Delft University of Technology

Master Thesis

Aerodynamics of dual facesheet acoustic liners

Author: Tim Bruins Slot
Student Number: 5638453

Thesis Supervisors: Dr D. Modesti (TU Delft)
H. Shahzad (TU Delft)

May 15, 2024

Abstract

This thesis presents an in-depth investigation of the consequences of adding a second facesheet on the aerodynamic performance of acoustic liners. This is done by performing pore-resolved Direct Numerical Simulations (DNS) of a channel flow at $Re_\tau = 500$. Simulations are conducted for various dual facesheet configurations, exploring different facesheet layouts and relative positions of the second facesheet. Design considerations are constrained by preserving the attenuation properties of the multiple facesheet liner, achieved by maintaining adequate spacing between the facsheet. The study examines how the presence and staggering of the second facesheet affect the pressure drop and the wall-normal velocity fluctuations, both of which correlate with the added liner drag. The simulations reveal a relationship between the staggering distance of dual facesheet liners and added drag, demonstrating that increased shifting distance of regular facesheet configurations leads to reduced added drag compared to lesser shifting distances. Furthermore, the staggering diminishes wall-normal velocity fluctuations between the facesheets, aligning with observed trends in added drag. However, the study finds that while dual facesheet configurations offer some reduction in added drag compared to conventional single facesheet designs, the extent of drag reduction is limited. The study shows that the addition of a second facesheet to the liner causes additional wall parallel permeabilities not present in a single facesheet liner influencing the flow below the wall.

Contents

List of Figures ii

List of Tables vii

List of Symbols and Abbreviations ix

1 Introduction 1

2 Acoustic liners 3
- 2.1 Sound attenuation and resonance . . . 4
- 2.2 Various liner configurations . . . 7

3 Smooth wall turbulence 10
- 3.1 Turbulent flow . . . 10
- 3.2 Turbulent channel flow . . . 12

4 Rough wall turbulence 16
- 4.1 Law of the wall and added drag . . . 19

5 Aerodynamic performance of acoustic liners 23
- 5.1 Parameter identification . . . 24
- 5.2 Instantaneaous flow . . . 26

6 Problem statement 30

7 Methodology 31
- 7.1 STREAmS . . . 31
  - 7.1.1 STREAmS validation . . . 32
- 7.2 Immersed Booundary Method . . . 34
  - 7.2.1 IBM validation . . . 35
- 7.3 Double facesheet . . . 36
  - 7.3.1 Geometry . . . 37
  - 7.3.2 Forchheimer coefficient . . . 40

8 Results and discussion 43
- 8.1 Instantaneuous flow in channel . . . 43
- 8.2 Mean Velocity profile . . . 45
  - 8.2.1 Relevant parameters for ΔU^+ . . . 49
- 8.3 Reynolds stresses . . . 51
  - 8.3.1 Relevant parameters for Reynolds stresses . . . 64

9 Conclusion and Recommendations 66

References 69

List of Figures

2.1 (a): Schematic image of the set-up of a conventional honeycomb structured acoustic liner. The top configuration shows the liner when stacked and the bottom three images show a sketch of the liner components displayed independently. Image taken from Herbert and Copiello (2015) (b): Schematic image of a jet engine taken from Kempton (2011). The pink highlighted section, at the intake and near the bypass duct, represents the acoustic liners present in a jet engine. 3

2.2 A schematic overview of a Helmholtz resonator cavity found in acoustic liners. The neck of the resonator is resembled by the hole in the facesheet and the main volume is that of the cavity below. Here l_{eff} is the effective length of the resonator neck, S represents the cross-sectional area of the neck and the volume V is the cavity volume. These variables are found in (2.4) for the calculation of the resonance frequency 5

2.3 Example of the resistance, reactance and attenuation of an acoustic liner. The left top plot indicates the resistance, the left bottom plot the reactance and the right plot the respective attenuation. The different line colours indicate different geometries, not of interest for the illustration. (Figure taken from Dodge et al. (2023)) 6

2.4 (a) Shows the variable depth liner from Schiller et al. (2019), here the cavities are connected to multiple orifices where the cavities have different depths. (b) Graphical representation of the liner configuration discussed by Howerton et al. (2012). Here each orifice has its own cavity of variable depth connected to it. (c,d) Show how the liner is constructed in the work of Cherrier et al. (2012). As can be seen in (c), the facesheets are directly positioned on top of each other and are staggered as displayed in (d), where the overlap of the plates can be seen. (e) Shows the triple facesheet configuration as discussed by Dodge et al. (2023). Here there is a space between the liner sheets (contrary to (c)) and are tested at fixed open area percentages as indicated in the image. Here the 50% case indicates that 50% of the single orifice area is open. 8

2.5 Impedance of the tipple facesheet configuration of Dodge et al. (2023) 9

3.1 Visual representation of the Reynolds decomposition. The Left image shows the total and the mean flow. The right image shows the decomposed elements. (from Reggente (2014)) 11

3.2 Schematic representation of a channel flow domain with the dimensions $L_x \times L_y \times L_z$ where the channel half width is indicated by δ. 12

3.3 Image of the contributions of to the total shear stress form Pope (2000) In the left image it can be seen how the viscous stresses contribute to the total shear stress plotted as a function of wall distance, the same is seen in the right image for the Reynolds stresses. In the figure, the dashed line represents a Reynolds number of $Re = 5600$ and the solid line represents $Re = 13750$. 13

3.4 Comparison of the normalised Reynolds stresses from DNS simulations for a $Re_\tau = 180$ channel flow (Red lines) compared to Lee and Moser (2015) DNS results (Black dashed lines). The Reynolds stresses in descending order are $\langle u_1' u_1' \rangle$,$\langle u_2' u_2' \rangle$, $\langle u_3' u_3' \rangle$ and $\langle u_1' u_2' \rangle$. . 14

3.5 The log law and u^+ for the viscous sub-layer plotted along near wall results of a DNS simulation performed by the author based on Lee and Moser (2015) for $Re_\tau = 180$. The velocity profile is the velocity profile found in the half of the channel flow and is scaled by viscous units. 15

4.1 Image taken from Chung et al. (2021) showing a typical, arbitrary, rough wall topography with its respective flow features. 16

4.2 Schematic figure of the equivalent sand grain roughness. (from Hetsroni et al. (2011)) . . 19
4.3 The roughness function plotted for a smooth wall and various types of roughness. (from Flack et al. (2007)) 21

5.1 (a) Figure representing the Reynolds dependence of the Darcy Forchheimer law for increasing Reynolds number (figure taken from Shahzad et al. (2022)). (b) ΔU^+ with respect to the inverse of the Forchheimer coefficient. (figure taken from Shahzad et al. (2023)) 26
5.2 Snapshot of the wall-normal velocity fluctuations over a porous surface of POA=32% at $Re_\tau = 2000$. Where the grey lines indicate the facesheet and cavity walls. (from Shahzad et al. (2023)) 27
5.3 (a-c): Velocity field of misaligned perforated plates at various distanced L/D of 1/8, 1/2 and 2 respectively. (d) Pressure loss coefficient EU as a function of L/D for misaligned perforated plates (yellow). (e) Geometry of the separate perforated plates and the combination of the two plates in the misalligned configuration. The white space shows the opening in the plate. (All images taken from La Rosa et al. (2021).) 28

7.1 (a,b) Comparison of mean velocity profile $\langle u^+ \rangle$ (w.r.t wall distance) from STREAmS (red line) and Lee and Moser (2015) (black squares) results. (c,d) Comparison of the Reynolds stresses $\langle u_i' u_j' \rangle^+$ from STREAmS (red line) and Lee and Moser (2015) (black squares)results. 33
7.2 Example of the Immersed Boundary Method (IBM). Here the white cells, with the open node points, represent the fluid nodes, the blue cells with black nodes the forcing points and the yellow with grey nodes are the solid cells and nodes respectively. The red line represents an arbitrary geometry onto which the IBM adapts itself. (from Liu and Hu (2019)) 34
7.3 Sketch of the geometry from MacDonald et al. (2018) used for the validation of the IBM. The image has the flow direction indicated, the width W and the height k of the roughness elements are shown. The height of the half channel is indicated with h where the dashed line indicates the position of the symmetry boundary. 35
7.4 (a): Comparison of the mean velocity profiles found by the IBM tested in STREAmS (red line) and the limited span half channel runs performed by MacDonald et al. (2018) (black squares) 36
7.5 (a): Orientation of the holes through both facesheets covering one cavity for the 50% open ($D_{50} - L14$) configuration. The light grey facesheet represents facesheet 1 (fs_1) and the darker grey facesheet represents facesheet 2 (fs_2). Combined they show the top view for the configuration where the white space indicates the passage through both plates. (b): Schematic cut-through of the domain in the x-plane showing both facesheets and the cavity below. The slice is through the middle of the orifices of the 50% open configuration. In the image, both fs_1 and fs_2 are indicated and the size of the cavity is indicated. (c): Zoomed in schematic image of (b) where the gap, the diameter and the staggering distance are pointed out having size $g = 0.342d$, $d = 0.08\delta$ and $d_{stag} = 0.0323\delta$ respectively. The staggering distance changes depending on the percentage open area of the configuration. 38

7.6 (a): Schematic image of the double facesheet liner, channel geometry in the $D_{100} - L14$ configuration. The geometry shows the square cavities with their corresponding 4 orifices per cavity. The domain has $L_x \times L_y \times L_z = 3\delta \times 2\delta \times 1.5\delta$ as its dimensions, with the thickness of both facesheets is $t_{fs1} = t_{fs2} = 0.435d$ and the spacing gap between the plates is $g = 0.342d$ as indicated in Table 7.2. (b): 100% open facesheet orientation ($D_{100} - L14$) of the top with respect to the bottom facesheet (i.e. fs_1 and fs_2 resp.) and the inner cavity walls (Black square). NOTE: both the liner reference cases (i.e. $L-L14$ and L_t-L14) have the same orifice and cavity orientation but with a single facesheet of $t = d$ and $t = 1/2d$ respectively. (c): 75% open facesheet orientation ($D_{75} - L14$) where the red holes indicate the orientation of the top facesheet (the sheet in direct contact with the flow) and the blue holes that of the bottom facesheet (the sheet which is connected to the cavities). (d): 50% open facesheet orientation ($D_{50} - L14$) with the bottom plate shifted upstream. (e): 50% open facesheet orientation ($D_{50} - L14_{inv}$) with the bottom plate shifted downstream. (f): Hole orientation of the staggered configuration $L - L14_{stag}$ with a single facesheet where $t = d$. (g): Double staggered facesheet hole orientation ($D_{1.6} - L14_{stag}$), with the same fs_1 configuration as $L - L14_{stag}$ while the bottom facesheet is staggered in the mirrored direction w.r.t the red holes from (f) and are shifted upstream like fs_2 of (d) resulting in a 1.16% open configuration. 39

7.7 (a): Shows a sketch of the computational domain of the pressure drop simulations here the inlet velocity is indicated by U_t, the size of the orifice and the thickness of the plate by d and t respectively and the pressure at the inlet and outlet is indicated by P_1 and P_2. For the purpose of the illustration the side walls have been removed such the individual facesheet are visible In the simulation these are closed. (b): shows the results of the simulations, performed for $D_{50} - L14$ indicated by ($\triangle$), $D_{75} - L14$ indicated by ($\square$) and $D_{100} - L14$ indicated by ($\times$) and $D_{1.6} - L14_{stag}$ indicated by ($*$) 41

8.1 Comparision of the instantaneous streamwise velocity fluctuations u_1' of a reference case for (a): the $S - H$ run and (b) : the $L - H32$ run for the $Re_\tau = 2000$ cases of Shahzad et al. (2023) take at $y^+ + l_T^+ = 12$. Additionally, from the current work (c): $L - L14$, (d): $D_{100} - L14$, (e): $L - L14_{stag}$ and (f): $D_{1.6} - L14_{stag}$. All flowfields of the current work are x-z planes of the full domain taken at $y^+ = 5$. The location of the orifices is indicated for the first 3 rows at the left side of each case. 44

8.2 Comparision of the instantaneous wall-normal velocity fluctuations u_2' of (a): $L - L14$, (b): $D_{100} - L14$, (c): $L - L14_{stag}$ and (d): $D_{1.6} - L14_{stag}$. All flowfields are x-z planes of the full domain taken at $y^+ = 5$. The location of the orifices is indicated for the first 3 rows at the left side of each case. 45

8.3 Schematic drawing of the near-wall turbulence over a porous and smooth surface, respectively. The virtual origin shift is indicated by l_T. 45

8.4 Averaged Reynolds shear stress $\langle \tau_{12} \rangle$ profiles vs. the viscous scaled wall distance y^+ without (a) and with (b) the virtual origin correction applied (l_T). The black dashed line indicates the $\langle \tau_{12} \rangle$ profile of the smooth-wall case ($S - L$: performed by Shahzad et al. (2023)). The liner cases are indicated by lines and corresponding coloured symbols as: $L - L14$ ($\blacksquare$), $L_t - L14$ ($\bullet$), $L - L14_{stag}$ ($\diamondsuit$), $D_{50} - L14$ ($\triangle$), $D_{75} - L14$ ($\square$), $D_{100} - L14$ ($\times$), $D_{50} - L14_{inv}$ ($\triangledown$), $D_{1.6} - L14_{stag}$ ($*$). 46

8.5 Comparison of the mean velocity profile $\langle \tilde{u_1}^+ \rangle$ versus the viscous scaled wall normal distance y^+. All figures show the three reference cases in black: the smooth wall $S - L$ reference case by the black dashed line (- -), $L - L14$ by ($\blacksquare$) and $L_t - L14$ by ($\bullet$). (a), compares these reference cases to the streamwise shifted dual facesheet liner cases $D_{50} - L14$ ($\triangle$), $D_{75} - L14$ ($\square$) and $D_{100} - L14$ ($\times$). (b) Shows the runs with a different fs_1 configuration like, $L - L14_{stag}$ ($\diamondsuit$) and $D_{1.6} - L14_{stag}$ ($*$) as well as the inverse shifted dual facesheet liner case $D_{50} - L14_{inv}$ ($\triangledown$). (c) and (d) are the zoomed-in images of (a) and (b) respectively. 47

8.6 Comparison of the viscous scaled velocity deficit (ΔU^+) of the dual facesheet cases versus the percentage open ($\%_{open}$) in (a) and the staggering distance d^+_{stag} in (b). The black lines are merely a visual aid to see a relationship between the velocity deficit of the respective runs. The only double facesheet configuration with a staggered top facesheet ($D_{1.6} - L14_{stag}$) is connected by a dashed line as the stagger magnitude change is not the only difference compared to the regular dual facesheet liner cases. The symbols represent the cases as: $D_{50} - L14$ (△), $D_{75} - L14$ (□), $D_{100} - L14$ (×), $D_{50} - L14_{inv}$ (▽) and $D_{1.6} - L14_{stag}$ (∗). 48
8.7 Drag variation (in %) for the different double liner cases displayed versus (d^+_{stag}) in (a) and versus the effective porosity (σ_{eff}) in (b). The liner cases are indicated by the following symbols: $L - L14$ (■), $L_t - L14$ (•), $L - L14_{stag}$ (◇), $D_{50} - L14$ (△), $D_{75} - L14$ (□), $D_{100} - L14$ (×), $D_{50} - L14_{inv}$ (▽), $D_{1.6} - L14_{stag}$ (∗). 48
8.8 ΔU^+ as a function of the Forchheimer coefficient $1/\alpha^+_y$ (a) and the Darcy permeability $\sqrt{K_y}^+$ (b). The reference cases from Shahzad et al. (2023) for the thick (plate thickness $t = d$) and thin (plate thickness $t = d/2$) facesheet are indicated by (– – ■) and (– - •) respectively. The liner cases of this work are indicated by the following symbols: $L - L14_{stag}$ (◇), $D_{50} - L14$ (△), $D_{75} - L14$ (□), $D_{100} - L14$ (×), $D_{50} - L14_{inv}$ (▽), $D_{1.6} - L14_{stag}$ (∗). 49
8.9 Schematic drawing of how r_{eff} is computed. This example shows the case for $D_{50} - L14$. 51
8.10 Viscous scale velocity deficit (ΔU^+) compared to the effective orifice radius in viscous units (r^+_{eff}) displayed in (a) and the effective porosity of the orifice $\sigma)eff$ in (b). Coloured symbols indicate the different liner cases as: $L - L14$ (■), $L_t - L14$ (•), $L - L14_{stag}$ (◇), $D_{50} - L14$ (△), $D_{75} - L14$ (□), $D_{100} - L14$ (×), $D_{50} - L14_{inv}$ (▽), $D_{1.6} - L14_{stag}$ (∗). . 51
8.11 Comparison of the intrinsic averaged Reynolds stress profiles. The primary, non-zero directions of the Reynolds stresses are given, i.e. (a): $\langle\tau_{11}\rangle/\tau_w$, (b): $\langle\tau_{22}\rangle/\tau_w$,(c): $\langle\tau_{33}\rangle/\tau_w$ and (d): $\langle\tau_{12}\rangle/\tau_w$ for the cases: S-L (- -), $L - L14$ (■), $L_t - L14$ (•), $D_{100} - L14$ (×), $D_{50} - L14_{inv}$ (▽), $D_{1.6} - L14_{stag}$ (∗). Some of the liner cases' results have been omitted for the clarity of the illustration. The double-liner cases (red) shown are selected as these represent the largest difference between the four cases. $D_{75} - L14$ and $D_{100} - L14$ values lay in between the two shown results. 52
8.12 Normalised instantaneous wall-normal velocity fluctuations u'_2/u_τ zoomed in at a cavity. The cases displayed are (a): the thick-wall reference case $L - L14$, (b): the thin-wall reference case $L_t - L14$, (c): the 50% open dual face-sheet liner case $D_{50} - L14$, (d): the 75% open dual face-sheet liner case $D_{75} - L14$, (e): the 100% open dual face-sheet liner case $D_{100} - L14$, (f): the 50% open, inversed, dual face-sheet liner case $D_{50} - L14_{inv}$, (g and h): the double staggered liner with 1.6% open configuration $D_{1.6} - L14_{stag}$. Here (g) shows the plane through the orifices which are closest to each other and (h) the orifices with the largest distance between them. 53
8.13 Normalised instantaneous spanwise velocity fluctuations u'_3/u_τ zoomed in at a cavity. The cases displayed are (a): the thick-wall reference case $L - L14$, (b): the thin-wall reference case $L_t - L14$, (c): the 50% open dual face-sheet liner case $D_{50} - L14$, (d): the 75% open dual face-sheet liner case $D_{75} - L14$, (e): the 100% open dual face-sheet liner case $D_{100} - L14$, (f): the 50% open, inversed, dual face-sheet liner case $D_{50} - L14_{inv}$, (g and h): the double staggered liner with 1.6% open configuration $D_{1.6} - L14_{stag}$. Here (g) shows the plane through the orifices which are closest to each other and (h) the orifices with the largest distance between them. 55
8.14 Wall normal component of the Reynolds stress, $\langle\tau_{22}\rangle$, Comparison for all runs. (a) and its zoomed-in version,(c), show the thick plate reference case: $L - L14$ (■) and the four straight shifted cases: $D_{50} - L14$ (△), $D_{75} - L14$ (□), $D_{100} - L14$ (×), $D_{50} - L14_{inv}$ (▽). (b) and its zoomed-in version, (d), show both the thick and the thin plate reference cases: $L - L14$ (■) and $L_t - L14$ (•) as well as both the staggered top facesheet cases: $L - L14_{stag}$ (◇) and $D_{1.6} - L14_{stag}$ (∗). The dashed, horizontal, lines at y+=0, -17 and -31 indicate the beginning of fs_1, the end of fs_1 and the beginning of fs_2 respectively. . . 56

8.15 Reynolds stress components on the y- normal plane ($\langle\tau_{11}\rangle$ and $\langle\tau_{33}\rangle$) comparison for all runs. (a) and (c) show $\langle\tau_{11}\rangle$ and $\langle\tau_{33}\rangle$ respectively for: $L-L14$ (■) and the four straight shifted cases: $D_{50}-L14$ (△), $D_{75}-L14$ (□), $D_{100}-L14$ (×), $D_{50}-L14_{inv}$ (▽). (b) and its zoomed-in version, (d), show b$\langle\tau_{11}\rangle$ and $\langle\tau_{33}\rangle$ respectively for: $L-L14$ (■) and L_t-L14 (•) as well as both the staggered top facesheet cases: $L-L14_{stag}$ (◇) and $D_{1.6}-L14_{stag}$ (∗). The dashed, horizontal, lines at y+= -17 and -31 indicate the end of fs_1 and the beginning of fs_2 respectively displaying the facesheet gap. 57
8.16 Comparison of the maximum value of the wall parallel Reynolds stresses ((a): $\max(\langle\tau_{11}\rangle_{-31<y^+-17})$ and (b): $\max(\langle\tau_{33}\rangle_{-31<y^+-17})$) between the facesheets plotted versus the viscous scaled shifting distance d^+_{stag}. The symbols represent the following cases: $D_{50}-L14$ (△), $D_{75}-L14$ (□), $D_{100}-L14$ (×), $D_{50}-L14_{inv}$ (▽) and $D_{1.6}-L14_{stag}$ (∗). 58
8.17 (a): Normalized instantaneous streamwise velocity (u_1/u_τ) and (b): Normalized spanwise velocity (u_3/u_τ) shown on an x-z plane in the middle of the facesheet gap, $y^+=-24$, of $D_{1.6}-L14_{stag}$. Both figures depict the vector field indicating the wall-parallel velocity of magnitude $\|(u_1,u_3)\|_2$ and direction $\langle u_1,u_3\rangle$. The figure overlays the geometry, where the red geometry represents the orifices in fs_1, the blue geometry represents the orifices in fs_2, and the black geometry indicates the cavity walls. These elements illustrate the location of the respective features, although they are not present at $y^+=-24$. 59
8.18 (a): Normalized instantaneous streamwise velocity (u_1/u_τ) and (b): Normalized spanwise velocity (u_3/u_τ) shown on an x-z plane in the middle of the facesheet gap, $y^+=-24$, of $D_{100}-L14$. Both figures depict the vector field indicating the wall-parallel velocity of magnitude $\|(u_1,u_3)\|_2$ and direction $\langle u_1,u_3\rangle$. The figure overlays the geometry on the flow fields. The orifices in fs_1 and fs_2 are shown by the blue orifices (as they overlap) and the black geometry indicates the cavity walls. These elements illustrate the location of the respective features, although they are not present at $y^+=-24$. 60
8.19 Normalized instantaneous streamwise velocity (u_1/u_τ) and (b): spanwise velocity (u_3/u_τ) shown on an x-z plane at $y^+=-24$ for the single facesheet $L-L14$ case. Both figures depict the vector field indicating the wall-parallel velocity of magnitude $\|(u_1,u_3)\|_2$ and direction $\langle u_1,u_3\rangle$. The black circles indicate the orifices in the thick facesheet and the black squares show the location of the cavity walls below the facesheet (i.e. $y^+<-40$). . 61
8.20 Normalised streamwise velocity in an x-y plane through the orifice and cavity. The figures show vectors of magnitude $\|(u_1,u_2)\|_2$ and direction $\langle u_1,u_2\rangle$. The display is of the bottom wall of the domain, where the wall is at $y/\delta=-1$. The cases presented are (a): $L-L14$, (b): L_t-L14, (c): $D_{100}-L14$, (d): $D_{75}-L14$, (e): $D_{50}-L14$, (f): $D_{50}-L14_{inv}$ and (g): $D_{1.6}-L14_{stag}$. The liner walls are indicated in grey. 62
8.21 Percenntual decrease of the Wall normal Reynolds stresses over the facesheet gap ($\%\Delta\langle\tau_{22}\rangle_{gap}/\tau_w$) compared to the staggering distance (d^+_{stag}) displayed in (a) and the value of $\langle\tau_{22}\rangle$ found at y+=-40, i.e. the bottom of the L-L14 facesheet, in (b). The different liner cases are indicated by coloured symbols as: $L-L14$ (■), L_t-L14 (•), $L-L14_{stag}$ (◇), $D_{50}-L14$ (△), $D_{75}-L14$ (□), $D_{100}-L14$ (×), $D_{50}-L14_{inv}$ (▽), $D_{1.6}-L14_{stag}$ (∗). Note that for (b) the single facesheet liner cases are included as lines to provide a comparison, they do not have a staggering distance as they only have a single facesheet in the geometry. . . 64
8.22 (a): ΔU^+ vs Percenntual decrease of the Wall normal Reynolds stresses over the facesheet gap ($\%\Delta\langle\tau_{22}\rangle_{gap}/\tau_w$) (b): ΔU^+ vs $\max(\langle\tau_{22}\rangle)$ for $y^+<0$. The different liner cases are indicated by coloured symbols as: $L-L14$ (■), L_t-L14 (•), $L-L14_{stag}$ (◇), $D_{50}-L14$ (△), $D_{75}-L14$ (□), $D_{100}-L14$ (×), $D_{50}-L14_{inv}$ (▽), $D_{1.6}-L14_{stag}$ (∗). 65

List of Tables

5.1 Results of previous studies on the drag of acoustic liners. All of the results resemble grazing flow over different acoustic liners. The relative size of the orifice diameter d, the cavity depth h and the facesheet thickness t w.r.t. the boundary layer thickness have been indicated. σ resembles the porosity factor, Ma is the Mach number and Re_τ is the friction Reynolds number. Eventually, in the last column, the drag increase (with respect to a smooth wall) in percentages are given which are found in all studies. Many of the values presented are not directly indicated in the studies. Some results have readily been extracted by Shahzad et al. (2023) while others have been deducted from figures or calculated from other known quantities of the respective studies. 24

7.1 Comparison of the reference case runs and the validation. LM indicates the reference case (Lee and Moser (2015)) and VS indicates the **V**alidation run of **S**TREAmS. The number behind this distinction is the indication of the friction Reynolds number Re_τ. Re_b is the bulk Reynolds number, L_x and L_z the domain size normalised by the half channel width δ. Δx^+ and Δz^+ is the size of the mesh elements in x and z direction respectively. Δy_w^+ is the mesh spacing at the wall and Δy_c^+ at the channel centre-line. N_y is the number of mesh elements in the y-direction and $Tu\tau/\delta$ is the simulation time taken to gather statistics (Eddy Turnover Time). 32

7.2 Geometry overview and comparison of the different cases of interest. The DNS geometry from Shahzad et al. (2023) for the perforated single facesheet where the first L refers to Liner configuration, the second to $Re_\tau = 500$, 14 the POA and the 't' subscript indicates the thin facesheet. The orifice diameter d is expressed as a function of half channel width $\delta = 1$ (in the first case). The facesheet porosity σ and the effective porosity σ_{eff} are shown for all cases. The effective porosity is the area of the holes which can be looked through when the facesheets are staggered. Additionally, the largest facesheet gap configuration 'G3', of the experimental set-up, of Dodge et al. (2023) is shown, for different opening percentages (i.e. 100% and 25%). The orifice diameter d is expressed in inches and the facesheet spacing gap g is expressed in the orifice diameter. The same is done for the CFD set-up from La Rosa et al. (2021) for both the staggered and non-staggered cases. The spacing g however for this case indicates the spacing at which the pressure drop over the two plates is maximum and the orifice diameter is expressed in millimetres. 37

7.3 DNS dataset of all runs of which results are used in the results section. The first 3 runs (S_L, $L-L14$ and L_t-L14) are performed by Shahzad et al. (2023) 40

7.4 Values found for the slope and the wall intercept of the normalised pressure drop and converted to the viscous scaled Forchheimer and Darcy coefficient. The values of the first 3 cases are from Shahzad et al. (2023) and the remaining 5 originate from current simulations. Both the Forchheimer coefficient and the Darcy permeability are converted such that their unit is a length scale $[L]$. (The unit of α_y is $[L^{-1}]$ and of K_y is $[L^2]$) . . . 42

List of Symbols and Abbreviations

χ : Reactance

ΔD : Drag variation (%)

ΔP : Pressure drop

ΔU^+ : Viscous scaled velocity deficit

Δx^+ : Mesh spacing in x-direction

Δy_c^+ : Viscous scaled centreline spacing

Δy_w^+ : Viscous scaled wall spacing

Δz^+ : Mesh spacing in z-direction

δ_ν : Viscous lengthscale

δ_{ij} : Kronecker delta

δ : Half channel width

ϵ_o : Opening ratio

κ : Von Karman constant

λ : Wavelength

$\langle \tau_{ij} \rangle$: Reynolds stresses in the i,j th direction

$\langle u \rangle$: Mean Velocity

μ : Dynamic viscosity

ν : Kinematic viscosity

ω_r : Resonant frequency

ω : Angular frequency

ρ : Density

σ_{eff} : Effective porosity

σ_{ij} : Viscous stress tensor

σ : Porosity

τ_w : Wall shear stress

τ : Total shear stress

α_{ij} : Forchheimer permeability tensor

α_y^+ : Viscous scaled wall normal Forchheimer coefficient

B_s : Equivalent sand grain roughness log law wall intercept

C_{fr} : Rough wall friction coefficient

C_{fs} : Smooth wall friction coefficient

c_0 : Sound velocity

C_f : Friction coefficient

c_v : Heat capacity at constant volume

c : Speed of sound

CO_2 : Carbon dioxide

d^+_{stag} : Viscous scaled staggering distance

d^+ : Viscous scaled hole diameter

d : Orifice diameter

d_0 : Wall offset

dB : Decibel

E : Energy

f : Frequency

f : Forcing term

fs_1 : Top facesheet

fs_2 : Bottom facesheet

g^+ : Viscous scaled gap spacing

H : Enthaply

h : Orifice depth

K_{ij} : Darcy permeability tensor

K^+_{ij} : Viscous scaled Darcy permeability tensor

k^+_s : Viscous scaled sand grain roughness height

k_s : Sandgrain roughness height

k^+ : Viscous scaled roughness height

k : Turbulent kinetic energy

k : Roughness height

l_eff : Effective neck length Helmholtz resonator

l_T : Virtual origin shift

L_x : Domain length in x-direction

L_y : Domain length in y-direction

L_z : Domain length in z-direction

L : Quarter wave cavity length

M : Mass

N_x : Number of mesh elements in the streamwise direction

N_y : Number of mesh elements in the wall-normal direction

N_z : Number of mesh elements in the spanwise direction

n : Integer

p_0 : Reference pressure

p_x : Pressure in x direction

p : Pressure

P : Turbulence production

Pa : Pascal

q_j : Heat flux

r_n : Neck Radius Helmholtz resonator

r_u : Tube Radius Helmholtz resonator

r^+_{eff} : effectve radius

R : Resistance

r : Radius

Re_δ : Reynolds number Based on channel halfwidth

Re_τ : Friction Reynolds number

Re_0 : Reynolds number Based on the centreline velocity

Re_p : Pore Reynolds number

Re : Bulk Reynolds number

S : Neck area Helmholtz resonator

t^{fs1} : Thickness of the top facesheet

t^{fs2} : Thickness of the bottom facesheet

t^+ : Viscous scaled facesheet thickness

t : facesheet thickness

t : Time

T : Temperature

u_τ : Friction velocity

u_0 : Centreline velocity

u_b : Bulk Velocity

u_i : flow direction

U^+_r : Viscous scaled rough wall velocity

U^+_s : Viscous scaled smooth wall velocity

U_t : Superficial velocity

u'_1 : Streamwise velocity fluctuation

u^+ : Viscous scaled Velocity

u : Velocity

V_c : Cavity volume Helmholtz resonator

u'_2 : Wall normal velocity fluctuation

u'_3 : Spanwise velocity fluctuation

x_i : direction

y_r : Roughness sublayer

y^+ : Viscous scaled wall distance

Z : Impedance

B : Smooth wall log law wall intercept

BPF : Blade passing frequency

GPU : Graphical Processing unit

DDOF : Double degree of freedom

DNS : Direct numerical simulation

EU : Pressure Loss coefficient

FAA : Federal Aviation Agency

HPC : High-Performance Computing

IATA : International Air Transport Association

IBM : Immersed boundary method

ICAO : International Civil Aviation Organisation

LES : Large eddy simulations

Ma : Mach number

MPI : Message Passing Interface

NS : Navier–Stokes

POA : Percentage open area

Re : Reynolds number

RMS : Root Mean Square

SAF : Sustainable Aircraft Fuel

SDOF : Single degree of freedom

SPL : Sound pressure level

STREAmS : Supersonic TuRbulEnt Accelerated navier -stokes Solver

TKE : Turbulent kinetic energy

USA : United States of America

1 Introduction

During take-off and landing, aircraft generate significant noise levels, prompting regulatory bodies such as the International Civil Aviation Organization (ICAO) and the Federal Aviation Administration (FAA) to establish increasingly stringent noise regulations. These regulations drive continuous innovation in noise reduction strategies for aircraft.

A significant source of noise during aircraft operation, particularly during take-off and landing, is the engine. Many commercial flights use high bypass ratio jet engines that emit a range of frequencies. To mitigate noise emissions, efforts have been focused on attenuating these frequencies within the engine itself. Acoustic liners, comprising perforated facesheets with cavities below to absorb sound energy, have been extensively researched for this purpose (XuQiang and ZhengTao (2020)).

While significant progress has been made in reducing engine noise through various acoustic mechanisms, the implementation of acoustic liners in engine nacelles has led to an unintended consequence: increased aerodynamic drag compared to smooth-wall configurations (Howerton and Jones (2015)). This is due to the flow perceiving the perforated facesheet as a rough surface, resulting in a substantial drag penalty. Conventional acoustic liner geometries can produce up to 70% more drag per plane area than equivalent smooth surfaces (Shahzad et al. (2023)). Since acoustic liners cover only a small area of the aircraft, the overall increase in drag for the entire aircraft due to the acoustic liners is modest. However, the overall impact on all aircraft combined can certainly not be neglected.

The progress on the acoustics properties of the acoustic liners is due to the acoustics being well understood. Many authors have provided empirical relations to compute the acoustic performance of a liner geometry. The same can not be said about the aerodynamics of perforated surfaces. In this area, only limited research has been performed and there is no (empirical) relation capable of determining the aerodynamic performance of the liner without extensive experimental or numerical simulations. Recent studies however have delved into the aerodynamics of perforated surfaces used in acoustic liners, like Shahzad et al. (2023).

While the current drag penalty limits the widespread application of acoustic liners, there is potential for future advancements to enable their use in new areas beyond engine nacelles. If the drag penalty could be reduced or eliminated, acoustic liners could be applied to larger areas of the aircraft, such as the fuselage (XuQiang and ZhengTao (2020)). This expanded application could facilitate the adoption of more efficient aircraft configurations, such as open fan or distributed propulsion systems, while still meeting noise regulations near airports (Thomas et al. (2014)).

Thesis outline

This thesis will therefore be focused on the aerodynamic properties of acoustic liners. The aim is to test these through pore-resolved DNS simulations as has been done by Shahzad et al. (2022). However, before the rationale behind the geometry will be explained some background knowledge is provided to improve the readers' understanding and context of the specific topic at hand.

Chapter 2 elaborates on the acoustics of acoustic liners, beginning with an exploration of their working principle and a review of state-of-the-art liner design. This sets the stage for understanding the acoustic constraints that shape liner development. From Chapter 3 onwards, the focus shifts to the aerodynamics of liners. Chapter 3 starts with a primer on general turbulence, followed by an examination of turbulent

channel flow over smooth walls. Building upon this foundation, Chapter 4 extends the discussion to turbulent flow over rough walls, exploring various parameters for identifying roughness and introducing a drag quantification tool. Chapter 5 narrows the focus to the specific roughness type relevant to acoustic liners: porous surfaces. This chapter reviews studies on added drag reduction and identifies key contributors to acoustic liner drag. Chapter 6 synthesizes the findings from previous chapters, presenting the problem statement and research questions of the thesis. In Chapter 7, the numerical method and boundary method are thoroughly explained, alongside a discussion of geometric choices and flow conditions for the simulated cases. This chapter also outlines the reference cases and methodologies for obtaining results. Chapter 8 is dedicated to presenting and discussing the results of the simulations conducted throughout the thesis. Finally, Chapter 9 offers conclusions drawn from the research and provides further recommendations for future studies.

2

Acoustic liners

The acoustic liners which are of interest in this discussion are those found in the inlet of a jet engine, positioned in front of the fan and inside the bypass duct. These are used to attenuate the tonal fan and broadband turbulent noise emitted by the engine. The placement of the liner can be seen in Figure 2.1 (b). The degree of the attenuation of sound depends on the set-up and type of acoustic liner. Generally, these acoustic liners are single or double degree of freedom (SDOF or DDOF resp.) liners (Ingard (1953)) consisting of a porous facesheet, a honeycomb structure and a solid back plate as can be seen in Figure 2.1 (a) Beck et al. (2015). The degree of freedom relates to the number of cavities stacked onto each other. These liners attenuate sound through Helmholtz resonance where the ratio of volumes of the compartments is of interest Fahy (2001).

The review on the acoustic properties of acoustic liners has two primary objectives. Firstly, it aims to understand the working principle of these liners. Secondly, it identifies acoustic performance parameters for the definition of constraints on the attenuation properties. An interesting aspect of the investigation is the examination of how the geometry of the facesheet affects sound attenuation properties. The definition of constraints for facesheet geometry is necessary to preserve the liner's primary function. This is crucial, as the loss of acoustic attenuation properties renders the holes redundant, adding unnecessary complexity and becoming a source of drag in the nacelle. Ultimately, the discussion will focus on the sound attenuation capabilities of various studied liner geometries.

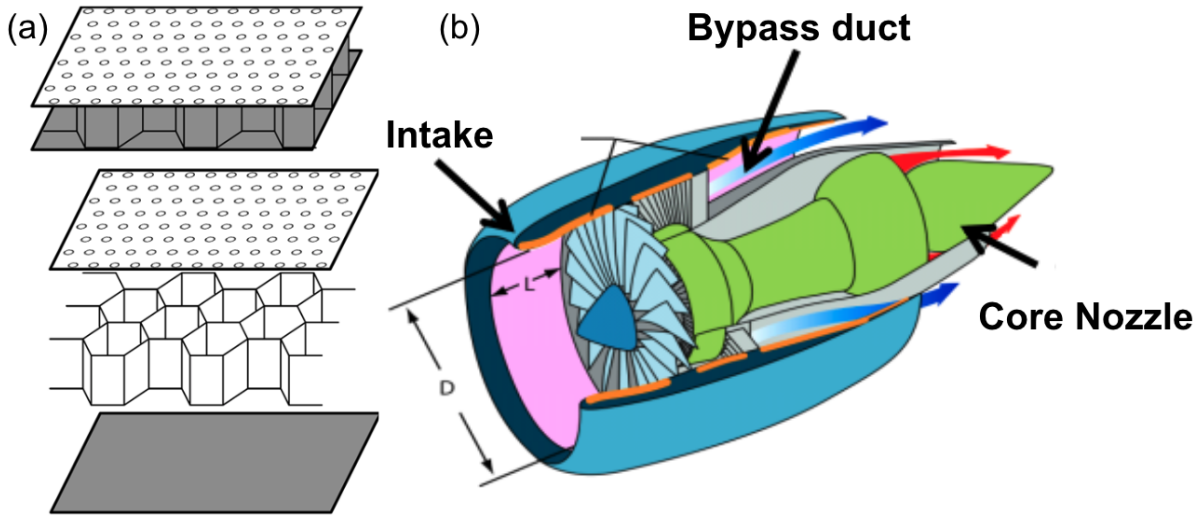

Figure 2.1: (a): Schematic image of the set-up of a conventional honeycomb structured acoustic liner. The top configuration shows the liner when stacked and the bottom three images show a sketch of the liner components displayed independently. Image taken from Herbert and Copiello (2015) (b): Schematic image of a jet engine taken from Kempton (2011). The pink highlighted section, at the intake and near the bypass duct, represents the acoustic liners present in a jet engine.

2.1 Sound attenuation and resonance

As mentioned above, the main mechanism for the attenuation of incident sound waves in cavities is done through Helmholtz resonance. To adequately discuss the mechanism it is appropriate to briefly define what 'sound' or 'noise' is and continue the discussion from that point to the principle of the attenuation mechanism.

From a physical perspective, sound can be defined as an acoustic wave propagating through a medium, which, in the present case, is air. ANSI (2014) describes sound as the following: *"Oscillation in pressure, stress, particle displacement, particle velocity, etc., propagated in a medium with internal forces (e.g., elastic or viscous), or the superposition of such propagated oscillation."* This definition is how sound will be perceived in this review. The sound in a jet engine originates from the blade passing of the turbine blade and the turbulent flow due to the high bypass ratio inside the jet. Both these phenomena cause pressure undulations in the surrounding air resulting in noise. The main difference between the two noise sources is that the blade passing of the turbine happens at a specific frequency whilst the turbulent flow causes a more broadband noise, that is a combination of many frequencies. The use of acoustic liners generally is aimed at the attenuation of specific frequencies and is tuned to that of the turbine. (XuQiang and ZhengTao (2020))

To reduce emitted sound from the jet engine, there is a need to absorb and attenuate the incident sound in the acoustic liners. This is done by tuning the resonant frequency of the acoustic attenuation cavity in the liner to match the dominant frequency of the engine noise. Achieving resonance in the cavity leads to numerous interactions of the sound in the cavity with the facesheet and cavity walls, resulting in a strong response to the respective frequency. The resonance induces various viscous losses, such as viscous scrubbing (Jones et al. (2020)). These effects contribute to the absorption and attenuation of sound energy, ultimately reducing noise (Dai and Aurégan (2018)).

According to Yang et al. (2010), the resonance in the cavity results in a negative dynamic stiffness, which measures a resonator's ability to resist deformation or respond to externally applied forces (Zhao et al. (2016)). A negative dynamic stiffness makes the resonator highly susceptible to incident sound. This phenomenon facilitates both absorption and dissipation of sound energy, effectively attenuating the incident sound waves.

The use of the Helmholtz resonator in acoustic liners is common practice. In a Helmholtz resonator, the objective is to attain resonance in the cavity which ensures the attenuation of sound energy through dissipation. The Helmholtz resonator is often explained by the analogy of blowing over the top of a (partially) empty bottle making it hum at a specific frequency. This is a form of a Helmholtz resonator. Fundamentally, the Helmholtz resonator consists of a neck and a cavity connected to it. The resonance in the cavity relies on the grazing flow over the opening in the neck and the geometric ratios of the neck and the cavity volume. An example of a Helmholtz Resonator is given in Figure 2.2, where a side view of a Helmholtz resonator is given as found in the application of an acoustic liner.

Acoustic impedence

The sound response of the Helmholtz resonator is found through the acoustic impedance of the resonator. The impedance is a measure of the ease with which sounds pass through a medium or are absorbed by it (Fahy (2001)). Generally, the impedance is a function of the resistance and the reactance of the resonator as shown in (2.1):

$$Z = R + j\chi \tag{2.1}$$

Here R indicates the resistance of the resonator, which translates to the energy transfer of an acoustic wave, where the pressure and motion have aligned phases, resulting in work being done on the medium. χ represents the reactance of the resonator which is the out-of-phase portion of the pressure and motion of the sound in the resonator. As a result, the reactance does not transfer energy. The reactance part is imaginary and the resistance is real. A Helmholtz resonator has a specific impedance function in a tube with grazing flow given by (2.2) (from Chen et al. (1998) and Mechel (2008)):

$$Z = \rho_0\left(\frac{\omega^2}{\pi c_0}\left(2 - \frac{r_n}{r_u}\right) + 0.425\frac{Mc_0}{S} + j\left(\frac{\omega l_{eff}}{S} - \frac{c^2}{V_c\omega}\right)\right) \tag{2.2}$$

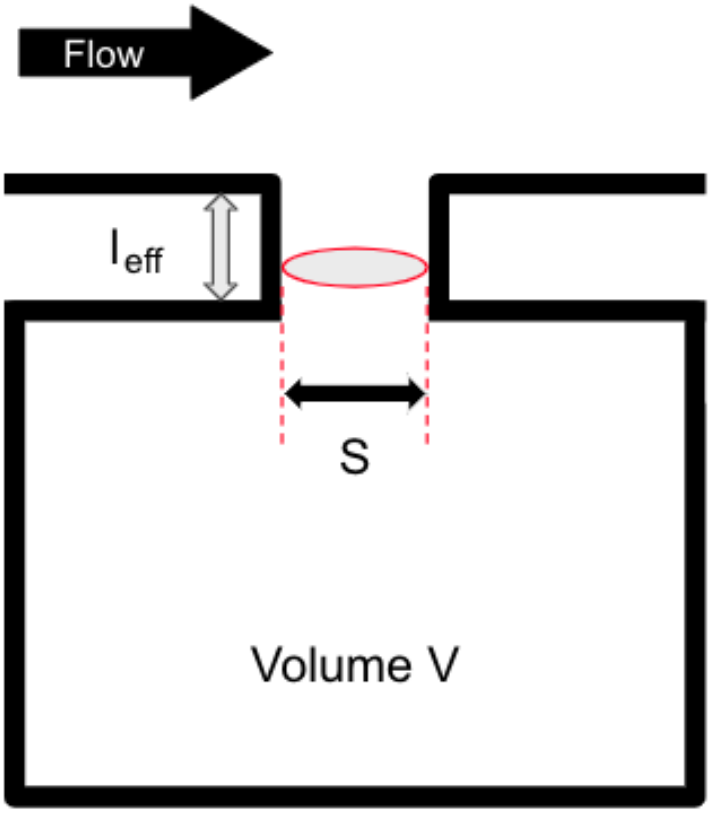

Figure 2.2: A schematic overview of a Helmholtz resonator cavity found in acoustic liners. The neck of the resonator is resembled by the hole in the facesheet and the main volume is that of the cavity below. Here l_{eff} is the effective length of the resonator neck, S represents the cross-sectional area of the neck and the volume V is the cavity volume. These variables are found in (2.4) for the calculation of the resonance frequency

Where r_n and r_u are the radius of the neck of the resonator and the tube respectively. Although this impedance equation does not exactly match the acoustic liner configuration as the radius of the tube does not resemble the channel width, the reactance of the impedance function does not depend on the tube.

More importantly, the reactance part (imaginary part) of (2.2) dictates the resonance frequency of the Helmholtz resonator. As the description of the reactance might suggest, when the Helmholtz resonator is in resonance, the out-of-phase pressure and motion of the sound are not present, meaning the reactance equals 0 as shown in (2.3):

$$\chi = \rho_0(\frac{\omega l_{eff}}{S} - \frac{c^2}{V_c \omega}) = 0 \tag{2.3}$$

This equation shows how the derivation of the resonance frequency (ω_r), as found in (2.4), is achieved:

$$\omega_r = c\sqrt{\frac{S}{l_{eff} V_c}} \tag{2.4}$$

Here c is the sound velocity, S is the area of the neck of the resonator, V_c is the cavity volume and l_{eff} is the effective length of the neck. According to XuQiang and ZhengTao (2020), the effective length is longer than the physical neck length due to account for the vibrating mass of fluid in the resonator neck. For a flanged-out neck, which most closely resembles the acoustic liner configuration, $l_{eff} = l + 1.7r$. This is in agreement with the definition Chen et al. (1998) gives for the effective length.

The resonator functions by attenuating incident acoustic waves through the dissipation of acoustic energy when in resonance. As depicted in (2.4), the Helmholtz resonator resonates at a specific frequency determined by the cavity's dimensions. Specifically, the resonance frequency is influenced by the ratio of several geometric parameters, including the neck cross-sectional area, the effective length of the neck, and the volume of the cavity. This geometric flexibility allows for precise tuning to target frequencies while adhering to the weight and size constraints of the engine nacelle.

This flexibility becomes particularly advantageous with the recent increase in turbine fan diameters. Larger fan sizes result in lower frequency noise due to a decreased blade-tip passing frequency, corresponding to longer wavelengths. Consequently, Helmholtz resonators can maintain their compact size while adjusting geometric ratios to resonate at lower frequencies. This adaptability positions them as the preferred method for acoustic attenuation in acoustic liners, as noted by XuQiang and ZhengTao (2020).

Sound attenuation

An example of the resistance, reactance and the resulting sound attenuation can be seen in Figure 2.3. This image depicts a liner over a cavity. As observed in the reactance figure, the resonant frequency is identified at the frequency where the reactance intersects 0. The effect of the resonance can be seen in the right plot, where there is a peak in attenuation at the resonant frequency. At other frequencies there is some attenuation however much less than at the resonant frequency, especially when realised that the Sound Pressure Level (SPL) is a logarithmic measure (2.5):

$$SPL = 20log_{10}(\frac{p}{p_0})[dB] \tag{2.5}$$

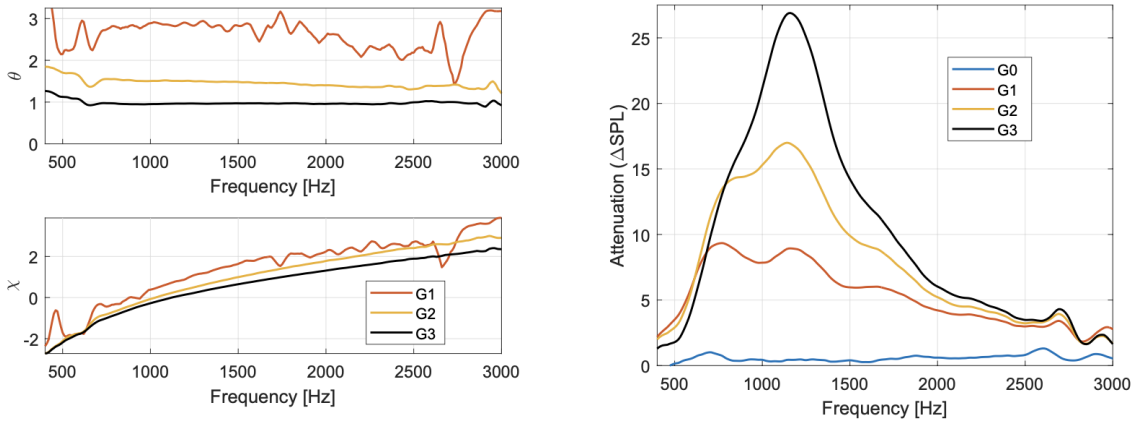

Figure 2.3: Example of the resistance, reactance and attenuation of an acoustic liner. The left top plot indicates the resistance, the left bottom plot the reactance and the right plot the respective attenuation. The different line colours indicate different geometries, not of interest for the illustration. (Figure taken from Dodge et al. (2023))

The acoustic performance of the liner can be determined experimentally or simulated numerically by an assessment of the impedance of the liner. As an added benefit, since the impedance is an intrinsic property of the liner the impedance values can be merely calculated and then be used as a boundary condition in numerical simulations of aircraft manufacturers to asses the true sound attenuation reached by the liner. The impedance of liners can be calculated well as has been done by many different authors (Casalino et al. (2018); Shur et al. (2020); Jones et al. (2022)).

Although the acoustic performance of conventional acoustic liners is well understood, the ongoing expansion of engine size, increases in bypass ratios, and increasingly stringent noise emission regulations necessitate continuous advancements in acoustic liner technology. Key objectives in acoustic liner research focus on maximizing noise attenuation per unit surface area, minimizing liner thickness to reduce overall weight, broadening attenuation capabilities across a wider frequency range (Jones et al. (2022)), and mitigating facesheet drag. Achieving these objectives involves exploring various configurations, which will be further detailed in the following section.

2.2 Various liner configurations

As the previous section has highlighted, impedance and attenuation are the most important metrics for the performance of an acoustic liner. The impedance of the acoustic liners is mainly a result of the liner geometry ratios when the conventional cavity design is maintained. The single cavity Helmholtz resonator design in a liner is often referred to as a local reacting liner (Jones et al. (2020) and XuQiang and ZhengTao (2020)). These liners consist of regular Helmholtz resonators in series, classically they are all the same volume and filled with air. Although these liners fulfil the basic needs of sound attenuation to a certain extent, there is a need to improve the attenuation mechanism of the liners.

To achieve greater efficiency in acoustic liners, one effective approach is to enhance sound attenuation at the targeted frequency. Numerous novel liner designs have been proposed, demonstrating superior sound attenuation properties compared to conventional single-degree-of-freedom (SDOF) Helmholtz resonator liners. Several examples will be highlighted, beginning with the metal foam liner. In addition to cavities filled with air, investigations have explored the use of metal foam liners Sutliff and Jones (2009), which have shown lower frequency absorption Bozak et al. (2019) and more efficient attenuation Sutliff et al. (2013). However, due to their high tunability, comparing performance between different metal liners can be challenging. An extension of the metal foam liner approach is the local reacting liner, introduced by Hillereau et al. (2005), where the cavity walls are perforated instead of impermeable. This design allows sound to pass from chamber to chamber, enhancing sound attenuation beyond local reactions.

In contrast to many conventional designs featuring a rigid honeycomb structure between the facesheet and the back plate, Bake and Knobloch (2019) presents a proof of concept for a liner with a flexible inner wall. This design demonstrates increased absorption and a better broadband response. Additionally, a proof of concept is provided for a zero mass flow liner, a form of bias flow liner, achieving similar results to the flexible wall (FlexiS) liner.

McAuliffe (1950) firstly came up with a bias flow mechanism in the orifice, which allowed acoustic energy to be transformed into kinetic energy near the orifices. According to Bechert et al. (1997), this causes additional vorticity shedding close to the orifices dissipating the transformed acoustic energy into heat through the kinetic energy of the vorticity. Many research efforts have been invested into the bias flow as underscored by XuQiang and ZhengTao (2020), who have shown promising results for sound attenuation efficiency. Bielak et al. (1999) takes a different approach, using active bias flow and temperature control to ensure additional sound attenuation. This is however deemed not sufficient in the scope of goals set for the noise reduction campaign.

For a more broadband liner response, there is a preference for liners with geometrical variations effective at multiple frequencies. Mesh cap liners, for instance, utilize mesh caps in honeycomb liners to create variable depth liners. Svetgoff and Manimala (2018) tunes the material of mesh cap liners for good low-frequency absorption, providing a lighter and less complicated alternative to double-degree-of-freedom (DDOF) liners. Variable depth acoustic liners, as discussed by Parrott and Jones (1995), feature chambers with different depths along the surface, ensuring more broadband noise attenuation due to varying impedance responses. Some liners integrate facesheets with varying depth cavities below, as illustrated in Figure 2.4 (a).

Another approach to variable depth liners involves connecting a cavity to each orifice, mitigating the facesheet, as explored by Howerton et al. (2012). These liners are highly tunable, allowing for changes in cavity order and geometry to tailor the acoustic response to specific requirements.

Checker-board liners, investigated by Watson et al. (2004), demonstrate promising sound attenuation improvements over conventional uniform liners. They are able to attenuate substantially more noise at the targeted frequency and display better performance regarding broadband frequencies, despite not being specifically designed for them.

While variable depth liners generally have cavities that cannot be adjusted according to flight status needs, there are adaptive liner designs with Helmholtz resonators featuring adaptive volume cavities to achieve resonance at various frequencies, as discussed by McDonald et al. (1997); Matsuhisa et al. (1992); de Bedout et al. (1997); Kostek and Franchek (2000). However, these designs come with added weight and complexity due to active elements tuning the liner to the flight status, which is less desirable.

Williams et al. (2002) takes a different approach again, using adaptive, tuned, while still passive vibration absorbers, through shape memory alloys. This allows the tuning of the resonant frequency by 15%. Liu

et al. (2003) also presents a tunable acoustic liner, here again, a vastly different approach is taken. The study focused on the use of an electromechanically tunable Helmholtz resonator using a compliant piezoelectric composite back-plate in the liner. This allows for a diaphragm-like back-plate which can be tuned such that the single-layer liner is a two-degree-of-freedom system tunable over 8% of frequency. Ichihashi (2013) presents a system which has an adaptive open area reacting to velocity changes in the flow yielding a more favourable non-linearity factor.

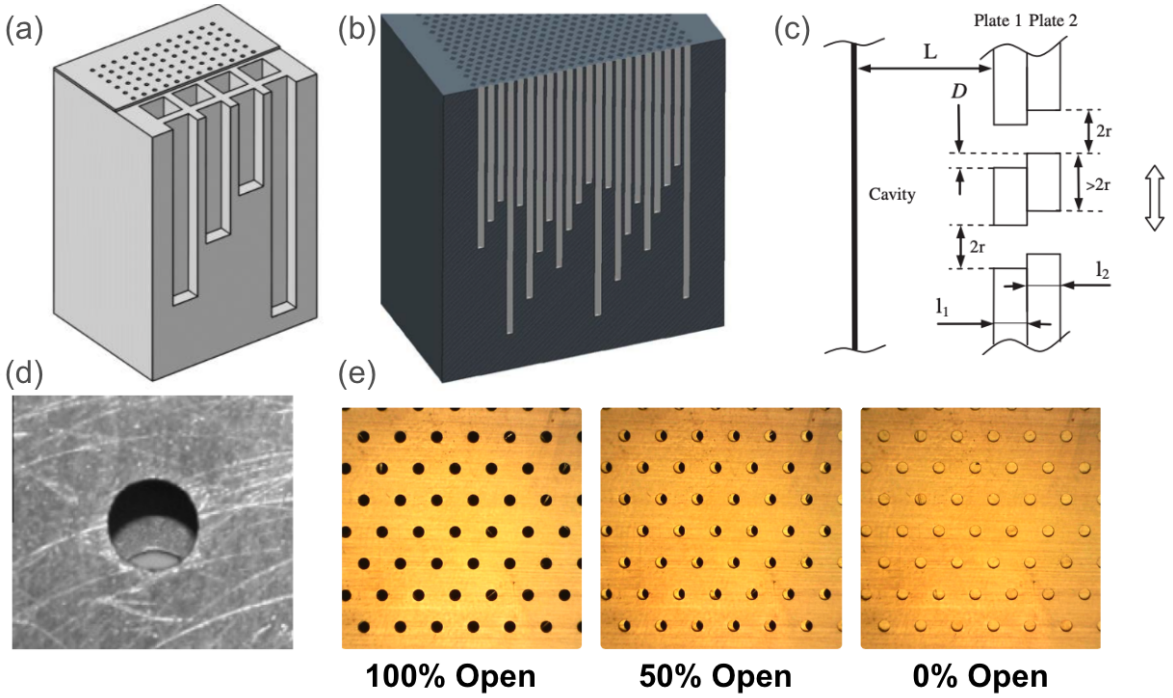

Figure 2.4: (a) Shows the variable depth liner from Schiller et al. (2019), here the cavities are connected to multiple orifices where the cavities have different depths. (b) Graphical representation of the liner configuration discussed by Howerton et al. (2012). Here each orifice has its own cavity of variable depth connected to it. (c,d) Show how the liner is constructed in the work of Cherrier et al. (2012). As can be seen in (c), the facesheets are directly positioned on top of each other and are staggered as displayed in (d), where the overlap of the plates can be seen. (e) Shows the triple facesheet configuration as discussed by Dodge et al. (2023). Here there is a space between the liner sheets (contrary to (c)) and are tested at fixed open area percentages as indicated in the image. Here the 50% case indicates that 50% of the single orifice area is open.

As highlighted in the previous section, the resonance frequency of the Helmholtz resonator can be altered either by changing the volume of the cavity or by adjusting the orifice area S, as discussed earlier in Equation (2.4). Nagaya et al. (2001) demonstrates significant shifts in resonant frequencies by completely closing the second orifice in a double-degree-of-freedom (DDOF) application, effectively creating a single-degree-of-freedom (SDOF) cavity below the facesheet. Alternatively, Cherrier et al. (2012) employs two facesheet plates capable of moving with respect to each other, allowing the orifice to open or close entirely on demand, resulting in a shift in absorption to lower frequencies. An example of this geometry can be seen in Figure 2.4 (c and d), where image (c) illustrates staggered facesheets positioned on top of each other to reduce the effective open area of the resonator's neck, while image (d) provides a top view of the reduced area.

Interestingly, Dodge et al. (2023) employs a similar facesheet geometry but with three facesheets, investigating the effect of spacing between them while keeping the overlap fixed. The author finds that sufficient spacing between the plates results in an unchanged resonant frequency compared to the 100% open case, even when staggered (Figure 2.4 (e)). Moreover, there is no loss in sound attenuation, even when the facesheets are staggered in a way that eliminates the effective open area (most right image of Figure 2.4 (e)).

The results from Dodge et al. (2023) found for the impedance of multiple staggered facesheets is very promising as the staggering of the facesheets influence facesheet aerodynamics while maintaining the

acoustic properties. This configuration differs from that of Cherrier et al. (2012) in that there is spacing between the facesheets, and Dodge et al. (2023) uses three facesheets, with the top and bottom locked in position while the middle sheet can be moved to create different percentage open area (POA) configurations, as seen in Figure 2.4 (e). The configuration with the largest spacing between the plates is the most favourable from a sound attenuation perspective, with a spacing of only 0.35 times the hole diameter d. Conventionally, the facesheet thickness is roughly equal to the hole diameter, i.e., $t = d$. Therefore, a spacing of $0.35d$ between facesheets is not very large. Despite the small spacing, the acoustic attenuation properties are not hindered, and the resonant frequency does not experience a significant shift, as shown in Figure 2.5. The attenuation plot even indicates that for some configurations with a lower POA than 100% (i.e., 25%, 50%, and 75%), the attenuation is higher than when the plates are perfectly aligned, with only minimal losses in attenuation for the 0% overlap configuration.

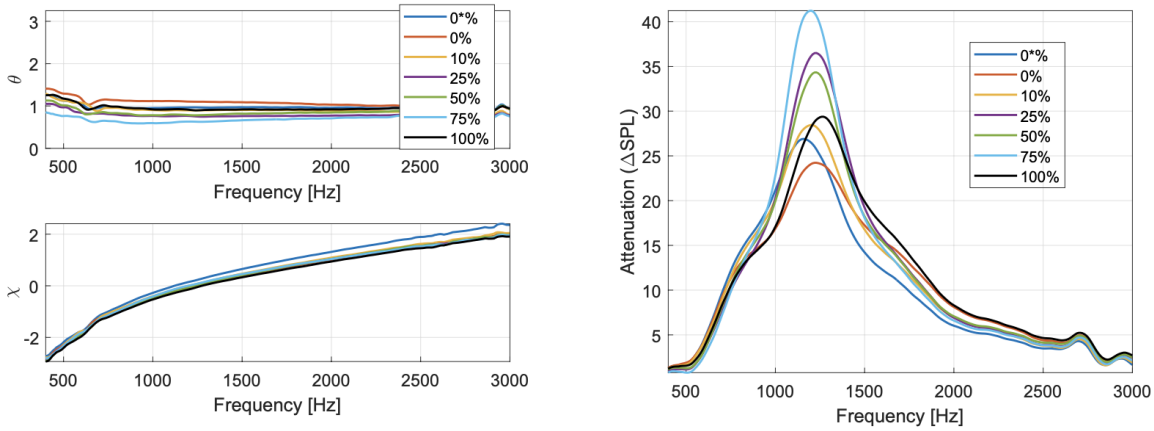

Figure 2.5: Impedance of the tipple facesheet configuration of Dodge et al. (2023) for several POA settings and the largest gap spacing between all three plates of 0.35d.

These papers illustrate the diverse methods employed by researchers to enhance acoustic liners and meet modern standards. Each liner configuration has its own advantages and drawbacks, making one more suitable than another depending on the application. Despite the known increase in drag levels of up to 200% caused by acoustic liners Howerton and Jones (2017), their application persists. While the acoustic properties of liners, particularly impedance, can be predicted accurately, predicting drag, especially over perforated liners, remains a challenge. Many studies resort to experimental measurements or complex simulations.

Given the objective of this review to identify ways to reduce drag in acoustic liners, improving attenuation properties emerges as a potential method. As noted by Howerton and Jones (2017), one of the main contributors to drag in perforated facesheets of acoustic liners is the percentage open area (POA). Unfortunately, the open area is crucial for sound absorption, necessitating the added drag from these holes from an acoustic standpoint. However, improvements in liner efficiency enable a reduction in POA while maintaining similar sound attenuation levels, thereby reducing drag on the liner surface.

For drag reduction purposes, it is crucial to ensure some level of sound absorption, making a more efficient absorber or a change in facesheet beneficial. Studies on variable depth liners and liners with metamaterials show promising results, as they offer enhanced absorption over multiple frequencies. While active liners demonstrate promising results in testing conditions, they face challenges in weight reduction and managing complexities for aircraft use. Passive liners are closer to practical application in engine nacelles. One promising passive configuration for drag reduction, identified by Dodge et al. (2023), involves multiple staggered facesheets that maintain acoustic properties while potentially offering more favourable aerodynamic conditions compared to conventional perforated liner designs due to a smaller open area.

3

Smooth wall turbulence

In order to dive into turbulent flows over acoustic liners, first a general understanding of turbulent flows is desired. This will be followed up by an explanation concerning relevant topics of wall-bounded turbulent flows such that there is a general understanding of the terminology. This will be followed by a discussion of the elaborate study of turbulent flows over rough-wall surfaces in the following chapter. This will enable the reader to better understand relevant concepts. Finally, the focus will be on the turbulent flow over perforated surfaces in the chapter thereafter.

3.1 Turbulent flow

Turbulent flows are characterized by chaotic fluctuations in flow velocity and pressure, resulting in the mixing of multiple layers of fluid. In contrast to laminar flow, turbulence arises from the transfer of energy from the mean flow to chaotic, unsteady turbulent vortices. These vortices overcome the internal friction of the flow induced by viscosity, leading to the division of flow energy into mean and turbulent kinetic energy.

As the energy of the flow can be split into a mean and a turbulent part, the flow velocity can be similarly characterized by this. The splitting of the steady (mean) and the turbulent (fluctuating) part of the flow is more commonly known as the Reynolds decomposition Pope (2000). The Reynolds decomposition decomposes the flow into the mean flow and the fluctuating flow as indicated in Equation (3.1):

$$u = \langle u \rangle + u' \tag{3.1}$$

A visual representation of this decomposition is given in Figure 3.1. The left image shows the total flow velocity (u) and the mean flow velocity, $\langle u \rangle$ as a function of time and at an arbitrary position. As can be seen, the mean flow velocity does not change over time. When the mean flow velocity is subtracted from the total flow velocity, the velocity fluctuations, u_i', are found. In turbulent channel flow, there is no mean flow in the spanwise or wall-normal direction, however, due to turbulent fluctuations, u_2' and u_3' are present.

As mentioned above, the kinetic energy of the turbulent fluctuations can be found in the flow. The turbulent kinetic energy is often indicated with TKE or k (3.2):

$$k = \frac{1}{2}\langle (u_1'^2 + u_2'^2 + u_3'^2) \rangle \tag{3.2}$$

which are combined as the average of the sum of the squares of the fluctuations. The TKE gives an indication of the total turbulent fluctuations at a location in the fluid.

The production, convection, and dissipation of turbulence in the flow, along with the development of mean flow over time, are governed by the Navier-Stokes (NS) equations. These equations constitute a system of partial differential equations that describe the motion of a fluid, based on the conservation of mass and momentum balance. Given the focus on acoustic liners in the current work, the compressible Navier-Stokes equations for a perfect heat-conducting gas, as implemented by Bernardini et al. (2021)

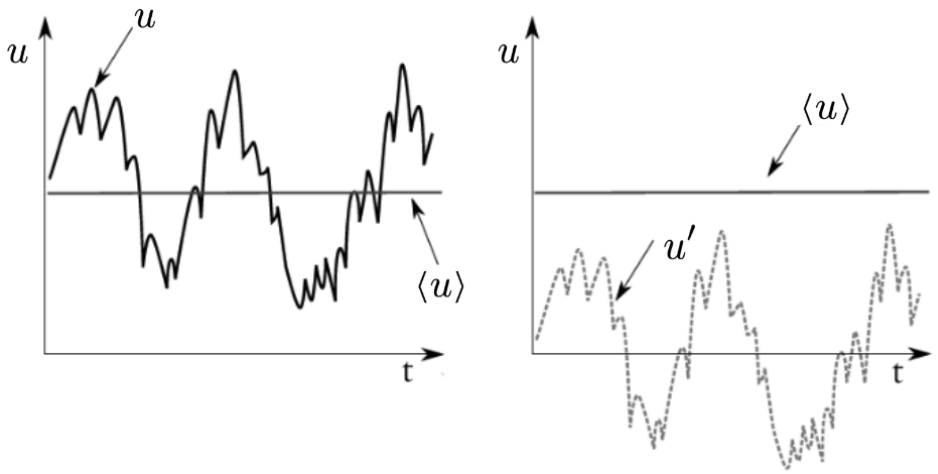

Figure 3.1: Visual representation of the Reynolds decomposition. The Left image shows the total and the mean flow. The right image shows the decomposed elements. (from Reggente (2014))

in the STREAmS DNS code for channel flow, are presented. These equations include the conservation of mass (3.3), momentum (3.4), and total energy (3.5).

$$\frac{\partial \rho}{\partial t} + \frac{\partial \rho u_i}{\partial x_i} = 0 \tag{3.3}$$

$$\frac{\partial \rho u_i}{\partial t} + \frac{\partial \rho u_i u_j}{\partial x_j} = -\frac{\partial p}{\partial x_i} + \frac{\partial \sigma_{ij}}{\partial x_j} + f\delta_{i1} \tag{3.4}$$

$$\frac{\partial \rho E}{\partial t} + \frac{\partial u_i H}{\partial x_j} = -\frac{\partial q_j}{\partial x_j} + \frac{\partial \sigma_{ij} u_i}{\partial x_j} + f u_1 + f_T \tag{3.5}$$

Here ρ is the fluid density and the i (and j) subscript in u_i can be $i, j = 1, 2, 3$ and denotes the fluid direction. p, in (3.4), denotes the pressure and the total energy per unit mass in (3.5) is defined as:

$$E = c_v T + \frac{u_i u_j}{2} \tag{3.6}$$

In the same equation, the total enthalpy ($H = E + p/\rho$) is found, together with σ_{ij} and q_j. These constitute the viscous stress tensor and the heat flux and are defined as (3.7) and (3.8), respectively:

$$\sigma_{ij} = \mu\left(\frac{\partial u_i}{\partial x_j} + \frac{\partial u_j}{\partial x_i} - \frac{2}{3}\frac{\partial u_k}{\partial x_k}\delta_{ij}\right) \tag{3.7}$$

$$q_j = -k\frac{\partial T}{\partial x_j} \tag{3.8}$$

Finally, both (3.4) and (3.5) contain a forcing term f which only operates in the streamwise direction. This is a uniform body force which drives the flow downstream. The forcing is being adapted at every time step to ensure a constant mass flow through the channel. The added energy of the forcing is accounted for in the right-hand side of (3.5). Additionally, there is a uniform, bulk cooling term added to (3.5) in order to attain a constant bulk flow temperature. The bulk quantities are volume averages over the entire domain. These are defined as:

$$u_b = \frac{1}{\rho_b V}\int_V \rho u_1 dV \quad \text{and} \quad T_b = \frac{1}{\rho_b u_b V}\int_V \rho u_1 T dV \tag{3.9}$$

Representing the bulk velocity and temperature respectively. ρ_b is the bulk density, which is found by taking a similar average over the volume of only the density (i.e. $\rho = \frac{1}{V}\int_V \rho dV$). Note that $V = L_x \times 2\delta \times L_z$, which is the entire domain for a smooth wall channel. The volume of orifices or the gap between plates is therefore omitted in the computation of volumetric averages.

This section gives a brief overview of the governing fluid flow equations used in the DNS code of Bernardini et al. (2021). The equations can be combined with numerical schemes, like one of those as have been described by Pirozzoli (2010), to resolve the flow in space in time, given the appropriate mesh resolution. The method of spatial and temporal discretization along with the order of accuracy and the flow statistics are discussed in the methodology in more detail.

3.2 Turbulent channel flow

Turbulent flows encountered in practice are often bounded by surfaces, such as vehicles moving through fluids (e.g., cars, ships, and aircraft), as well as flows in channels and pipes commonly found in industrial applications. This work focuses on fully developed turbulent channel flow, a concept integral to the development of turbulent wall-bounded flow theory. In essence, fully developed turbulent channel flow refers to the flow through a channel bounded by walls at the top and bottom of the domain (i.e., $y = 0$ and $y = h = 2\delta$, where h represents the channel height as depicted in Figure 3.2). The boundaries in the streamwise (x) and spanwise (z) directions are periodic, with the domain extending L_x by L_z in length and width, respectively. The term 'fully developed' implies that the mean flow is spatially homogeneous in the streamwise direction (x), as the boundary layer height is equal to the channel half width. Additionally, the flow is statistically homogenous in the stream and spanwise direction (z)

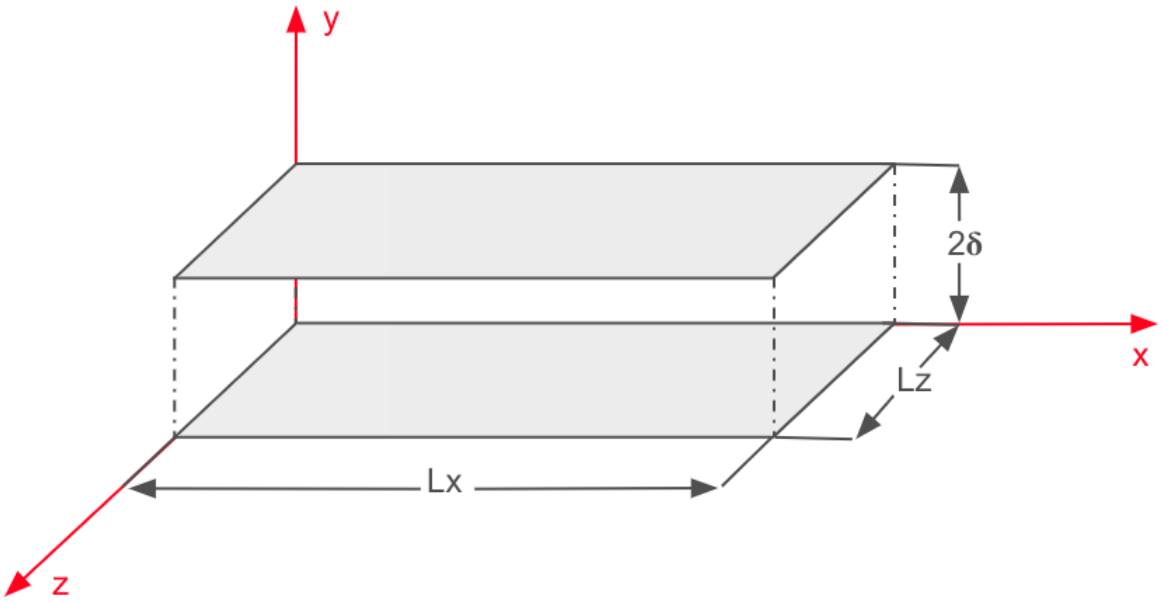

Figure 3.2: Schematic representation of a channel flow domain with the dimensions $L_x \times L_y \times L_z$ where the channel half width is indicated by δ.

The channel half-width is denoted by δ, a symbol commonly used to represent the boundary layer thickness. This is as the channel half-width is equal to the boundary layer thickness inside a channel due to symmetry. In channel flow, two conventions for the Reynolds number are often used. The first, $Re_b = 2\delta u_b/\nu$, represents the bulk Reynolds number, calculated using the bulk velocity u_b (which is the mean velocity of the mass flow through the channel). The second, $Re_0 = \delta u_0/\nu$, is based on the centerline velocity u_0 and the channel half width. The Reynolds number provides insight into the flow state within the channel.

In channel flow, the flow is driven by an axially constant mean pressure gradient. Derivation of the mean momentum equation yields (3.10) (Pope (2000)):

$$\frac{dp_x}{dx} = \frac{d\tau}{dy} \tag{3.10}$$

which describes the total shear stress (3.11) as a function of y, denoted as $\tau(y)$. This total shear stress can be decomposed into viscous and Reynolds stress terms. Close to the wall, viscous stresses dominate due to the large velocity gradient. At the wall, where all velocities are zero due to the no-slip condition, only the viscous term remains. Moving away from the wall, Reynolds stresses become dominant as the velocity gradient decreases with increasing y. A visual representation of this phenomenon, adapted from Pope (2000)), is provided in Figure 3.3.

$$\tau = \rho\nu\frac{d\langle u_1(y)\rangle}{dy} - \rho\langle u_1' u_2'\rangle \tag{3.11}$$

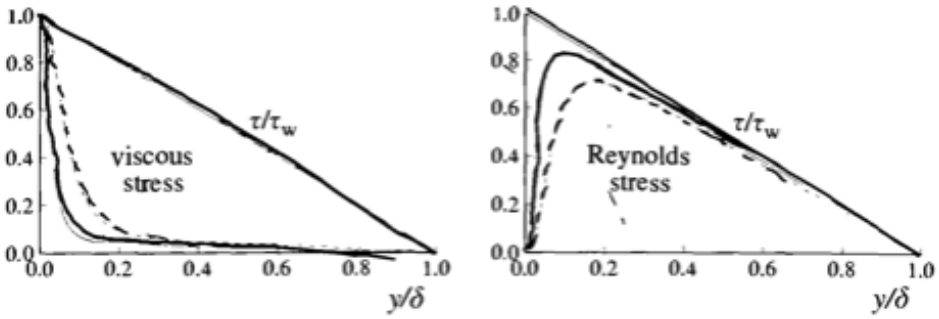

Figure 3.3: Image of the contributions of to the total shear stress form Pope (2000) In the left image it can be seen how the viscous stresses contribute to the total shear stress plotted as a function of wall distance, the same is seen in the right image for the Reynolds stresses. In the figure, the dashed line represents a Reynolds number of $Re = 5600$ and the solid line represents $Re = 13750$.

Figure 3.3 shows which stress in the flow is dominant, depending on the wall distance. The image shows the dependence of both the viscous and Reynolds stresses on the Reynolds number. Increasing values of the Reynolds number ensures less viscous stress in the channel and high shear stress at the wall. The shear stress at the wall is written as seen in (3.12):

$$\tau_w = \rho\nu\left(\frac{d\langle u_1(y)\rangle}{dy}\right)_{y=0} \tag{3.12}$$

This equation gives a good overview of which parameters are of importance close to the wall and leads the way towards the concepts of viscous scaling (also known as friction scaling). This framework identifies the friction velocity u_τ and the viscous length scale δ_ν, as shown in (3.13).

$$u_\tau = \sqrt{\frac{\tau_w}{\rho_w}} \quad \text{and} \quad \delta_\nu = \nu\sqrt{\frac{\rho_w}{\tau_w}} = \frac{\nu}{u_\tau} \tag{3.13}$$

The Reynolds stresses in channel flow contribute to the total mean momentum balance. These stresses are derived from the averaged velocity fluctuations in the flow:

$$\tau_{ij} = \rho\langle u_i' u_j'\rangle \tag{3.14}$$

which describes the Reynolds stress tensor for a homogeneous fluid with constant density. Figure 3.4 displays the corresponding values of the Reynolds stress relative to the wall distance. As can be seen from the image, the Reynolds stresses are zero at the wall, due to the no-slip condition, in correspondence with Figure 3.3. The Reynolds stresses are indicative for the main region of the production of turbulent kinetic energy (3.15)), (which reduces to only $P = \langle u_1' u_2'\rangle\frac{\partial\langle u_1(y)\rangle}{\partial y}$ in the boundary layer approximation). Due to the large peak in the stream-wise velocity fluctuations it can be seen that most of the turbulence production is situated close to the wall where velocity gradients cause shearing flow.

$$P = -\langle u_i' u_j' \rangle \frac{\partial \langle u_i \rangle}{\partial x_j} \tag{3.15}$$

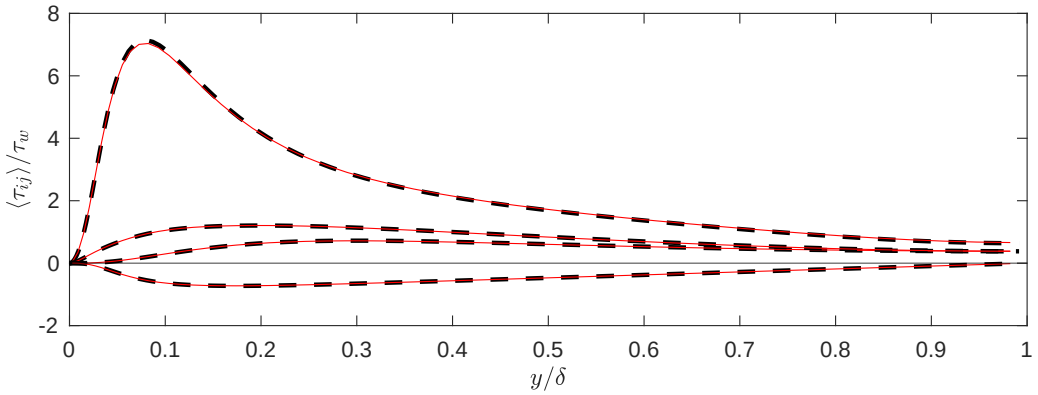

Figure 3.4: Comparison of the normalised Reynolds stresses from DNS simulations for a $Re_\tau = 180$ channel flow (Red lines) compared to Lee and Moser (2015) DNS results (Black dashed lines). The Reynolds stresses in descending order are $\langle u_1' u_1' \rangle$,$\langle u_2' u_2' \rangle$, $\langle u_3' u_3' \rangle$ and $\langle u_1' u_2' \rangle$.

The skin friction coefficient represents the nondimensional wall-shear stress and it is a primary quantity for engineering design. The definition of the friction coefficient is found in (3.16):

$$C_f = \frac{2\tau_w}{\rho u_b^2} \tag{3.16}$$

Where in this instance the bulk velocity (u_b) is used. Some authors tend to use the centre line velocity for the friction coefficient which bids some caution when making comparisons based on the friction coefficient. The coefficient however is useful to assess and compare the added friction of a wall.

Law of the wall

A useful indication for flow conditions can be found by the combination of (3.12) and (3.13) such that the friction Reynolds number can be written as (3.17).

$$Re_\tau = \frac{u_\tau \delta}{\nu} = \frac{\delta}{\delta_\nu} \tag{3.17}$$

Where the friction Reynolds number is equal to the viscous scaled boundary layer thickness. This gives an indication of the range of scales present in the boundary layer and increases with increasing friction velocity. The same scaling can be applied to the wall distance, y, by normalizing it with the viscous length scale to obtain $y^+ = y/\delta_\nu$. This dimensionless quantity is a valuable tool for identifying different regions within the flow. Specifically, it delineates the various regimes present in the flow. Close to the wall, the viscous sub-layer is found for $y^+ < 5$, while the buffer layer exists for $5 < y^+ < 30$. The buffer layer lies between the viscous sub-layer and the log layer, which extends from $30 < y^+$ to $y/\delta < 0.3$, with the outer layer encountered beyond $y^+ = 0.3$.

Prandtl (1925) has introduced that at high Reynolds number, close to the wall (i.e.$y << \delta$), an inner layer can be found where the velocity merely depends on the viscosity while the boundary layer thickness and the centre line velocity have no influence. After some computation, this entails that there is a function f_w for which $u^+ = f_w(y^+)$ Pope (2000). This means that the viscous scaled velocity, close to the wall, at high enough Reynolds number is merely a function of the wall distance. This is commonly known as the law of the wall. The viscous scaled regions are of importance for the law of the wall. This concept was first proposed by von Karman (1930). It is used as a universal law to relate the viscous scaled velocity to the viscous scaled wall distance in the boundary layer.

In the viscous sub-layer ($y^+ < 5$), the viscous scaled velocity is equal to the viscous scaled wall distance (i.e. $u^+ = y^+$), where $u^+ = u/u_\tau$. Due to negligible terms in the Taylor series expansion for u^+, the

behaviour is linear for small y^+ but deviates as y^+ increases beyond 5, as illustrated in Figure 3.5. Beyond the viscous sub-layer, the buffer region ($5 < y^+ < 30$) lacks a universally accurate description of flow solely dependent on y^+.

From $y^+ > 30$ however, the logarithmic layer is found. This layer corresponds to larger values of y^+, where the length of the log layer is determined by the Reynolds number. As can be seen in Figure 3.3, the effect of viscosity away from the wall vanishes. In the logarithmic region, through integration of the mean viscous scaled velocity gradient, the logarithmic law is found (3.18) by von Karman (1930):

$$u^+(y^+) = \frac{1}{\kappa} ln(y^+) + B \tag{3.18}$$

In this equation, κ resembles the von Kármán constant, where $\kappa = 0.387 \pm 5\%$ is generally found in literature. In the log law, B is generally found to be $B = 4.8 \pm 5\%$ Pirozzoli et al. (2022). Both these values are found through a DNS data fit of the mean axial velocity of a pipe flow. As can be seen from Figure 3.5 from $y^+ < 30$ the velocity profile of the DNS results starts to follow the log law very closely until the flow enters the outer layer. In DNS studies performed at several friction Reynolds numbers, like that of Lee and Moser (2015), it can be seen that all velocity profiles collapse onto each other for the inner layer of the boundary layer flow, indicating the universality of the law of the wall.

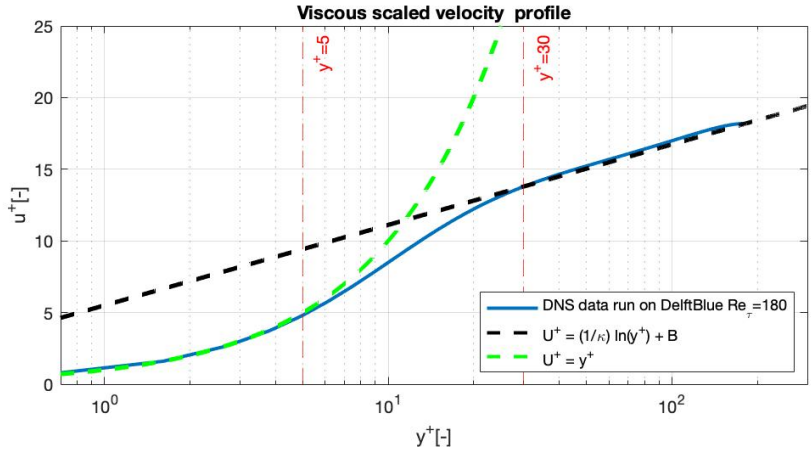

Figure 3.5: The log law and u^+ for the viscous sub-layer plotted along near wall results of a DNS simulation performed by the author based on Lee and Moser (2015) for $Re_\tau = 180$. The velocity profile is the velocity profile found in the half of the channel flow and is scaled by viscous units.

4

Rough wall turbulence

Hydraulically rough walls commonly occur in engineering applications. The term hydraulically rough or smooth is used to indicate that the 'smoothness' of a surface is not directly determined by a physical length scale. It is not possible to say whether a surface is smooth or rough, in a fluid mechanics framework, without making an observation of the flow next to it. For a turbulent flow, the surface is conceived as a rough surface when the roughness elements (surface fluctuations) of the wall, are large enough to alter the smallest near-wall eddies of the flow. In this situation, the momentum transfer in the flow is altered and the effect of the wall on the flow can be perceived. Depending on the flow and especially the Reynolds number, the surface can be either smooth or rough. The effect of a rough wall can be monumental when it is found on the surface of a ship or aircraft causing large losses in efficiency. These losses are generally expressed in drag of the surface and can have large effects on fuel economy and costs.

Unfortunately, the prediction of the drag caused by a rough surface is not as clear-cut as the drag prediction of a smooth wall. This is due to the interaction of the roughness topography with the flow, where flow over each roughness topography behaves differently and therefore causes different near-wall flows and ultimately different drag levels. The study of roughness is therefore mainly focused on finding relevant surface parameters which can be used to predict the effect of the specific roughness topography on the flow. Generally, a roughness topography found in industry is not a monotonically rough surface and can be unique on its own. Therefore the study of surface roughness is very complicated and elaborate and is currently an area where a lot of research is conducted (Chung et al. (2021)).

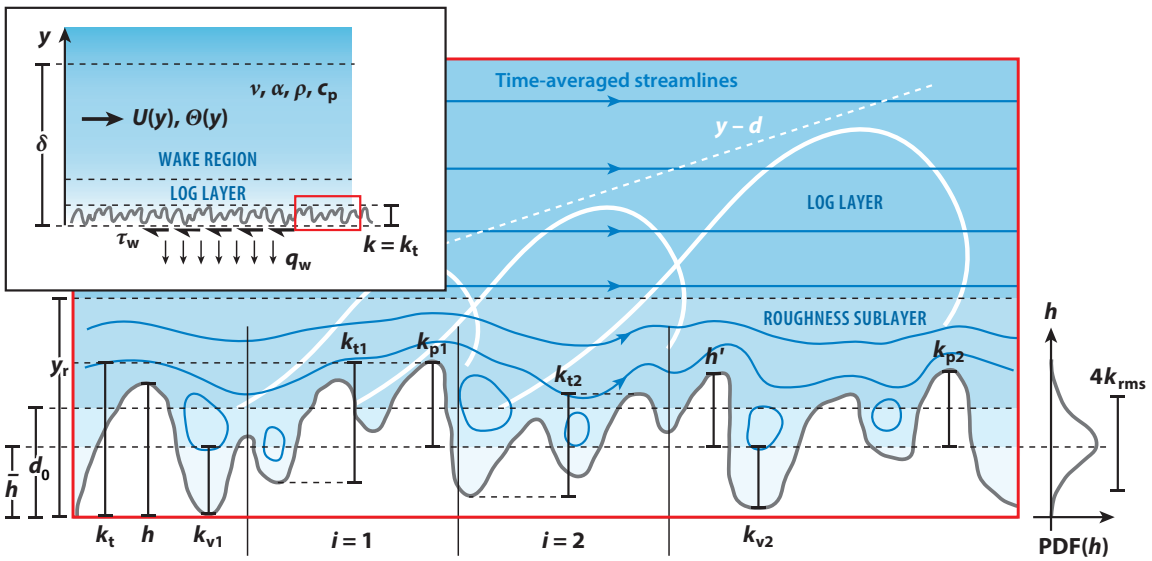

Figure 4.1: Image taken from Chung et al. (2021) showing a typical, arbitrary, rough wall topography with its respective flow features.

Understanding rough wall turbulence requires familiarity with relevant terminology and concepts. This

includes discussing flow over perforated/porous surfaces in a rough wall framework and examining current research on the effect of perforated surfaces on added drag compared to smooth surfaces.

To introduce the concept of rough wall turbulence, The discussion starts with a graphical representation of a rough surface topography and its interaction with the flow, borrowed from Chung et al. (2021). This illustration, provided in Figure 4.1, depicts a typical, arbitrary rough wall topography.

In the larger image of the figure, roughness elements large enough to interact with the flow's length scales are presented. Some flow elements lay between these roughness elements, causing the flow above the surface to perceive the wall as rough.

The study of roughness aims to determine the drag per plane area (τ_w) at the rough surface and define the velocity profile as a function of the wall distance y and roughness element properties. These properties are shown in Figure 4.1. The roughness height (k) measures the maximum distance from peak to trough height, while δ represents the boundary layer thickness beyond which the mean fluid velocity remains constant with increasing y. The origin of the wall is defined at $y = 0$, and the wall offset (d) indicates the location where the fluid perceives its origin for a rough wall. The roughness sub-layer, depicted by $y_r > y$ in the figure, is where roughness no longer directly influences the mean flow.

The smaller inset in the top left provides an overview of the total boundary layer flow, divided into the wake region, the log layer, and the roughness sub-layer. These concepts will be further elaborated on in subsequent discussions.

In studies of flow near walls, the roughness height (k) is scaled using the same principle as used for the viscous scaling of the wall distance, as $k^+ = ku_\tau/\nu$. This parameter is often termed the roughness Reynolds number and can be expressed as $k^+ = k/\delta_\nu$. The viscous scaled roughness height (k^+) is therefore dependent on the flow, determining its magnitude and relevance.

According to Chung et al. (2021), the roughness problem aims to determine the surface drag (τ_w, drag per unit area) as a function of y^+ and k^+, outlined by (4.1). Obtaining the mean velocity profile of rough-wall flow ($u^+(Y^+, k^+)$) is crucial for determining surface drag.

$$\frac{\tau_w}{0.5\rho u^2} = \frac{2}{u^{+2}} \tag{4.1}$$

The following sections will explore the phenomena briefly introduced in Figure 4.1. Firstly, there will be an explanation of the wall offset. This concept aids the discussion of how the velocity profiles can be displaced due to the influence of the roughness elements. Following this, the region of influence of the roughness elements, known as the roughness sublayer, will be addressed. Subsequently, a brief explanation of sandgrain roughness will be provided. The sand grain roughness is a relevant length scale for characterizing roughness elements. This will lead to a discussion of the region outside the roughness sublayer, where, given sufficient separation of scales, outer-layer similarity can be observed. The concept of outer layer similarity will be explained and there is a discussion of how it is leveraged to determine performance parameters used to evaluate the added drag of rough surfaces. Done through the law of the wall and the Hama roughness function. The subsequent chapter will delve into studies conducted to address the more specific roughness problem tailored to acoustic liner aerodynamics.

Wall offset

Figure 4.1 illustrates the concept of zero plane displacement with the parameter d_0. Zero plane displacement, or wall offset, is crucial for addressing outer layer similarity. It represents the origin of the boundary layer encountered by the outer flow. Although the actual wall may be at $y = 0$, the flow perceives the origin of the boundary layer to be at $y = d_0$. This adjustment accounts for the presence of roughness elements, which can render the fluid between them relatively stationary.

Determining the value of d_0 is challenging as it depends on the specific flow conditions. Therefore d_0 is a consequence of the flow rather than a quantity which can be predicted. Studies by Jackson (1981), Cheng and Castro (2002), Castro (2007), Coceal et al. (2007), and Chan-Braun et al. (2011) have explored this parameter's variability.

The wall offset facilitates the collapse of velocity profiles from different topographies onto each other. Although the flow perceives the wall offset as the origin of the flow, this does not necessarily mean that $u(y = d_0) = 0$. This is especially the case for small roughness elements (small k^+), where d indicates the

location where mostly intact, smooth wall-like turbulence is encountered. Here the wall offset effectively creates a slip wall, reducing drag. This is generally seen with grooved surfaces or surfaces containing riblets as found by Bechert et al. (1997), Luchini et al. (1991) and García Mayoral et al. (2018).

With increasing k^+, roughness elements begin to affect near-wall turbulent structures. Generally, d_0 falls between the highest and lowest points of the roughness elements. For densely distributed roughness, d_0 is closer to the highest point, while for sparsely distributed roughness, it is closer to the lowest point of the roughness elements. When roughness spacing approaches the viscous length scale, d_0 approaches the peak of the roughness elements MacDonald et al. (2016). Similar behaviour is observed in canopy-like roughness by Sharma and García-Mayoral (2020).

In canopies, as roughness spacing decreases, d_0 decreases too, influenced by Kelvin–Helmholtz-like instabilities perturbing between roughness elements. These instabilities enhance Reynolds shear stress and skin friction. The depth of the canopy influences these instabilities, with shallow roughness hindering their development. When canopy depth is significantly greater than lateral spacing, instabilities do not reach the bottom of the trough, akin to the near-wall flow over a highly porous surface Breugem et al. (2006).

Roughness sub-layer

The extent to which the near-wall flow is affected by the roughness is highly dependent on the roughness topography. The region which is affected by the roughness is called the roughness sub-layer denoted by y_r and indicated in Figure 4.1. The height of the roughness sub-layer is dependent on the roughness on the surface. Where the region within y_r is influenced by the surface topography while the region outside does not encounter direct effects of the roughness.

The roughness sub-layer can be defined as the, wall-normal, wall spacing where the (time-averaged) flow becomes spatially homogeneous. This homogeneity pertains to the mean flow, requiring less scale separation than turbulent fluctuations (outer layer similarity) Flack and Schultz (2014), Chan et al. (2018). The height of y_r is determined by identifying the point normal from the wall where the mean flow becomes homogeneous Raupach et al. (1980). However, y_r cannot be determined a priori as it is contingent on flow conditions, similar to wall offset determination.

Jiménez (2004) and Raupach et al. (1991) proposed a roughness sub-layer thickness of $y_r \in [2k - 5k]$, but the specific roughness height is not specified. Flack et al. (2007), however, suggested expressing y_r in terms of sand grain roughness height (k_s). Their findings indicate the roughness sub-layer exists for $y_r < 3k_s$ but not beyond $y_r = 3k_s$ or $y_r = 5k$. Using sand grain roughness provides a topography-independent definition of the roughness sub-layer. Yet, it remains a flow-dependent parameter, as the equivalent sand grain roughness is determined by the flow conditions.

Sand grain roughness

Sandgrain roughness is often used as a reference roughness type with uniform elements. The roughness consists of uniformly spaced and sized roughness elements. An illustration of a sand grain roughness topography is depicted in Figure 4.2. This representation closely resembles densely packed sand grains akin to sandpaper-like roughness on a hypothetical surface. The sand grain roughness is employed in roughness studies to attain a uniform roughness type to which arbitrary rough wall topographies can be related. This is done by defining the respective equivalent sand grain roughness height k_s.

The equivalent sand grain roughness height serves as a valuable parameter for characterizing rough wall surfaces. The concept of equivalent sand-grain roughness has first been applied to match the data of Nikuradse (1933) by Schlichting (1937), describing roughness as uniformly distributed elements of various shapes, uniformly spaced and sized. At sufficiently high Reynolds numbers, the equivalent sand grain roughness height is selected such that the surface induces the same drag as the original topography under identical flow conditions. The sand grain roughness is not a physical quantity but rather a flow consequence resulting from a specific roughness topology. Its key advantage lies in providing a uniform method to address the effect of a roughness topography on the flow.

As mentioned, sand grain roughness aids in determining the roughness sub-layer thickness, denoted by the "s" subscript in (Figure 4.2). Analogous to the regular roughness Reynolds number for k^+, the sand grain roughness Reynolds number is defined as $k_s^+ = k_s u\tau/\nu$, scaling the sand grain roughness height with the viscous length scale δ_ν.

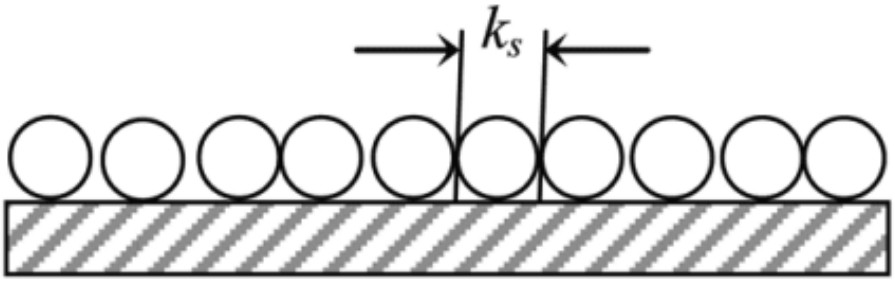

Figure 4.2: Schematic figure of the equivalent sand grain roughness. (from Hetsroni et al. (2011))

Outer layer similarity

Outer layer similarity is a concept first proposed by Townsend (1956) and worked out by Raupach et al. (1991). The latter provided strong support for the outer layer similarity. The outer layer similarity dictates that for sufficiently high Reynolds number, both smooth and rough wall flows, outside the viscous or roughness sub-layer respectively, show the same turbulent structure. This implies that statistical quantities are independent of the surface conditions, a premise that, when valid, greatly facilitates simulations by allowing the outer flow to be modelled rather than explicitly simulated Flack and Schultz (2014).

However, achieving outer layer similarity requires a sufficient separation of scales. This occurs when $\delta \gg \delta_\nu$ (i.e., sufficiently high Re_τ) and $\delta \gg k$. Under these conditions, the outer layer is not directly influenced by surface roughness effects, but rather experiences the effects of roughness on the sub-layer, thereby establishing boundary conditions for the outer layer flow. It has been proposed by Jiménez (2004) that a blockage ratio of at least $\delta/k = 40$ is necessary, although some experiments suggest that this value may need to be doubled before observing similarity in the outer layer flow. Numerous studies, including those by Flack et al. (2005), Castro (2007), Amir and Castro (2011), and Krogstad and Efros (2012), have established the existence of outer layer similarity.

Despite efforts to establish definitive criteria for sufficient scale separation, prescribing guarantees remains challenging. To ensure sufficient scale separation, tests can be conducted at larger scale separations (with fixed k^+) and the outer layer flow can be assessed. If unchanged, the original scale separation can be deemed sufficient. Flack and Schultz (2014) provides a comprehensive review of the literature on outer layer similarity, consolidating findings from numerous studies.

4.1 Law of the wall and added drag

In line with the discussion on smooth-wall turbulence, the law of the wall represents a fundamental principle that relates the mean viscous-scaled velocity in the boundary layer to the viscous-scaled wall distance, initially proposed by von Karman (1930). In the context of roughness, the wall is considered smooth when the roughness is significantly smaller than the thickness of the viscous sub-layer.

When rough walls are of interest, the log law is also used for the relation of the velocity with the wall distance. In this section however, there is a distinction between the smooth and the rough wal log law which will be denoted with the "S" subscript for the smooth wal in (4.2) and "R" for the rough wall in (4.3).

$$U_S^+ = \frac{1}{\kappa} ln(y^+) + A \tag{4.2}$$

In the logarithmic function for smooth walls, a subscript "S" is used to denote the log law for a smooth wall. The constants associated with smooth walls have been extensively studied in the literature, with a consensus on the range of their values. The von Karman constant proposed by Pirozzoli et al. (2022) of $\kappa = 0.387 \pm 1\%$ represents the slope of velocity profile in the log layer, and the wall intercept of the log law is around $A = 4.8 \pm 1\%$ (derived from $U_S^+(y^+ = 1) = A$).

The log law represents one of the most crucial concepts utilized in wall-bounded turbulence studies, particularly for assessing the added drag resulting from roughness effects. The log law applies to both rough and smooth walls owing to the concept of outer layer similarity. In cases where k^+ is not substantially smaller than the viscous length scale, the wall is no longer considered smooth. The roughness height surpasses the viscous sub-layer, and the flow perceives the wall as rough. In such instances, y must lie outside the roughness sub-layer ($y >> y_r$) for the log law to be applicable. Subsequently, the viscous-scaled velocity for the rough wall is determined by (4.3), denoted by the subscript "R":

$$U_R^+ = \frac{1}{\kappa} ln(\frac{y}{k}) + B(k^+) \tag{4.3}$$

Here, y is scaled by k due to integration, and the wall intercept B becomes a function of both the roughness Reynolds number k^+ and the specific roughness topography. It is important to note that the argument of the logarithm is not in plus units due to cancellation of the viscous length scale. For very high roughness Reynolds numbers ($B(\infty)$), B may approach a constant value dependent solely on the surface topology, only in cases where the fully rough regime is attained.

To obtain the log law in boundary layer flow, outer layer similarity is necessary however it is not sufficient for the observance of the logarithmic behaviour. The boundary layer thickness must be large enough such that the logarithmic region is well within the boundary layer(i.e. $y \ll \delta$). Therefore the log law is observed in the region outside the roughness sub-layer but within the boundary layer. Oftentimes, the observation of the log law is used as the establishment of outer layer similarity however the observation of outer layer similarity is not necessarily evidence that there will be a logarithmic region in the boundary layer since outer layer similarity can be observed for δ and y much closer to k (Castro (2007), Amir and Castro (2011), Chan et al. (2015)).

Hama roughness Function

A way to provide an appropriate value for $B(k^+)$ is to use the roughness function which has been defined by both Hama (1954) and Clauser (1954). The roughness function is commonly referred to as the Hama roughness function so this termination will be used interchangeably in this review.

The Hama roughness function evaluates the deviation between the smooth and rough wall log laws, as expressed in (4.2) and (4.3), respectively. This function assesses the shift of the logarithmic region at a specific y^+ value by comparing the viscous-scaled velocity deficit between smooth and rough wall configurations. Figure 4.3 presents an illustration of the comparison of velocity profiles for various roughness types, comparing the velocity profiles of a smooth wall with those of roughness topographies.

The Hama roughness function, presented in (4.4) is found through the difference of (4.2) and (4.3) to obtain:

$$\Delta U^+(k^+) = U_S^+ - U_R^+ = \frac{1}{\kappa} ln(k^+) + A - B(k^+) \tag{4.4}$$

This equation quantifies the velocity deficit of the rough wall relative to the smooth wall, thus providing insight into the drag penalty associated with surface roughness. A positive value of ΔU^+ indicates an increase in drag due to roughness, while a negative value suggests a drag reduction.

Moreover, the Hama roughness function articulates the difference in smooth and rough-wall skin-friction coefficients at matching δ^+, denoted by (4.5):

$$\sqrt{\frac{2}{Cf_s}} = U_{s\delta}^+ \quad \text{and} \quad \sqrt{\frac{2}{Cf_r}} = U_{r\delta}^+ \tag{4.5}$$

Utilizing this function is particularly relevant for scaling experimental or numerical data to real-world applications at lower Reynolds numbers, as noted by Chung et al. (2021). The velocity deficit between rough and smooth wall surfaces remains independent of the length of the log layer, as the slope of both log laws remains equivalent, with only the wall intercept changing. However, according to Chan et al. (2015), Thakkar et al. (2018), and Jiménez (2004), a minor caveat exists when the log layer is relatively small (low Re_τ). In such cases, the roughness function may still exhibit slight dependence on the boundary layer thickness, resulting in a maximum overestimation of ΔU^+ by 1.

As can be seen from (4.4), which has not been discussed in detail, is that the equation is a function of the roughness Reynolds number k^+. The relation of the roughness function with the roughness height is fairly intuitive when taking the previous discussion concerning the roughness sub-layer into account. When k^+ is small, the flow perceives a (hydraulically) smooth wall and there is no added drag (i.e. $\Delta U^+ = 0$). This is due to the roughness elements being too low to perturb out of the viscous sub-layer and the viscous damping ensures a hydraulically smooth wall. From a certain value of k^+, dependent on the roughness topography ($k_s^+ > 5$ more specifically), the roughness effect on ΔU^+ occurs. From this k^+, the roughness ensures a transitionally rough flow which is both influenced by the pressure and viscous drag contributions. When k^+ is increased more, the flow enters the fully rough regime where the pressure drag prevails over the viscous drag Schlichting (1968).

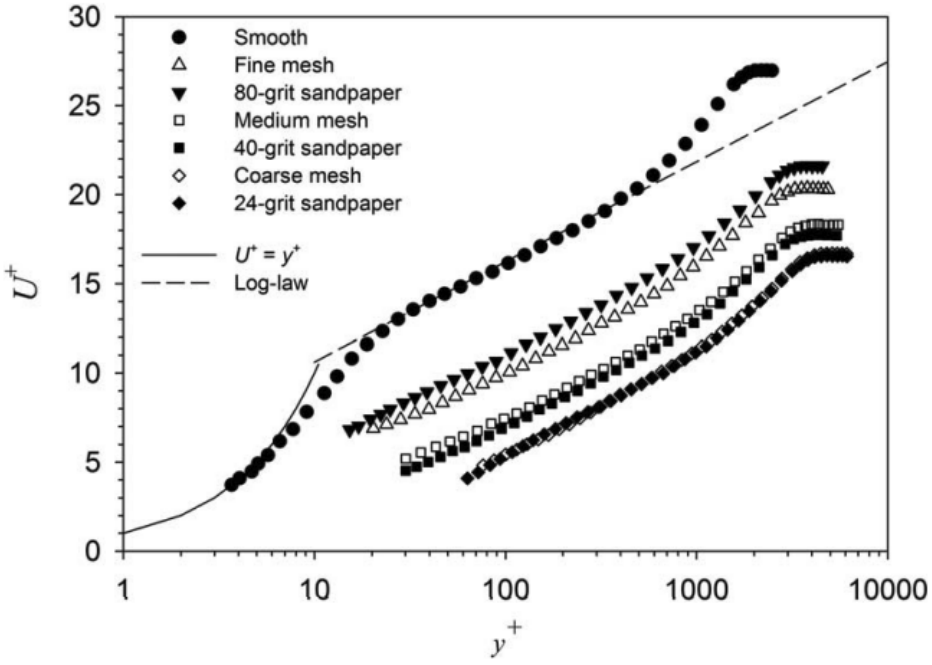

Figure 4.3: The roughness function plotted for a smooth wall and various types of roughness. (from Flack et al. (2007))

The fully rough regime holds particular significance, as beyond this point, ΔU^+ and thus skin friction become independent of the Reynolds number (Re_0), provided that k/δ remains constant. This phenomenon, established by Nikuradse (1933) and Colebrook (1939), formed the basis for the renowned Moody diagram, showcasing the asymptotic behaviour of skin friction with increasing Reynolds number across different (pipe) roughness types.

The discussion on the Hama roughness function gives many insights into why the prediction of drag acting on rough surfaces is so difficult. As the rough wall logarithmic function does not find a universal wall intercept $B(\infty)$ in the fully rough regime. Even worse, each roughness topology produces a different wall intercept and behaves differently in the transitionally rough regime as can be seen from Figure 4.3. So it is not possible to make predictions for the drag based on k^+. In order to attain universality in a roughness height, k_s is used.

Firstly, (4.3) can be formulated with the use of the sand grain roughness Reynolds number k_s^+. This takes the form of (4.6):

$$\Delta U^+(k_s^+) = \frac{1}{\kappa} ln(k_s^+) + A - B_s(k_s^+) \tag{4.6}$$

where instead of $B(k^+)$ we now have $B_S(k_s^+)$ as the wall intercept. The crucial difference between the two, however, is that since the sand grain roughness is only one specific type of roughness topology, the wall intercept in the fully rough regime is found at a set value, that is $B_s(\infty) = 8.5$. Since the roughness function can be described through both kinds of roughness, the roughness k can be related to the sand

grain roughness k_s. This uses the wall intercept for both equations and when evaluated in the fully rough regime, the ratio of roughness types is found to be as (4.7) (Chung et al. (2021)):

$$\frac{k_s}{k} = exp(\kappa(B_s(\infty) - B(\infty))) \tag{4.7}$$

Therefore the function is independent of the roughness Reynolds numbers. When the ratio is used as a pre-factor in the argument of the logarithm the roughness function for k^+ can be made to coincide with the roughness function of the sand grain roughness.

5

Aerodynamic performance of acoustic liners

Through the previous discussion, it has been established that the equivalent sand grain roughness height is an appropriate length scale for drag prediction over rough surfaces. As mentioned, however, the equivalent sand grain roughness height is a result of the flow and therefore is not a physical property of the roughness topography Nikuradse (1933). This makes it difficult to predict the drag before conducting measurements or simulations. Chung et al. (2021), Flack and Schultz (2010) have performed a comprehensive summary of all attempts to correlate the topography to sand grain roughness.

Given the focus of this thesis on the aerodynamic properties of acoustic liners, it is imperative to extract three key components from the literature to assess the current research status. Firstly, previous studies on acoustic liner drag provide essential insights. Secondly, understanding the relationship between (sand-grain) roughness height and topographical features of porous surfaces is crucial for correlating them with ΔU^+ and subsequent drag reduction. Additionally, identifying flow phenomena responsible for acoustic liner drag enables the devising of effective drag reduction mechanisms. This will culminate in a discussion on known (added) drag reduction mechanisms and how these can be leveraged to attain a more favourable liner.

Liner drag studies

Recent research papers have extensively explored the flow over porous plates, focusing on identifying parameters governing added drag while maintaining desired sound attenuation levels. For instance, Zhang and Bodony (2016) conducted Direct Numerical Simulations (DNS) to examine how the presence of porous surfaces affects grazing flow. Their findings indicate a drag increase over smooth-wall configurations with increasing Sound Pressure Level (SPL). However, it is worth noting that their simulations, limited to a single cavity to reduce computational costs, may overestimate the effect of sound levels on drag.

Howerton and Jones (2015), Howerton and Jones (2016) and Howerton and Jones (2017) have performed a series of wind tunnel experiments measuring the static pressure drop over the test section. Focusing on the reduction of added acoustic liner drag and evaluation of acoustic performance. The first study is more a proof of concept of the test methods, while the second and third studies test the effect of certain parameters and typologies, respectively. The conclusion is in line with the findings from Zhang and Bodony (2016) in the sense that all liner geometries add drag compared to smooth wall configuration.

However, the experiments do not perceive large differences between situations with and without sound indicating that due to the single cavity, the effect of the sound could indeed be overestimated. The papers from Howerton and Jones do find that the increase of the Percentage Open Area (POA) of the plate increases drag and acoustic attenuation. The percentage open area is the ratio of the area of the orifices to the total area of the liner facesheet, this is often referred to as the porosity of the liner.

In line with the effect of the reduction of POA on added liner drag, the reduction of hole diameter reduces drag with respect to the original liner design. The best-performing results in this study campaign, have been found for rectangular slots, which minimally increase drag while maintaining nearly the same acoustic attenuation capabilities.

Other solutions to minimise the drag impact are found through active liner solutions like Gustavsson et al. (2019). This solution is based on the opening and closing of the orifices when the sound attenuation is needed or not (take-off and landing versus cruise conditions). The closing of the orifices results in a 4% lower pressure drop over the closed orifice plate w.r.t the open plate thus reducing drag.

In line with previous studies, Gowree et al. (2019) discovered that reducing the diameter of three-dimensional staggered circular cavities causes a favourable, monotonic response on the added drag. Moreover, the author reports that a diameter-to-cavity depth ratio smaller than 1 (i.e., $\frac{d}{h} \leq 1$), could, in some cases, even reduce drag. While the reduction in hole diameter leading to lower added drag aligns with prior findings, the reduction of drag compared to the smooth-wall configuration had not been reported previously. This research is corroborated by Scarano et al. (2022, 2023), who arrived at similar results. They observed that the thickening of the viscous sub-layer resulted in a decrease in friction velocity.

Despite the promising drag reduction observed in these studies, there is limited focus on the acoustic attenuation aspect of the liners. The perforated plates used in these experiments are sealed at the bottom of the orifices, preventing any fluid from passing through the plate. This difference in the behaviour of skin friction with respect to the orifices will be elaborated on in the following sections. attenuation properties.

Schiller et al. (2019) arrives at a similar conclusion using a slightly different approach. Their objective is to achieve the same sound impedance levels while reducing the open area (porosity). This results in a reduction in added drag and is therefore in line with conclusions from Howerton and Jones (2017) as the reduction of porosity reduces added drag. The reduction of 50% open area resulted in a 75% decrease in added drag compared to the conventional configuration. While the impedance levels are equal, there are some caveats since the impedance is over a broadband of sound frequencies and therefore not very efficient in the attenuation of one specific frequency.

An overview of previous studies concerning the acoustic liner drag is presented in Table 5.1. This gives an indication of the various studies quantifying the added drag results of conventional acoustic liners with their respective geometric properties.

Author	d/δ	h/δ	t/d	σ	Ma	Re_τ	$\Delta D(\%)$
Shahzad et al. (2023)	0.08	0.5	0.5-1	0.036-0.32	0.3	500-2000	70%
Howerton and Jones (2015)	0.025-0.05	1.8	1	0.08	0.3-0.5	7800	10-15%
Howerton and Jones (2016)	0.036	1.8	1	0.08	0.3-0.5	7800	80-130%
Howerton and Jones (2017)	0.036-0.084	1.8	1	0.1-0.3	0.3-0.5	7800	200-350%
Zheng et al. (2022a)	0.0188-0.0353	0.0188-0.0282	1-2	0.075-0.2	0.1-0.6	~3000-12000	$\leq$ 137%
Zhang and Bodony (2016)	0.05	-	-	0.0099	0.05-0.5	6900	4-100%
Wilkinson (1983)	0.075-0.08	0.55-0.7	0.75-1	0.06-0.12	0	500-2000	2-20%
	0.018	0.3-1.85	0.66	0.047-0.139	0	500-200	30-60%
Gustavsson et al. (2019)	0.15-0.17	5.85-6.05	1	0.0853	0.3-0.6	2000-3000	30-50%

Table 5.1: Results of previous studies on the drag of acoustic liners. All of the results resemble grazing flow over different acoustic liners. The relative size of the orifice diameter d, the cavity depth h and the facesheet thickness t w.r.t. the boundary layer thickness have been indicated. σ resembles the porosity factor, Ma is the Mach number and Re_τ is the friction Reynolds number. Eventually, in the last column, the drag increase (with respect to a smooth wall) in percentages are given which are found in all studies. Many of the values presented are not directly indicated in the studies. Some results have readily been extracted by Shahzad et al. (2023) while others have been deducted from figures or calculated from other known quantities of the respective studies.

5.1 Parameter identification

Firstly, the focus is on the identification of relevant parameters present in porous surface studies which influence the drag of the surface. The previous section has indicated some of the more obvious and intuitive parameters which influence the drag. This section will elaborate on those and introduce relevant new parameters.

In previously discussed research, a recurring pattern emerges where a certain level of attenuation is desired, serving as the constraint under which a reduction in liner drag is sought. This requirement

remains a key consideration in this thesis, serving as a stringent criterion for evaluating the suitability of each parameter for reducing added drag. While some studies suggest a trade-off between reducing added drag and maintaining acoustic attenuation in liners (Palani et al. (2021)), the primary trade-off observed typically pertains to the frequency range rather than the total impedance. The suitability of this solution would depend on the intended application for the liner.

In line with studies on rough walls, predicting added liner drag based solely on liner geometry often yields unsatisfactory results. Therefore there is a demand for the identification of relevant scaling parameters which can be used to accurately predict the liner drag. Some promising results in this field are found by Howerton and Jones (2016) and Zheng et al. (2022b) where it is shown that the reduction of the pore diameter alone and its ratio to liner thickness reduces added drag in general. Next to this, the reduction of porosity is found to reduce the added drag in a similar manner where the proportionality is found for a range of Mach numbers (Ma = (0.1 - 0.6)). The geometrical measures sound intuitive as the geometries approach the smooth-wall configuration. A potential drawback is the loss of the sound attenuation properties. Both Howerton and Jones (2017) and Zheng et al. (2022b) have found that a mesh underlayment (fabric-like layer) below the perforated panel can reduce added drag. Although promising, these features however are difficult to quantify as a scaling parameter

In the quest to identify relevant parameters for drag prediction, an intriguing proposition has been put forth by Shahzad et al. (2022) and Shahzad et al. (2023). They argue that acoustic liners can be considered as porous surfaces. Unlike conventional extrusive roughness described by Chung et al. (2021), flow over porous surfaces exhibits characteristics more akin to canopy-like roughness, as elaborated on by Sharma and García-Mayoral (2020).

Porous surface

Therefore the length scales concerning the roughness (i.e. the pores) need to be classified differently. For this Shahzad et al. (2023) used the viscous scaled facesheet thickness $t^+ = t/\delta_\nu$ and the viscous scaled pore diameter $d^+ = d/\delta_\nu$. These quantities could be considered as the thickness and the pore diameter Reynolds number, just as k^+. For true porous media, the surfaces are characterised by both the Darcy (K_{ij}) and the Forchheimer (α_{ij}) permeability tensors representing the flow passing through the porous surface as have been summarised by Whitaker (1969).

This results in a roughness type which generates pressure drag due to the pores which is intrinsically coupled with the permeability. On this topic, research has been performed by Manes et al. (2009) reporting on pressure fluctuations being the main driver of the turbulent kinetic energy transport into a porous surface. Esteban et al. (2022) finds that through the measurement of substrates with different thicknesses, the effects of the porous wall can be classified as the combination of a rough and a permeable wall. According to Breugem et al. (2006), when there is sufficient separation between the viscous scaled pore diameter (d^+) and the viscous scaled square root of the Darcy permeability tensor ($\sqrt{K_{ij}}^+$), the roughness and the porous effect are separated. These are considered by some authors (G. de Segura and García-Mayoral (2019), Rosti et al. (2018)) as the relevant roughness length scales for porous surfaces.

For the classical porous surface, this is the case in substrates like limestone or a fine sponge. Where the hole diameter is fairly small whilst the porosity is very high. In the case of acoustic liners however, this is generally the other way around, here the 'pores' are large and the porosity is generally below 0.3 (Howerton and Jones (2017) and Schiller et al. (2019)). Moreover, conventional acoustic liner facesheets only show permeability in the wall-normal direction resulting in producing only non-zero $K_{22} = K_y$ and $\alpha_{22} = \alpha_y$. Therefore another relevant scaling parameter to identify aerodynamic performances needs to be considered.

Shahzad et al. (2022) finds that the flow inside the relatively large orifices is dominated by inertial rather than viscous effects. This results in the conclusion that at a high enough pore Reynolds number, the relevant length scale is not the Darcy permeability but the Forchheimer permeability. This is concluded through the consideration of the work of Lee and Yeo (1997); Lee and Ih (2003) and Bae and Kim (2016) who have performed studies to develop the Darcy Forchheimer law. Relating both permeability factors in the wall-normal direction to the pressure drop over the substrate. The equation can be found in (5.1):

$$\frac{\Delta P}{t}\frac{d^2}{\rho\nu U_t} = \frac{d^2}{K_y} + \sigma d\alpha_y Re_p \tag{5.1}$$

here the pressure drop is indicated by ΔP. The thickness and pore diameter are as indicated above. U_t is the superficial velocity (Tanner et al. (2019)) indicating the pore perceived velocity. Finally, σ indicates the porosity as a ratio of the open area with respect to the substrate area.

As can be seen from the equation and Figure 5.1 (a), when the pore Reynolds number is sufficiently high, the Darcy coefficient hardly contributes as it is constant for a specific substrate. The Forchheimer coefficient on the other hand scales with the Reynolds number and therefore at higher Re_p the Darcy coefficient becomes negligible as can be seen from the red shaded area in Figure 5.1 (a). As a result Shahzad et al. (2022, 2023) argues that the (inverse) of the Forchheimer length scale is the relevant scaling parameter. Where $1/\alpha_y^+ = 1/\alpha_y\delta_\nu$ is used as the dimension of the Forchheimer coefficient is $[L^{-1}]$.

This conclusion is based on the study of Shahzad et al. (2023) where a relation between the added drag of the perforated surface and the Forchheimer coefficient is found. It is shown that the inverse of the Forchheimer coefficient is roughly equivalent to the equivalent sand-grain roughness as is illustrated in Figure 5.1 (b). They observe that the roughness function nearly collapses onto the fully rough regime exhibiting Nikuradse-type behaviour for sufficiently high roughness Reynolds number. It is stated that the sand grain roughness can be considered proportional to the inverse of the viscous scaled Forchheimer coefficient as can be seen in (5.2):

$$k_s^+ \propto \frac{1}{\alpha_y^+} \tag{5.2}$$

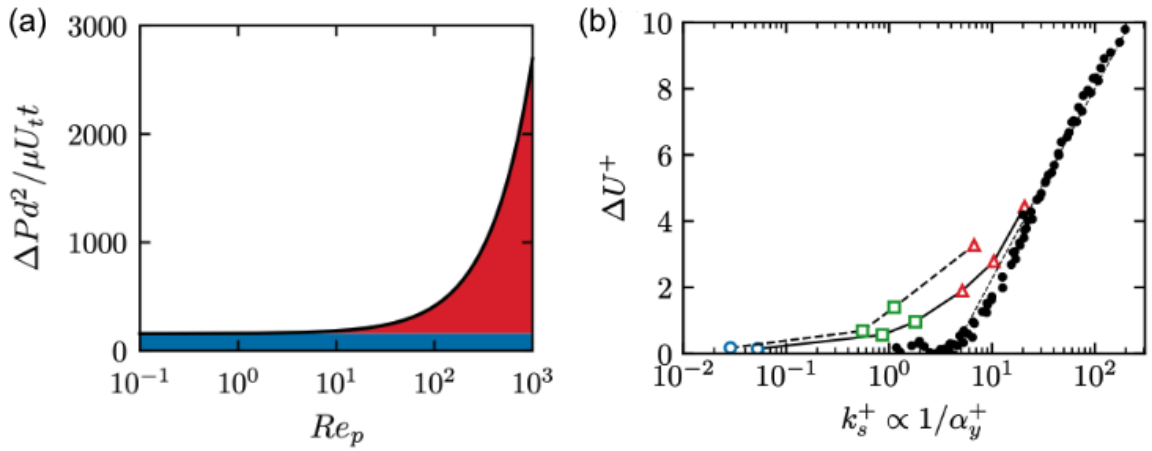

Figure 5.1: (a) Figure representing the Reynolds dependence of the Darcy Forchheimer law for increasing Reynolds number (figure taken from Shahzad et al. (2022)). (b) ΔU^+ with respect to the inverse of the Forchheimer coefficient. (figure taken from Shahzad et al. (2023))

This discussion has resulted in (5.1) being a suitable function to determine the Forchheimer coefficient for the known surface parameters. This in combination with (5.2) and (4.6), is a promising way to predict the velocity deficit of a porous surface, in the fully rough regime. These quantities can be leveraged in the added drag reduction campaign of the thesis.

5.2 Instantaneaous flow

Now that relevant parameters influencing the added drag of the facesheet are identified. There is a desire to couple these to flow phenomena to capture their intrinsic effect on the parameter values and thus the added drag. On the topic of the flow phenomena, governing the added drag over perforated plates, fairly limited research has been done. One of the reasons for this could be that for the qualitative flow either a very precise experiment or a pore-resolved DNS at high pore Reynolds number has to be performed to gain some valuable insights. Due to the limiting factor of computational power, this has not been feasible so far. Wilkinson (1983) established, through experiments of flow over perforated plates, that flow over porous surfaces increases drag. One of the first computational studies performed, regarding the relation of surface roughness and drag, was done by Orlandi et al. (2006). This study concerned velocity

fluctuations caused by cross-flow placed roughness elements. They established that when the root mean square of the wall-normal velocity fluctuations was considered, a satisfactory collapse of data was found for the added drag of the surface.

Jasinski and Corke (2020) have performed an experimental study on the flow over acoustic liners and has found that net zero mass "jet-like" bursts occur from the offices. These jet-like bursts can be quantified as wall-normal velocity, of which was observed that with an increase of the jet-like events, an increase of drag was experienced. Shahzad et al. (2022) has performed pore-resolved DNS simulations on the acoustic liner plates. They have observed that inside the orifice the inertial effects are dominant. This establishes the findings of Jasinski and Corke (2020) as the jet-like flow has been found in the highly inertial orifice regions. Here the conclusion came that ΔU^+ is intrinsically related to the wall-normal velocity fluctuations found in the orifice.

Shahzad et al. (2023) indicates that the virtual origin of the flow is inside the orifice opening, this is approximately 5 viscous scaled wall units into the orifice. Although small it does reveal part of the effect of the liner on drag. This makes it more apparent that the flow impinges on the rear edge of the orifice forcing jet-like structures into the orifice and inducing more pressure drag. The wall-normal velocity fluctuations are reported to increase with the pore Reynolds number.

An illustration of the fluctuations within the cavities beneath the liner can be observed in Figure 5.2. These velocity fluctuations enhance the momentum transfer between the region above and below the liner, thereby contributing to added drag (Orlandi and Leonardi (2006)). As highlighted by Jasinski and Corke (2020), the jet-like flow exhibits net zero mass, indicating that the jet entering the orifice is balanced by an equal outflow from the orifice. This phenomenon supports the momentum transfer between the regions below and above the liner, as discussed by Shahzad et al. (2023).

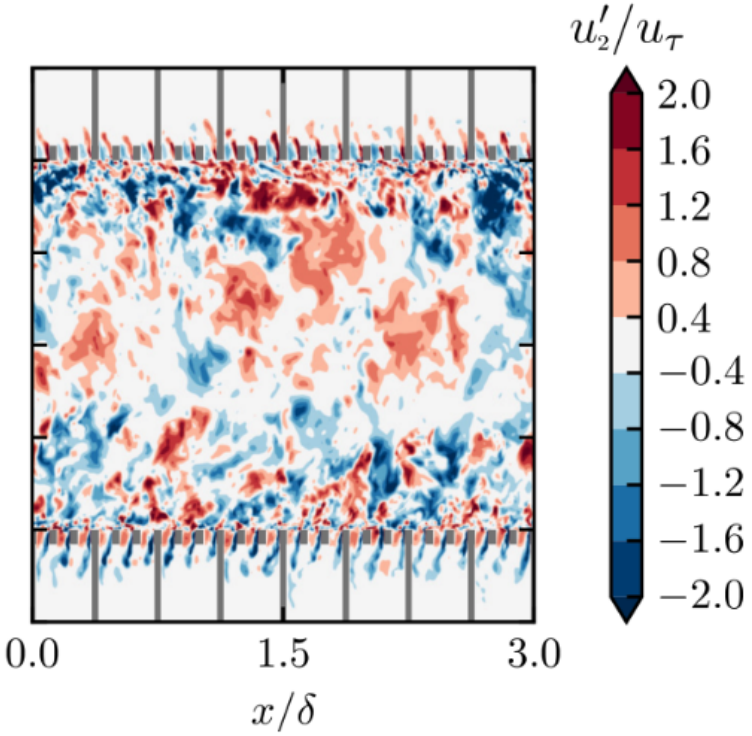

Figure 5.2: Snapshot of the wall-normal velocity fluctuations over a porous surface of POA=32% at $Re_\tau = 2000$. Where the grey lines indicate the facesheet and cavity walls. (from Shahzad et al. (2023))

This evaluation thus leads to the conclusion that the wall-normal velocity fluctuations in the orifice are a large driver for the added drag of the perforated plate geometry, found in acoustic liners. Especially the momentum transfer associated with the wall-normal velocity fluctuations, between the region above and below the facesheet of the liner, is responsible for large velocity deficits.

Since the wall-normal component of the Forchheimer permeability tensor is the only non-zero element, (5.1) focuses on the wall-normal pressure distribution and the pore Reynolds number for the determination of the Forchheimer coefficient. When the pore Reynolds number thus is large enough (i.e.

$Re_p \geq 500$) such that for this higher Reynolds number regime we can write (5.1) as (5.3). This tells us that for constant plate thickness, hole diameter and porosity, the Forchheimer coefficient is governed by the pressure drop over the hole.

$$\frac{\Delta P}{t}\frac{d^2}{\rho \nu U_t} = \sigma d \alpha_y Re_p \tag{5.3}$$

Therefore, the link between the wall-normal velocity fluctuations and the relation of the Forchheimer coefficient with ΔU^+, is that if a larger pressure drop (ΔP) over the hole is experienced, the flow into (or out of) the pore is more restricted. This raises the Forchheimer coefficient, thus decreasing the velocity deficit. A larger difficulty for flow being able to flow into or out of the orifice could additionally result in lower wall-normal velocity fluctuations. Potentially resulting in an added drag reduction, suggesting a link between the wall-normal velocity fluctuations and the Forchheimer coefficient. What application this notion can find in its implementation of the acoustic liner will be discussed in the subsequent section.

Mechanisms to reduce Added drag

Having identified the main drivers for the added drag of a perforated surface, the discussion can turn to some mechanisms which are known to reduce the aforementioned mechanisms providing possible solutions to discover in the thesis. One solution provided for the reduction of drag over the flat plate configuration is seen for (micro) orifice blowing O'Connor et al. (2023), Kornilov and Boiko (2012), who find a 70% drag reduction over the smooth wall configuration. Although these results are promising, they do require blowing into the orifices which could potentially hamper the sound attenuation properties. Moreover, this is an active process requiring energy to work. This ensures a more complicated system than a passive system for which no energy needs to be spent for it to function.

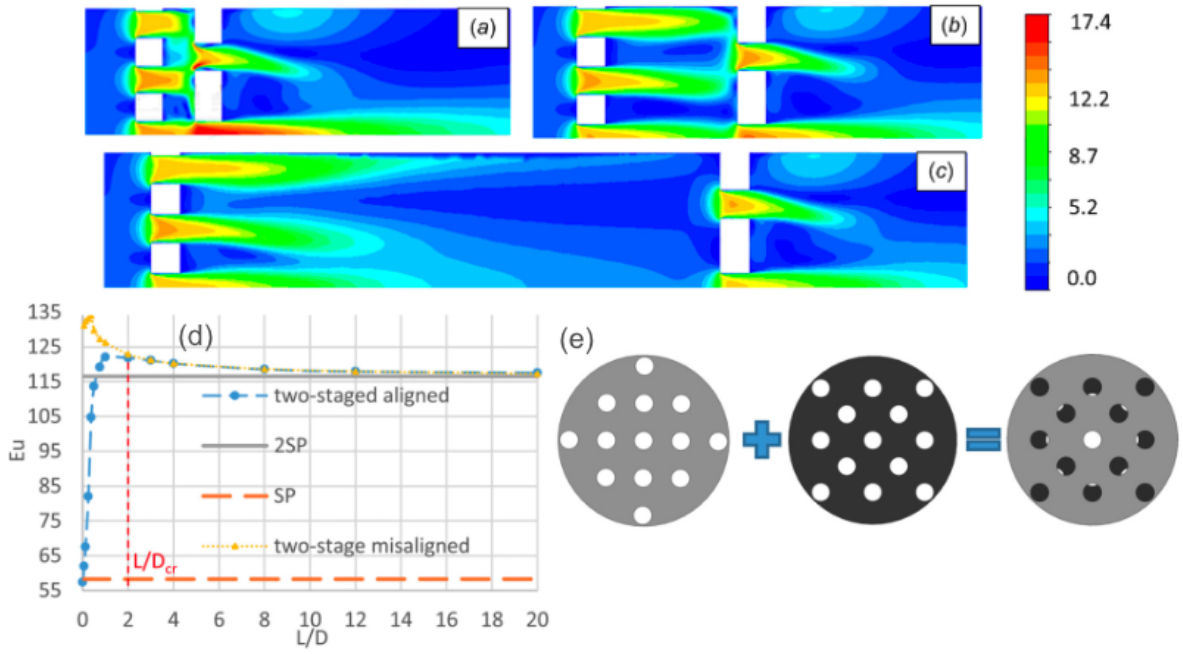

Figure 5.3: (a-c): Velocity field of misaligned perforated plates at various distanced L/D of 1/8, 1/2 and 2 respectively. (d) Pressure loss coefficient EU as a function of L/D for misaligned perforated plates (yellow). (e) Geometry of the separate perforated plates and the combination of the two plates in the misalligned configuration. The white space shows the opening in the plate. (All images taken from La Rosa et al. (2021).)

Different geometries, like surfaces with riblets are known to reduce surface drag (Modesti et al. (2021)) as the span-wise flow variations are inhibited. These can be employed to reduce the overall plate drag. The application of orifices to such geometries is however likely to influence the aerodynamic properties, as Manes et al. (2009) found by comparing the flow over permeable and impermeable rough wal surfaces.

Although these mechanisms are known to reduce the drag of a smooth plate, there is no guarantee that these will perform the same when the sound absorption constraint has to be adhered to. When (5.3) is considered, one of the solutions for the reduction of drag could be to increase the pressure drop over the perforated plate rather than reduce the friction of the flow along the plate.

Conveniently, La Rosa et al. (2021) conducted a study on the pressure drop across multiple perforated plates, examining the influence of hole alignment on this pressure drop. The research investigated a misaligned configuration (Figure 5.3 (e)) where closely spaced perforated plates resulted in a greater pressure drop compared to the sum of the pressure drops across two separate plates, as illustrated in Figure 5.3. The spacing parameter, denoted by the length L normalized by the pipe diameter D, is equal to 9.27 times the hole diameter d. Figures (a) to (c) in Figure 5.3 depict how the flow is constrained when the plates are in close proximity. Figure (d) illustrates the pressure loss coefficient for the aligned, misaligned, and separate plate configurations. It is evident from (d) that the flow experiences significant constraints when the plates are closely spaced. Notably, for L/D values very close to 0, the pressure loss coefficient decreases. This occurs because the middle hole of the plates is always aligned, and there is some degree of overlap among the remaining holes, effectively reducing the porosity of the configuration at $L/D = 0$.

6

Problem statement

The thesis aims to seek solutions to reduce added liner drag while maintaining the acoustic properties of a liner. As has been indicated in Chapter 2, many novel liner designs are being proposed. One of these designs consists of the application of three facesheets in a staggered configuration proposed by Dodge et al. (2023). Here the authors provide evidence indicating limited to no loss in acoustic performance when employing multiple staggered facesheets with sufficient spacing between them. From an acoustics perspective, this is a promising result however this has many applications in the quest for a more favourable facesheet configuration from an aerodynamic perspective. The aerodynamic properties of this configuration however are not explored by the author. Therefore this thesis will aim to attain more insights into the aerodynamic performance of the multiple facesheet configuration like that of Dodge et al. (2023).

Moreover, the interest in the aerodynamic properties stems from the concept of the Forchheimer coefficient being an appropriate scaling parameter for the velocity deficit of perforated plates, proposed by Shahzad et al. (2022) and the larger pressure differential over staggered plates found by La Rosa et al. (2021). The equations containing the Forchheimer coefficient (5.3) show that the pressure differential (ΔP) over the facesheet can be increased to reduce ΔU^+. The connection, therefore, between the multiple facesheets and the potential reduction of drag finds its origin in the work done by La Rosa et al. (2021). Specifically, the staggering of plates ensures a greater pressure drop over the two plates for normal flow through them. At the optimal spacing of staggered plates, the maximum pressure drop is 15% larger than that of two separate plates combined (Figure 5.3 (d)).

Based on the studies mentioned above, it is pertinent to explore the potential impact of multiple facesheets on the aerodynamic properties of acoustic liners. Considering the findings, configurations with multiple facesheets, particularly when placed in a staggered arrangement, are expected to amplify the pressure drop across the entire facesheet. Additionally, this configuration may effectively suppress wall-normal velocity fluctuations, which are known to contribute to drag over rough surfaces. To assess the combined effect of these factors, the following research questions are defined for this thesis:

Research Question

Research Question: What is the effect of an additional facesheet on the aerodynamic performance of acoustic liners?

Sub-questions:

1. What is the effect of an additional facesheet on the added liner drag?
2. How does a double facesheet affect the wall-normal velocity fluctuations and interaction between the flow below and above the facesheet?
3. What are the relevant scaling parameters for the performance indication of the dual facesheet liners?

7

Methodology

In the drag identification studies of acoustic liners, the methodology is either experimental or numerical. Where the experimental studies, mainly use a grazing flow tunnel with different drag identification techniques. An example of this is a direct drag balance (Zheng et al. (2022a, 2022b)), which is based on measuring the effect of the drag of the facesheet directly with the force balance. Alternatively Scarano et al. (2022); Gowree et al. (2019) use a detailed hot-wire probe to compare velocity profiles of smooth and perforated configurations. This gives the added drag results through the roughness function. Gustavsson et al. (2019); Howerton and Jones (2015) on the other hand measure the pressure drop over the substrate in order to derive a friction coefficient which can be compared to smooth wall configurations to obtain added drag results.

Although experimental studies give accurate and reproducible results, due to the measurement technique there is mainly one, or a limited series of quantities which can be extracted. For more insights into multiple variables and a more qualitative flow field, there is a need for more information. This can be provided by the use of Direct Numerical Simulations (DNS). This is the method of choice for Shahzad et al. (2022); Zhang and Bodony (2016) who argue that pore-resolved, compressible, DNS simulations are required for accurate drag determination of the novel porous surfaces. As Shahzad et al. (2022) reported, both the flow origin and many wall-normal velocity fluctuations have been found inside the orifice. The high resolution in the pores of the facesheet is therefore necessary for the desired results. This resolution will allow the interaction of the flow inside the orifice with that above and below to be examined closely. When the flow phenomena in the orifice are of interest, however, a porous boundary condition model can not be used.

This chapter will therefore first focus on the DNS solver used throughout the thesis. Both the governing equations as well as the validation of the solver will be discussed. Secondly, the qualitative flow phenomena in the orifices are of interest. Therefore, a porous boundary model, emulating the effect of a porous boundary on the flow without explicitly modelling the geometry, is not sufficient. The porous geometry needs to be explicitly included in the computational domain. This is done through the use of the immersed boundary method, which will be explained and validated in the following section. When both the solver and the boundary method are established and verified, the chapter will focus on the actual simulations performed on various, double facesheet, geometries. Finally, the methodology to attain the Forchheimer coefficients for the proposed cases' geometries will be discussed such that these geometries can be placed in the context of Shahzad et al. (2023).

7.1 STREAmS

The investigation into the novel facesheet configuration liners has been done by the use of the compressible DNS solver, STREAmS. An in-house designed solver by Bernardini et al. (2021), leveraging Message Passing Interface (MPI) parallelization on High-Performance Computing (HPC) clusters and recent developments of computations on GPU to attain a very efficient DNS solver. The numerical simulations solve the system of equations shown in (3.3), (3.4) and (3.5). The accompanying section (section 3.1) elaborates on the equations and definitions given in the Navier-Stokes equations.

The flow statistics are gathered through averages of the flow. For the viscous scaled velocity, a Favre averaging (Favre (1969)) is used, which is common for compressible flow. The Favre ensemble average

is a density-weighted average which takes the Reynolds averaged flow and accounts for the fluctuations in the density of the flow. Any arbitrary, time-dependent variable Φ, can be decomposed into the Favre averaged mean ($\widetilde{\Phi}$) and the fluctuating part (Φ'') as can be seen in (7.1). Where ($\widetilde{\Phi}$) is found in (7.2), where T is the total time of the statistical sample and $\langle\cdot\rangle$ is used to indicate the Reynolds ensemble average. In channel flow, the Reynolds average of the flow is taken of the time-averaged flow in the x and z direction, providing $\langle u\rangle(y)$.

$$\Phi = \widetilde{\Phi} + \Phi'' \tag{7.1}$$

$$\widetilde{\Phi} = \frac{\int_T \rho(t)\Phi(t)dt}{\int_T \rho(t)dt} = \frac{\langle\rho\Phi\rangle}{\langle\rho\rangle} \tag{7.2}$$

The Navier-Stokes equations are solved through the use of an energy-preserving scheme in locally conservative form, devised by Pirozzoli (2010). This scheme is used for the discretisation of the convective terms of the Navier-Stokes equations. Which has a user-defined order of accuracy ranging from 2 to 8, in the current work the order of accuracy is set to 6.

From the spatial discretization, as has been described above, (7.3) remains. Which contains the temporal derivative of the conservative variables vector, $\mathbf{w} = [\rho, \rho u, \rho v, \rho w, \rho E]$ and the vector of the residual $\mathbf{R}$. This system of equations progresses in time through a three-stage, third-order Runge-Kutta scheme as has been described by Spalart et al. (1991).

$$\frac{d\mathbf{w}}{dt} = \mathbf{R}(\mathbf{w}) \tag{7.3}$$

7.1.1 STREAmS validation

In order to justify the conclusions from the results gathered from the STREAmS DNS, a validation of the smooth, sub-sonic (with bulk Mach number defined as $Ma_b = u_b/c_b = 0.2$), channel flow is performed. This is done by comparing DNS results of the channel flow simulations performed by Lee and Moser (2015) to the results produced by STREAmS for the same domain, friction Reynolds number and mesh spacing. The validation test is performed on two flow cases, $Re_\tau = 180$ and $Re_\tau = 550$.

For this study, the smooth-wall, channel domain size and flow conditions as used by Lee and Moser (2015) have been reproduced. The dimensions of the domain, mesh element size and flow conditions can be found in Table 7.1. As can be seen, all parameters correspond fairly well. The largest difference is in the mesh element size Δy_w^+, as the wall spacing in the validation study is coarser to reduce computational costs. Next to the wall spacing, there is a slight difference in the friction Reynolds number for the Re_τ=550, this is a consequence of the mass flow forcing in the solver which can potentially result in small Re_τ discrepancies in friction Reynolds number. As this is a consequence of the flow and not an apriori set parameter in the solver.

Runs	Re_τ	Re_b	$\frac{L_x}{\delta}$	$\frac{L_z}{\delta}$	Δx^+	Δz^+	Δy_w^+	Δy_c^+	N_y	$Tu\tau/\delta$
LM180	182	2857	8π	3π	4.5	3.1	0.0074	3.4	192	31.9
LM550	544	10000	8π	3π	8.9	5.0	0.0019	4.5	384	13.6
VS180	182	2858	8π	3π	5.9	4.4	1.06	6.3	96	43.8
VS550	563	10449	8π	3π	9.8	5.1	0.84	6.1	384	12.1

Table 7.1: Comparison of the reference case runs and the validation. LM indicates the reference case (Lee and Moser (2015)) and VS indicates the **V**alidation run of **S**TREAmS. The number behind this distinction is the indication of the friction Reynolds number Re_τ. Re_b is the bulk Reynolds number, L_x and L_z the domain size normalised by the half channel width δ. Δx^+ and Δz^+ is the size of the mesh elements in x and z direction respectively. Δy_w^+ is the mesh spacing at the wall and Δy_c^+ at the channel centre-line. N_y is the number of mesh elements in the y-direction and $Tu\tau/\delta$ is the simulation time taken to gather statistics (Eddy Turnover Time).

The comparison of the mean velocity profiles for both flow cases can be seen in Figure 7.1 (a,b). The left figure, (a), shows the results for the mean wall scaled velocity $\langle u^+ \rangle$ for the $Re_\tau = 180$ case. The right image, (b), shows the mean wall scaled velocity $\langle u^+ \rangle$ for the $Re_\tau = 550$ case. Additionally, Figure 7.1 (c,d) show the Reynolds stresses of the respective simulations ($Re_\tau = 180$ and $Re_\tau = 550$). The Reynolds stresses shown are; $\langle u_1' u_1' \rangle^+$ $\langle u_2' u_2' \rangle^+$, $\langle u_3' u_3' \rangle^+$ and $\langle u_1' u_2' \rangle^+$ in descending order. The remaining elements ($\langle u_1' u_3' \rangle^+$ and $\langle u_2' u_3' \rangle^+$) are omitted as these are statistically zero in a channel flow.

Overall, good correspondence between the VS and LM runs are found. Some small differences, like in the $\langle u'u' \rangle$ of LM550 and VS550 can be attributed to the small difference in friction Reynolds number (Re_τ in Table 7.1). The results of the comparison establish that the STREAmS solver provides accurate and reproducible results.

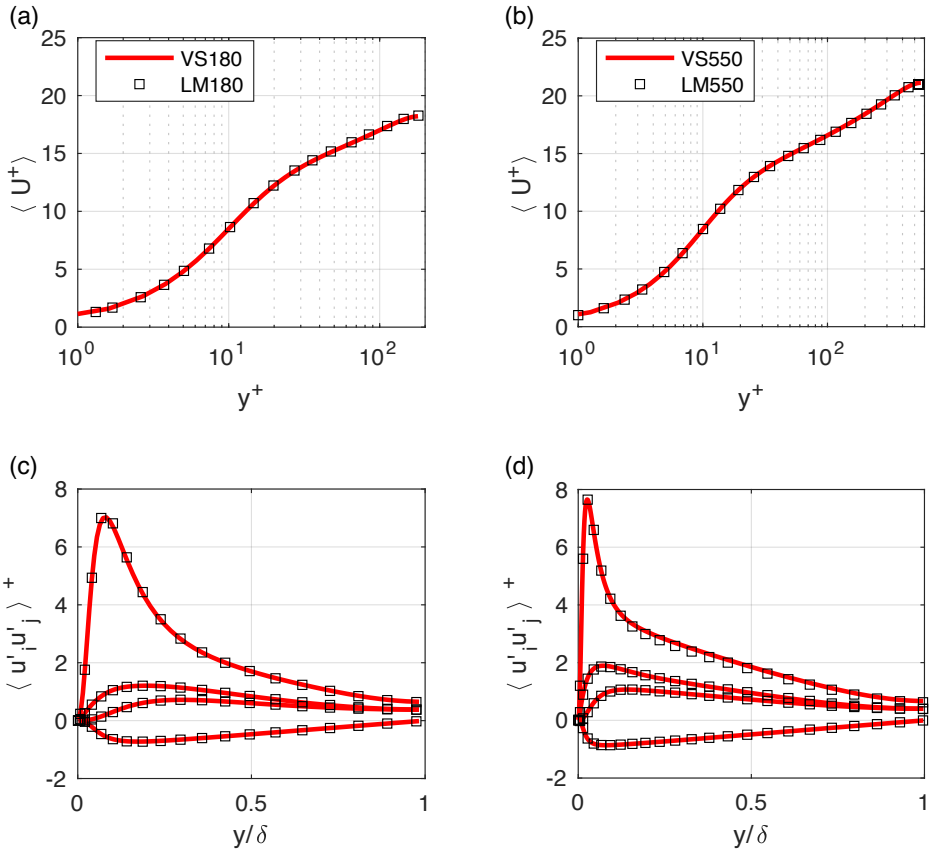

Figure 7.1: (a,b) Comparison of mean velocity profile $\langle u^+ \rangle$ (w.r.t wall distance) from STREAmS (red line) and Lee and Moser (2015) (black squares) results. (c,d) Comparison of the Reynolds stresses $\langle u_i' u_j' \rangle^+$ from STREAmS (red line) and Lee and Moser (2015) (black squares)results.

Drag metrics

Acoustic liner drag identification studies do not only contain the simulation of the flow field subject to a certain channel wall geometry. They also entail the post-processing of the results from the flow field data to useful quantities used by other authors such that results can be compared.

One of the most general indications of the added drag is ΔU^+ as has been readily discussed in previous chapters. The quantity gives a relative velocity deficit with respect to a smooth wall. ΔU^+ is found through the mean velocity profile of the half-channel flow. This value is therefore derived from a large amount of data, as the channel flow is fully turbulent, and many fluctuations are found in the flow. The averaging of the statistics in this work is at least 10 eddy turnovers (Tu_τ/δ) as has been deemed sufficient by Shahzad et al. (2022). This is to ensure that the averages do not change any more over time and represent true averages of the flow. From this, a part of ΔU^+ can be found, as it would be either the smooth or the rough wall geometries' velocity profile.

The quantity needs a reference smooth-wall case in order to be obtained. So the results of a smooth-wall

and a subject geometry are needed to find these results. According to Modesti et al. (2021), ΔU^+ can be used to find the drag variation as can be seen in (7.4):

$$(\%) = 1 - \frac{C_f}{C_{fsw}} = 1 - \frac{1}{(1 - \frac{\Delta U^+}{U^+_{\delta sm}})^2} \tag{7.4}$$

Where C_{fsw} is the skin friction of a smooth wall and $U^+_{\delta sm}$ is the centre line velocity of a smooth-wall channel. This function can give a percentage value for the drag reduction as a final product.

Alternatively, the skin friction coefficient can be used (3.16) to describe the drag influence. This is non-dimensionalised and therefore can be compared well to other studies. In order to attain the skin friction coefficient, τ_w must be obtained which is related to the pressure gradient. These equal each other (3.10), and the mean pressure gradient is used to drive the flow in the periodic channel. This is to ensure that the flow through the domain maintains a constant mass flow rate. As τ_w is larger, there is a larger pressure gradient needed to maintain the same mass flow rate.

The results of the pore-resolved DNS simulations will be averaged to find the ΔU^+ of the geometry with respect to a reference value. This result combined with the friction coefficient and the drag variation will lead to appropriate measures to evaluate the drag performance of novel liner designs. Additionally, the wall-normal velocity fluctuations will be expressed by both the instantaneous flow fields as well as the corresponding Reynolds stresses as found in (3.14).

7.2 Immersed Boundary Method

The boundary of the smooth-wall channel flow has a no-slip boundary condition imposed. This is done for a flat, smooth, isothermal, wall where a non-permeability condition is applied, such that no wall normal flow is allowed through the boundary. The boundary for the porous geometries will be modelled by the Immersed Boundary Method (IBM).

The Immersed Boundary Method eliminates the requirement to explicitly mesh each roughness element. As explained by Mittal and Iaccarino (2005), it imposes a geometry on the flow with opposite value source terms inside the geometry. This is often referred to as the discrete forcing approach deemed most suitable for stationary and rigid boundaries. The source term forcing is applied after the discretisation of the flow equations in the solver. An example of the IBM can be seen in Figure 7.2 where the Cartesian mesh is overlaid over the geometry and the forcing at the ghost nodes inside the body and the fluid

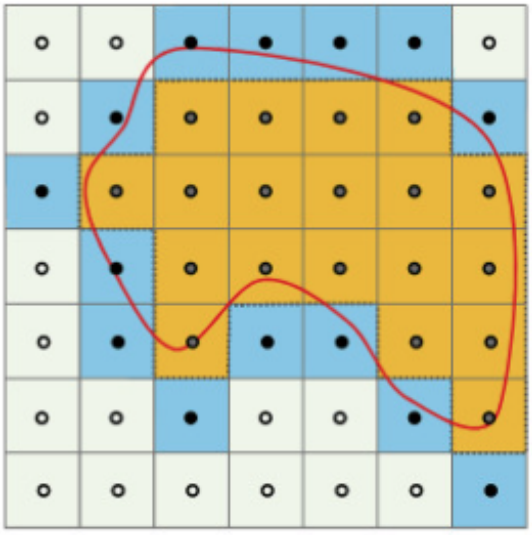

Figure 7.2: Example of the Immersed Boundary Method (IBM). Here the white cells, with the open node points, represent the fluid nodes, the blue cells with black nodes the forcing points and the yellow with grey nodes are the solid cells and nodes respectively. The red line represents an arbitrary geometry onto which the IBM adapts itself. (from Liu and Hu (2019))

points outside the body ensure the boundary is adhered to. For a solid boundary, the IBM ensures zero velocity at the boundary. Do note that the image is in 2D while the IBM in most geometries works in 3D extending into an additional dimension. For detailed explanations of the forcing terms Mittal and Iaccarino (2005) is recommended.

Due to the development of IBM, very cumbersome, explicit meshing of conformal grids around irregular roughness topographies is not necessary. This makes numerical simulations a more feasible approach for the added drag studies of the rough-wall topographies. Especially when different topographies are under scrutiny, as is the case in this work, the IMB is the preferred boundary method. In order to ensure the accuracy of the results provided by the IBM boundary, the following section, focussing on the validation of the IBM used in STREAmS, is employed.

7.2.1 IBM validation

In order to justify the results gathered with the help of the IBM, the boundary method will first be validated. This is done through the use of DNS results found by MacDonald et al. (2018) for 2 dimensional, rectangular spanwise bars in the domain. The computational domain consists of a 'minimal-span rough wall channel' which is the half channel with a slip, symmetry condition placed on the centreline which cuts the domain in half. The boundary of the explicitly meshed roughness elements is the conventional no-slip boundary and all remaining sides of the domain have periodic boundary conditions. Chung et al. (2015) have established this to be a computationally cost-efficient way to characterise hydraulic roughness elements in a channel flow. Especially as the span of the domain can be limited since the near wall (below $y_c \approx 0.4L_z$) turbulence is not altered. Therefore the results from MacDonald et al. (2018) have been selected as a validation source as they provide a cost-efficient way to validate the workings of the IBM in STREAmS.

The rectangular spanwise bars span over the entire width of the domain with various spacings and depths of the throughs. For the validation, the configuration with depth and width of the elements of $k^+ = 50$ and $W^+ = 100$ has been selected. A schematic overview of this geometry is provided in Figure 7.3. The origin of the smooth wall is found on top of the roughness crests and the throughs protrude downwards. This emulates, to a certain extent, a perforated surface, making it an even more relevant validation study.

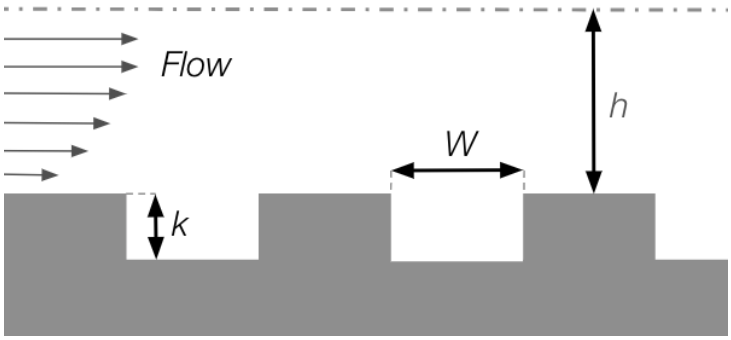

Figure 7.3: Sketch of the geometry from MacDonald et al. (2018) used for the validation of the IBM. The image has the flow direction indicated, the width W and the height k of the roughness elements are shown. The height of the half channel is indicated with h where the dashed line indicates the position of the symmetry boundary.

The $k^+ = 50$ and $W^+ = 100$ geometry is reproduced with 5 crest and roughness pairs placed in alternating order in the streamwise direction. The grid used is equally spaced in the x and z direction while the spacing in the y direction has a tanh regression with $N_x \times N_y \times N_z = 800 \times 250 \times 68$ (where the present notation conforms to that of this thesis, s.t. y is the wall-normal coordinate, not z as in MacDonald et al. (2018)). All simulations are performed at the same friction Reynolds number of $Re_\tau = 395$.

The results of the DNS run using IBM for the roughness geometry and those of the body-fitted mesh with conventional no-slip boundary condition are displayed in Figure 7.4. As can be seen from 7.4 (a), the mean velocity profile corresponds very well, both close to the wall and further towards the centreline, to the reference case. Especially the velocity profile close to the wall (i.e. $y^+ < 50$) is of interest as this is impacted the most by the boundary condition. The same effect is seen from the Reynolds stresses in 7.4 (b), where all the non-zero components of the Reynolds stresses are shown. Here again, both the results

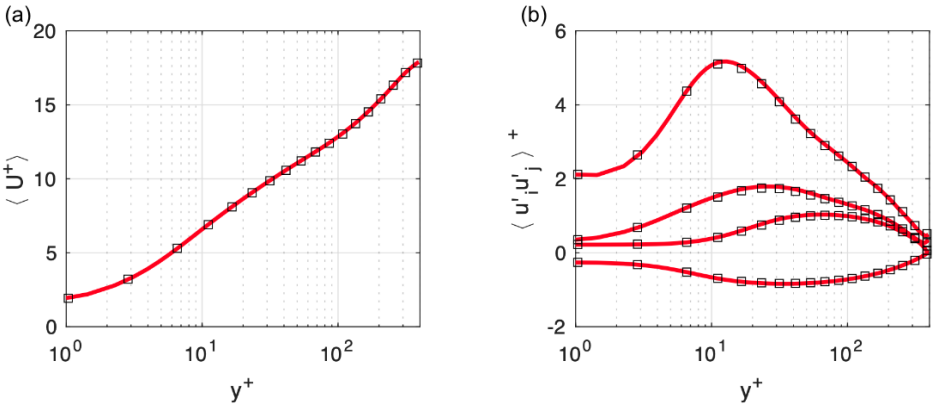

Figure 7.4: (a): Comparison of the mean velocity profiles found by the IBM tested in STREAmS (red line) and the limited span half channel runs performed by MacDonald et al. (2018) (black squares) . (b): Comparison of the Reynolds stresses found by the IBM tested in STREAmS (red line) and the results from MacDonald et al. (2018). Here the highest values are attained by $\langle u'_1 u'_1 \rangle$, then the second largest by $\langle u'_2 u'_2 \rangle$, the third by $\langle u'_3 u'_3 \rangle$ and the lowest and partially negative Reynolds stresses by $\langle u'_1 u'_2 \rangle$

close to the bottom boundary and towards the centreline correspond well to the reference case. The validation can therefore conclude that the IBM can very well be used to mesh the roughness geometries. This validation has shown that the IBM handles the porous wall-like geometries as well as a body-fitted mesh configuration.

7.3 Double facesheet

In order to produce a sensible double liner design, next to the facesheet geometry, which will emulate that of Shahzad et al. (2023), the size of the gap between the two plates needs to be determined. Where the pressure drop over the two facesheets increases with smaller spacing between them. In the case of La Rosa et al. (2021), the staggered configuration does have a central hole which is fully aligned as shown in Figure 5.3 (e). This limits the pressure drop over the plates when the spacing approaches 0, as the two plates effectively become one thicker plate with a limited porosity. Where, according to Gan and Riffat (1997), a thicker plate with sharp-edged orifices shows a lower pressure drop for a t=d facesheet than one where t=0.5d and increases further for thinner plates. This effect can cause less desirable results when the spacing is too small and some alignment of the holes is experienced.

Therefore, these studies show that when the spacing between plates reduces, the pressure drop increases. Looking at (5.3), the increase in ΔP results in the rise of α_y and therefore reduces ΔU^+. However, there is also a need to maintain a certain distance between the plates to preserve the noise-reduction properties of the liner. When the holes are fully miss-aligned and the spacing gap is 0, the pressure drop increases exponentially but there is no attenuation of any incident sound (Cherrier et al. (2012)). To provide some context in facesheet spacing, the geometries and gaps used in previous studies have been summarized in Table 7.2. Based on this information a gap spacing will be selected that is used for the geometries that will be tested.

When we compare the spacing between the facesheet plates, based on the hole diameter, as shown in the table, the largest spacing (G3) used by Dodge et al. (2023) is 0.342d. This is a relatively small spacing between plates which already allows for good sound attenuation levels. La Rosa et al. (2021) shows that for staggered geometries, the pressure drop over the plates with a spacing of $\frac{L}{D} < 1$, where D is the pipe diameter (D = 9.27d), is lowered. The combination of these feats shows that the spacing (between plates) used in the La Rosa paper is much larger than that in the Doge paper. This establishes that all the cases in the La Rosa paper would have sufficient sound attenuation properties, as these grow with the increase of the spacing.

Therefore, the spacing used for the G3 configuration of Dodge et al. (2023) can be treated as a constraint for the minimum spacing between the facesheets to maintain the desired sound attenuation properties. Depending on the amount of staggering of the facesheets, the appropriate spacing could lead to a larger and more desirable pressure drop over the facesheet. To assess these effects, the limited size channel flow

	Case	d	$\frac{g}{d}$	$\frac{t}{d}$	σ	σ_{eff}
Shahzad et al. (2023)	$L-L14$	0.08δ	-	1	0.142	0.142
	L_t-L14	0.08δ	-	0.5	0.142	0.142
Dodge et al. (2023)	G3 (100%)	0.046"	0.342	0.435	0.1087	0.1087
	G3 (25%)	0.046"	0.342	0.435	0.1087	0.0272
La Rosa et al. (2021)	Non-staggered	8.4 mm	9.27	1	0.15	0.15
	Staggered	8.4 mm	3.48	1	0.15	0.0116

Table 7.2: Geometry overview and comparison of the different cases of interest. The DNS geometry from Shahzad et al. (2023) for the perforated single facesheet where the first L refers to Liner configuration, the second to $Re_\tau = 500$, 14 the POA and the 't' subscript indicates the thin facesheet. The orifice diameter d is expressed as a function of half channel width $\delta = 1$ (in the first case). The facesheet porosity σ and the effective porosity σ_{eff} are shown for all cases. The effective porosity is the area of the holes which can be looked through when the facesheets are staggered. Additionally, the largest facesheet gap configuration 'G3', of the experimental set-up, of Dodge et al. (2023) is shown, for different opening percentages (i.e. 100% and 25%). The orifice diameter d is expressed in inches and the facesheet spacing gap g is expressed in the orifice diameter. The same is done for the CFD set-up from La Rosa et al. (2021) for both the staggered and non-staggered cases. The spacing g however for this case indicates the spacing at which the pressure drop over the two plates is maximum and the orifice diameter is expressed in millimetres.

geometry, used by Shahzad et al. (2023), is replicated for this study and the results for the 14.2% POA run will be used as reference. These reference cases are included in Table 7.2 to show the relative sizes of the orifices, plate porosity and thickness.

In order to be able to connect the results to the acoustic properties of Dodge et al. (2023), the same relative thickness of the facesheet and the largest gap configuration are used (based on orifice diameter). The diameter of the orifice used, however, is taken from Shahzad et al. (2023) just as the domain size for the channel. This way the geometry has the same dimensions and ensures that the flow results for the smooth wall configuration and the results for the liner can be used as reference cases to such that the effect of an additional facesheet can be observed. The additional benefit of this is that when the geometrical ratios are maintained between the orifice and the cavity volume the sound attenuation properties are the same as those of Shahzad et al. (2023).

The triple facesheet geometry of Dodge et al. (2023) is used as a reference for the percentage open configurations. The present work, however, will use 2 facesheets as opposed to 3 to reduce computational costs and geometric complexities. This simplification is mainly based on the mesh spacing of the computational domain, spanning the facesheet gap. This needs to be $\Delta y^+ < 1$ in order to capture all small-scale fluctuations in these areas. According to La Rosa et al. (2021) however, the use of only two staggered plates is sufficient to attain the desired pressure differential and therefore is deemed sufficient to evaluate the effect of multiple facesheets.

7.3.1 Geometry

The geometry of the double facesheet liner is constructed by combining the first and second facesheets (fs_1 and fs_2) as illustrated in Figure 7.5 (a). Both fs_1 and fs_2 possess a single plate porosity of $\sigma = 0.142$, and the effective porosity resulting from their combination (at 50% open) is $\sigma_{eff} = 0.071$, i.e. 50% of σ. The overlapping area of the orifices, seen through the top and bottom facesheet is the effective porosity σ_{eff} (based on the total cavity area). This is visualised by the light which passes through both perforated facesheets (white space in combined image). The double facesheet is presented through an x-plane slice at the midpoint of the orifice in both (b) and (c). The orientation of the rectangular cavities, each with a size of 0.335δ per side (excluding the 0.04δ thick walls), is displayed. The channel liner comprises a total of 64 cavities, resulting in 64 configurations similar to the right image in Figure 7.5 (a). The facesheets are spaced as depicted in (c), the current image shows the orifice orientation of the 50% open area orientation which is shifted upstream with a specific staggering distance d_{stag}. This distance is increased or decreased depending on the lower or higher (resp.) percentage open area of the configuration. To isolate the effect of the double facesheet, only the second facesheet (i.e. fs_2) is shifted

along the streamwise direction.

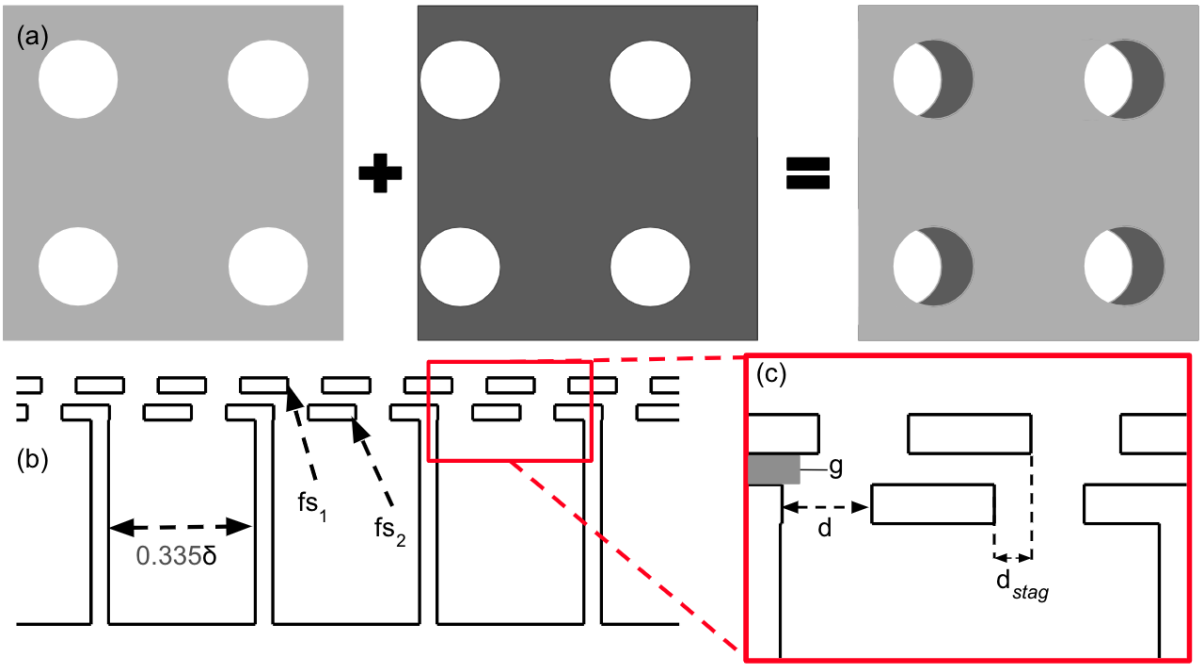

Figure 7.5: (a): Orientation of the holes through both facesheets covering one cavity for the 50% open ($D_{50} - L14$) configuration. The light grey facesheet represents facesheet 1 (fs_1) and the darker grey facesheet represents facesheet 2 (fs_2). Combined they show the top view for the configuration where the white space indicates the passage through both plates. (b): Schematic cut-through of the domain in the x-plane showing both facesheets and the cavity below. The slice is through the middle of the orifices of the 50% open configuration. In the image, both fs_1 and fs_2 are indicated and the size of the cavity is indicated. (c): Zoomed in schematic image of (b) where the gap, the diameter and the staggering distance are pointed out having size $g = 0.342d$, $d = 0.08\delta$ and $d_{stag} = 0.0323\delta$ respectively. The staggering distance changes depending on the percentage open area of the configuration.

As mentioned above, the channel flow geometry of this study has the same dimensions as Shahzad et al. (2023) has used. This ensures the ability to use the results for the smooth wall channel flow and the results of the Liner geometry $\sigma = 0.142$ (first three cases of Table 7.3) as reference cases. This, in turn, allows for the computation of ΔU^+ and asses relative performance, without the need to run these configurations again. The limited size channel dimensions are $L_x \times L_y \times L_z = 3\delta \times 2(\delta + h) \times 1.5\delta$ where δ is the channel half width and h is the depth of the cavity plus the total facesheet thickness (including gap spacing). The set-up of the total geometry can be seen in Figure 7.6 (a). Here the cavities below the facesheet and the double facesheet in the channel flow are displayed. The orifices of the facesheet are placed in the same locations and have the same dimensions as those of Shahzad et al. (2023) creating an identical geometry at the channel walls. For a reference friction Reynolds number of 500, the viscous scaled diameter of the orifices is $d^+ = 40$. Figure 7.6 (b-g) show the different orifice orientations tested for the runs as indicated in Table 7.3.

The computational domain spacing, in the x and z direction, is based on the minimum number of mesh elements per cavity (found through the mesh sensitivity study performed by Shahzad et al. (2023)). These have at least 25 elements spanning across the diameter of the orifice. This results in an equally spaced mesh in both the x and z direction of equivalent size. The domain length is $L_x = 3\delta$ and $L_z = 1.5\delta$ and therefore the mesh contains 1000 and 500 mesh elements respectively to adhere to 25 elements over the 0.08δ diameter of the orifices. The spacing of the mesh in the wall-normal direction (y) is based on attaining a sufficiently small spacing at the wall and in the facesheet gap of $\Delta y^+ \approx 0.8$. To attain this, the mesh from the centre of the channel to the wall decreases in spacing following $tanh$ from $\Delta y_c^+ \approx 5.8$ to $y_w^+ \approx 0.8$, depending on the friction Reynolds number of the specific simulation. The wall-normal spacing in the gap between the facesheets and through the orifices of both facesheets is maintained at y_w^+ before coarsening in the cavity again. This is done such that all the velocity fluctuations in, and close to, the orifices are captured. As these have been identified as the main contributors to the facesheet drag of

the channel.

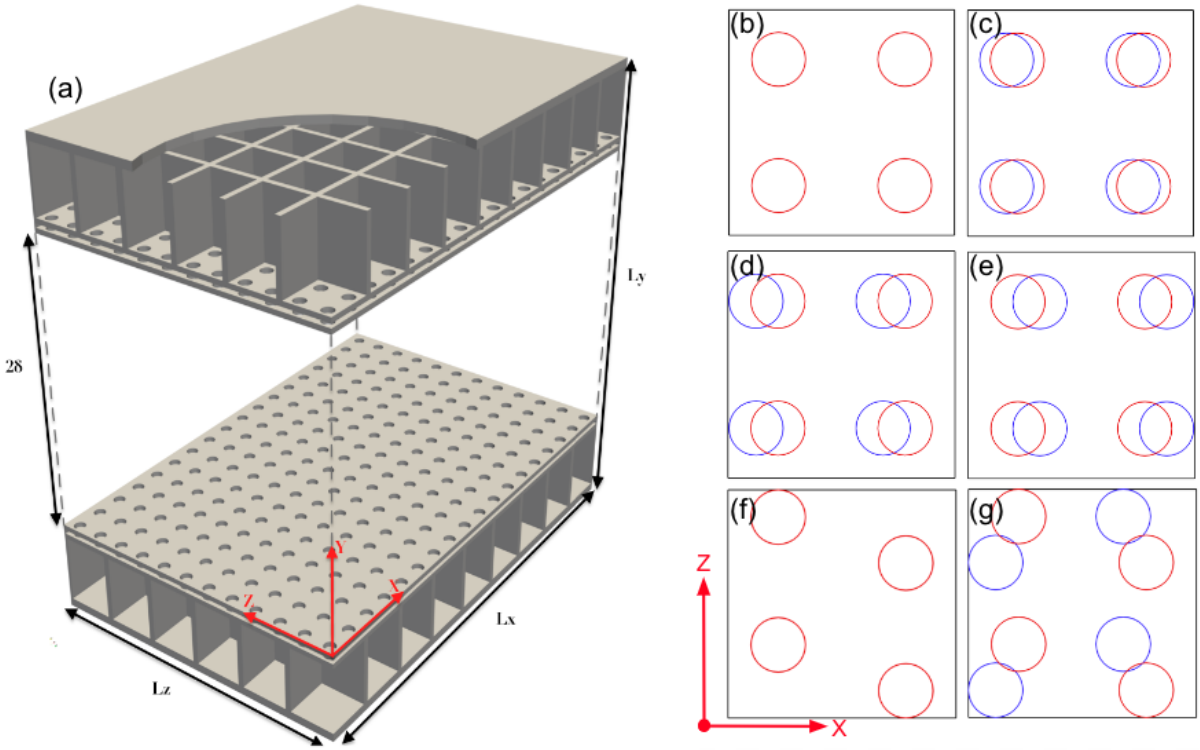

Figure 7.6: (a): Schematic image of the double facesheet liner, channel geometry in the $D_{100} - L14$ configuration. The geometry shows the square cavities with their corresponding 4 orifices per cavity. The domain has $L_x \times L_y \times L_z = 3\delta \times 2\delta \times 1.5\delta$ as its dimensions, with the thickness of both facesheets is $t_{fs1} = t_{fs2} = 0.435d$ and the spacing gap between the plates is $g = 0.342d$ as indicated in Table 7.2. (b): 100% open facesheet orientation ($D_{100} - L14$) of the top with respect to the bottom facesheet (i.e. fs_1 and fs_2 resp.) and the inner cavity walls (Black square). NOTE: both the liner reference cases (i.e. $L - L14$ and $L_t - L14$) have the same orifice and cavity orientation but with a single facesheet of $t = d$ and $t = 1/2d$ respectively. (c): 75% open facesheet orientation ($D_{75} - L14$) where the red holes indicate the orientation of the top facesheet (the sheet in direct contact with the flow) and the blue holes that of the bottom facesheet (the sheet which is connected to the cavities). (d): 50% open facesheet orientation ($D_{50} - L14$) with the bottom plate shifted upstream. (e): 50% open facesheet orientation ($D_{50} - L14_{inv}$) with the bottom plate shifted downstream. (f): Hole orientation of the staggered configuration $L - L14_{stag}$ with a single facesheet where $t = d$. (g): Double staggered facesheet hole orientation ($D_{1.6} - L14_{stag}$), with the same fs_1 configuration as $L - L14_{stag}$ while the bottom facesheet is staggered in the mirrored direction w.r.t the red holes from (f) and are shifted upstream like fs_2 of (d) resulting in a 1.16% open configuration.

Simulations are carried out for several geometry variations, changing the percentage open area of the two facesheets. An overview of the DNS runs performed as well as those taken from Shahzad et al. (2023) as a reference case are presented in Table 7.3. As is indicated in the table, all simulations are performed under the same flow conditions with $Re_\tau \approx 500$ and all top facesheets of the liner configurations have the same single plate porosity of $\sigma = 0.142$. The gap spacing and both facesheet thicknesses and orifice diameter are kept constant throughout the simulations. The bulk Reynolds number remains at $Re_b \approx 8800$ for all liner cases.

The variations of the percentage open area result in changes in effective porosity from $\sigma_{eff} = 0.142$ to $\sigma_{eff} = 0.0023$. Percentage open areas of 100%, 75% and 50% are tested, where the orifices in the second factsheet are shifted upstream. These percentage open areas are tested to evaluate the effect of the shifting of the plates on the liner drag. These runs are referred to as $D_{(\%)} - L(\sigma(\%))_{geo}$ where the D indicates the double facesheet liner with a percentage open indication in the subscript. The 'L' refers to the low friction Reynolds number (from Shahzad et al. (2023)), $\sigma(\%)$ to the single facesheet porosity (expressed as a percentage). The 'geo' subscript refers to any geometry changes over the conventional orientation mentioned above. Next to the 3 different percentage open orientations, the effect of the

shifting direction of the orifices in fs_2 is evaluated where the geometry is changed from Figure 7.6 (d) to (e). This inversed shifted run is indicated by the 'inv' subscript.

In addition to the moderate opening percentages tested, a geometry is tested where the open percentage is reduced to 1.6% (7.6 (g)). In order to ensure the orifices in fs_2 did open into a cavity and a periodic spacing between these was maintained, the top facesheet has been staggered such that these variations led to a nearly fully closed configuration. As can be seen from Figure 7.6 (f) and (g), fs_1 has a staggered orientation and fs_2 (in the case of (g)) has been mirrored and is shifted upstream as far as the cavity walls would allow. The staggered configuration, with a single facesheet and $t = d$, has also been simulated to isolate the effects of the minimal percentage open orientation and, the potential, effect of staggering the holes. The $L_{stag} - L14$ run is performed as a reference run with the same dimensions as the $L - L14$ run with the only difference being the location of the orifices.

Case	Re_τ	Re_b	d^+	g^+	t^+_{fs1}	t^+_{fs2}	σ	σ_{eff}	ΔU^+	$C_f \times 10^3$	Δx^+	Δz^+	Δy^+_w	Ny	Tu_τ/δ
$S - L$	506.1	9268	0.0	-	-	-	0	0	0	4.578	5.1	5.1	0.80	150	37.8
$L - L14$	496.4	8794	39.7	-	39.7	-	0.142	0.142	0.54	4.855	1.0	1.0	0.80	500	32.8
$L_t - L14$	515.5	8794	41.2	-	41.2	-	0.142	0.142	0.67	4.856	1.5	1.5	0.82	500	26.1
$L - L14_{stag}$	508.7	8835	40.7	-	40.7	-	0.142	0.142	0.39	4.774	1.5	1.5	0.81	500	10.1
$D_{50} - L14$	509.4	8835	40.8	14.2	17.7	17.7	0.142	0.071	0.52	4.864	1.5	1.5	0.82	560	11.2
$D_{75} - L14$	511.0	8835	40.9	14.2	17.8	17.8	0.142	0.107	0.55	4.946	1.5	1.5	0.82	560	11.0
$D_{100} - L14$	506.1	8835	40.5	14.1	17.6	17.6	0.142	0.142	0.56	4.814	1.5	1.5	0.81	560	11.0
$D_{50} - L14_{inv}$	507.7	8835	40.6	14.1	17.7	17.7	0.142	0.071	0.56	4.901	1.5	1.5	0.81	560	10.9
$D_{1.6} - L14_{stag}$	507.0	8835	40.6	14.1	17.6	17.6	0.142	0.002	0.60	4.778	1.5	1.5	0.81	560	10.6

Table 7.3: DNS dataset of all runs of which results are used in the results section. The first 3 runs (S_L, $L - L14$ and $L_t - L14$) are performed by Shahzad et al. (2023)

7.3.2 Forchheimer coefficient

To contextualize the geometries listed in Table 7.3 with the Forchheimer coefficient and evaluate its suitability as a scaling parameter for double facesheet liners, it is essential to determine the Forchheimer coefficient for each geometry. This entails conducting simulations of laminar flow through the perforated plate configurations depicted in Figure 7.6 (b-g). Utilizing (5.1), the Darcy and Forchheimer permeability coefficients of these geometries are computed by analyzing the pressure differential between the inlet and outlet at various pore Reynolds numbers during simulations of normal flow through a perforated surface.

The simulations are performed in the same fashion as done by Shahzad et al. (2022). The geometry for a single cavity (as in Figure 7.6 (b-g)) is augmented to a unit square with a no-slip boundary condition applied to it. A schematic representation of the computational domain is illustrated in Figure 7.7 (a). At the inlet, situated on top of the domain, a constant superficial velocity U_t is prescribed, while a constant pressure is maintained at the outlet, at the bottom of the domain. Neumann boundary conditions are applied for both inflow pressure and outlet velocity. Symmetry boundary conditions are enforced along all sides of the domain.

The direct numerical simulation of laminar flow through the perforated plate involves solving the incompressible Navier-Stokes equations utilizing the pimpleFoam solver, which is part of the OpenFOAM library Weller et al. (1998). The temporal progression of simulations is done by a forward Euler time step scheme, adhering to a Courant-Friedrichs-Lewy (CFL) number of less than 0.7, until reaching a steady-state solution with residuals below 1×10^{-9}. Spatial solution computation employs a second-order central discretization scheme. The lengths of the inlet and outlet have been investigated by Shahzad et al. (2022), confirming a minimum requirement of $40d$.

The simulations encompass four distinct geometries: $D_{50}-L14$, $D_{75}-L14$, $D_{100}-L14$, and $D_{1.6}-L14_{stag}$. Notably, the orientation of the holes does not affect the pressure drop over the plates Tanner et al. (2019); Bae and Kim (2016). Therefore, $D_{50} - L14_{inv}$ shares its permeability coefficients with $D_{50} - L14$, and $L - L14_{stag}$ with $L - L14$, which is provided by Shahzad et al. (2023). Each geometry undergoes simulations at three distinct pore Reynolds numbers.

The pore Reynolds number (Re_p) is defined as $Re_p = U_p d/\nu$, where U_p denotes the pore-perceived velocity, defined as $U_p A_o = U_t A_p$ through mass conservation. Here, A_o represents the orifice area and

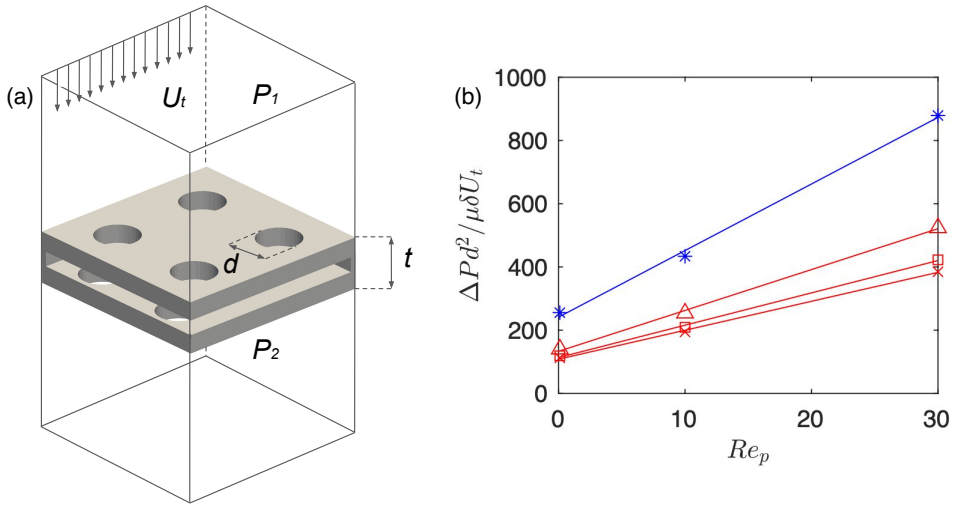

Figure 7.7: (a): Shows a sketch of the computational domain of the pressure drop simulations here the inlet velocity is indicated by U_t, the size of the orifice and the thickness of the plate by d and t respectively and the pressure at the inlet and outlet is indicated by P_1 and P_2. For the purpose of the illustration the side walls have been removed such the individual facesheet are visible In the simulation these are closed. (b): shows the results of the simulations, performed for $D_{50} - L14$ indicated by (△), $D_{75} - L14$ indicated by (□) and $D_{100} - L14$ indicated by (×) and $D_{1.6} - L14_{stag}$ indicated by (∗)

A_p indicates the plate area. Thus, the superficial velocity can be expressed as $U_p = U_t A_P/A_o = U_t/\sigma$, leading to $Re_p = U_t d/\sigma\nu$. In the simulations, pore Reynolds number adjustment is accomplished by varying the viscosity of the flow through the domain.

$$Re_p = \frac{U_p d}{\nu} \tag{7.5}$$

The Darcy and Forchheimer coefficients are determined through a least squares linear fit of the normalized pressure drop. In Figure 7.7 (b), the normalized pressure drop (left-hand side of (5.1)) is plotted against the pore Reynolds number. The slope of the fit provides $\alpha_y \sigma d$, while the y-axis intercept (at $Re_p = 0$) gives d^2/K_y.

Observing the figure, it is evident that the geometry with the smallest percentage open setting, $D_{1.6} - L14_{stag}$, exhibits the highest pressure drop over the facesheet across all Re_p. As the holes of the top and bottom facesheets become more aligned, the pressure drop over the facesheet diminishes. This trend aligns with the findings of La Rosa et al. (2021) for misaligned holes in subsequent plates. Moreover, the pressure drop varies more significantly, between cases, for higher Re_p. The computed values for the slope, the wall intercept of the normalized pressure drop, along with the Forchheimer coefficient and the Darcy permeability derived from them, are tabulated in Table 7.4.

In computing these values, the geometric variables considered include the orifice diameter, plate porosity, and plate thickness. When analyzing a single facesheet, there is no ambiguity in determining these variables. However, for a double facesheet configuration, decisions arise regarding which values to employ. Therefore it is necessary to highlight the variables used. The orifice diameter from Table 7.3 is utilized. Although Table 7.3 provides the effective porosity, the regular single-plate porosity is deemed more relevant due to its relevance for the computation of the pore perceived velocity through the conservation of mass. Additionally, the combined thickness of the two plates, rather than the total facesheet thickness (including the gap), is utilized for the plate thickness to ensure material permeability is adressed.

The table reaffirms the trends observed in Figure 7.7 (b). Specifically, it indicates that greater misalignment of the orifices in the plates corresponds to larger pressure drops and consequently smaller values for the inverse of the Forchheimer coefficient. A comparison with the values reported by Shahzad et al. (2023) reveals that the inversed Forchheimer coefficient values are indeed lower for the double facesheet configuration. However, there is a notable difference in the Darcy permeability coefficient, which is substantially higher for the dual facesheet liner cases compared to the values reported by Shahzad et al. (2023), while the geometries are similar.

Case	$\alpha_y \sigma d$	d^2/K_y	$1/\alpha_y^+$	$\sqrt{K_y}^+$
$L - L14$	6.61	371.63	0.859	2.06
$L_t - L14$	10.68	461.35	0.552	1.92
$L - L14_{stag}$	6.61	371.63	0.880	2.11
$D_{50} - L14$	13.02	133.96	0.439	3.52
$D_{75} - L14$	10.30	114.18	0.555	3.83
$D_{100} - L14$	9.22	108.88	0.620	3.88
$D_{50} - L14_{inv}$	13.02	133.96	0.439	3.51
$D_{1.6} - L14_{stag}$	21.20	242.87	0.270	2.60

Table 7.4: Values found for the slope and the wall intercept of the normalised pressure drop and converted to the viscous scaled Forchheimer and Darcy coefficient. The values of the first 3 cases are from Shahzad et al. (2023) and the remaining 5 originate from current simulations. Both the Forchheimer coefficient and the Darcy permeability are converted such that their unit is a length scale $[L]$. (The unit of α_y is $[L^{-1}]$ and of K_y is $[L^2]$)

Although, the relative values align with expectations, scaling inversely with the shifting distance. From the perspective of normal impinging flow on the surface, the values for the Darcy permeability seem unexpected, as it indicates the ease with which a fluid can pass through a medium. Where, due to the misalignment of the first and second facesheet orifices, one would expect that the flow encounters greater resistance. When considering the gap between the facesheets as additional permeability, however, the higher Darcy permeability for the dual facesheet liner cases becomes logical, as the flow benefits from additional release area between the plates compared to the single facesheet liner orifices, which primarily exhibit permeability in one direction.

Although hole orientation is insignificant to the pressure drop over the plates, the table does show slightly different values for $1/\alpha_y^+$ for the $L - L14$ and $L - L14_{stag}$ cases. This is however due to the difference in friction Reynolds number of the simulation. The same can be seen for $D_{50} - L14$ and $D_{50} - L14_{inv}$, which are effectively the same geometry but will have a different orientation with respect to the flow direction in the channel flow DNS runs. The effect of shifting direction together with the presence of the second facesheet in general will be discussed in the results section.

8

Results and discussion

The discussion of the results will begin with an evaluation and comparison of the instantaneous flow field of the various geometries. The primary aim of the results section is to address the main research questions posed in the problem statement, particularly concerning the impact of the dual facesheet configuration on the aerodynamics of an acoustic liner. Special attention will be given to assessing the additional drag induced by the dual facesheet configuration, examining the Reynolds stresses both above and below the facesheet, and exploring relevant scaling parameters or length scales that characterize the aerodynamic performance of the dual facesheet configurations.

8.1 Instantaneuous flow in channel

As extensively discussed in the previous chapter, the performance of the dual facesheet configurations with different percentage open configurations and two different top facesheet configurations (regular and staggered) are tested and compared to the reference cases provided by the study of Shahzad et al. (2023). The reference cases feature a single facesheet, allowing for a direct assessment of the impact of applying a second facesheet to the configuration.

To evaluate the impact of an additional facesheet on channel flow, we focus on streamwise velocity fluctuations, as illustrated in Figure 8.1. This figure provides a comparative analysis between a high-friction Reynolds number ($Re_\tau = 2000$) simulation by Shahzad et al. (2023) and the current work conducted at $Re_\tau = 500$. The x-z slice is taken at $y^+ = 5$ from the wall, offering insights into the flow behaviour. Figures (a) and (b) serve as reference cases, depicting streamwise velocity distributions for a smooth wall and a surface with $\sigma = 0.32$, respectively. Furthermore, figures (c) and (d) showcase scenarios with regular facesheet configurations, where (c) corresponds to a single facesheet, while (d) represents a double facesheet setup. Moreover, figures (e) and (f) maintain the same configuration but introduce a staggered arrangement for the top facesheet. This comparison provides valuable insights into how the additional facesheet alters streamwise velocity fluctuations, shedding light on the influence of different configurations on channel flow dynamics

Comparing the results of the cases of the current work (Figure 8.1 (c-f)), it is difficult to observe a notable difference between single and dual liner cases. This is especially evident when Figure 8.1 (a) and (b) are compared. The relative differences in the instantaneous flow velocity of the respective cases are much larger than seen for the cases of the current work. The lower friction Reynolds number, used in this study, results in a larger viscous length scale and thus relatively large small-scale structures compared to higher friction Reynolds number cases. Although the lower friction Reynolds number is beneficial from a computational standpoint the differences between the single and double facesheet configurations are not immediately evident from this instantaneous flow field.

The findings concerning the streamwise fluctuations may not be surprising, given that the primary function of the double facesheet is to attenuate wall-normal fluctuations originating from beneath the liner's surface. Consequently, it is not expected that the dual facesheet liner configuration would significantly affect the wall-parallel fluctuations above the liner surface. From the perspective of the channel, the geometry of the wall remains unaltered; the only modification introduced by the double-facesheet is an additional surface beneath the first facesheet and a thinner top-facesheet.

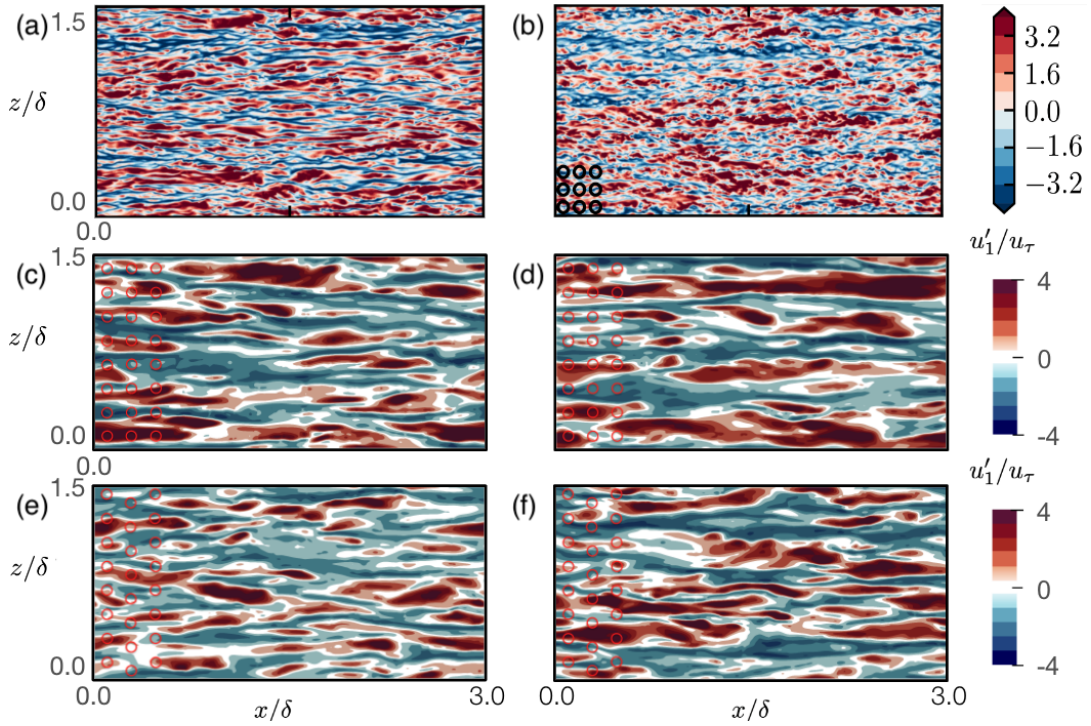

Figure 8.1: Comparision of the instantaneous streamwise velocity fluctuations u_1' of a reference case for (a): the $S-H$ run and (b) : the $L-H32$ run for the $Re_\tau = 2000$ cases of Shahzad et al. (2023) take at $y^+ + l_T^+ = 12$. Additionally, from the current work (c): $L-L14$, (d): $D_{100}-L14$, (e): $L-L14_{stag}$ and (f): $D_{1.6}-L14_{stag}$. All flowfields of the current work are x-z planes of the full domain taken at $y^+ = 5$. The location of the orifices is indicated for the first 3 rows at the left side of each case.

Whether similar results will be observed for cases with larger friction Reynolds numbers remains to be determined. This is particularly pertinent because the reduction of wall-normal velocity fluctuations could potentially elongate the streamwise streaks, as suggested by studies such as those conducted by Orlandi and Leonardi (2006) and Kuwata and Suga (2019).

In addition to investigating the streamwise velocity fluctuations, Figure 8.2 offers an overview of the same plane and flow cases as presented in Figure 8.1 (c-f) but for the wall-normal velocity fluctuations, u_2'. This variable is more affected by the design of the double facesheet liner. The theory posits that the wall-normal fluctuations originating from the orifices (Orlandi and Leonardi (2006), Shahzad et al. (2022), La Rosa et al. (2021)) are restricted due to the obstructed passage from the main channel to the cavities below. To assess this, Figure 8.2 compares the single facesheet liner (a) and the 100% open dual facesheet liner (b). Here, the effect of the second facesheet on the flow in the main channel, albeit close to the wall, would be visible, as these cases have the same effective porosity and only differ in the presence of a single or dual facesheet. Upon comparison, the differences appear to be fairly minimal, especially when examining the instantaneous velocity fluctuations where absolute differences are challenging to discern. However, it is noticeable that areas with high streamwise velocity fluctuations in Figure 8.1 (c) and (d) correspond to regions with high wall-normal velocity fluctuations in Figure 8.2 (a) and (b). This observation seems to corroborate the findings of Kuwata and Suga (2019) regarding the relationship between streak length and wall-normal velocity fluctuations.

One notable observation from Figure 8.2 is that the velocity fluctuations in the wall-normal direction are primarily influenced by interactions with the orifices. This observation aligns with the findings of Shahzad et al. (2023), as seen in Figure 8.2 (a). The additional wall-normal fluctuations are initiated by the presence of the orifices in the facesheet. However, the effect of inhibiting wall-normal velocity fluctuations due to the reduction of effective porosity (from Figure 8.2 (b) to (d)) is not observed in the channel. If any comparison can be made, it appears that there are more fluctuations emanating from the orifices of the $D_{1.6}-L14_{stag}$ configuration compared to the $D_{100}-L14$ case. This would oppose expectations however the instantaneous flow fields are not the most appropriate quantities to assess the degree of fluctuation in the channel. This assessment is continiued in the section concerning the Reynolds

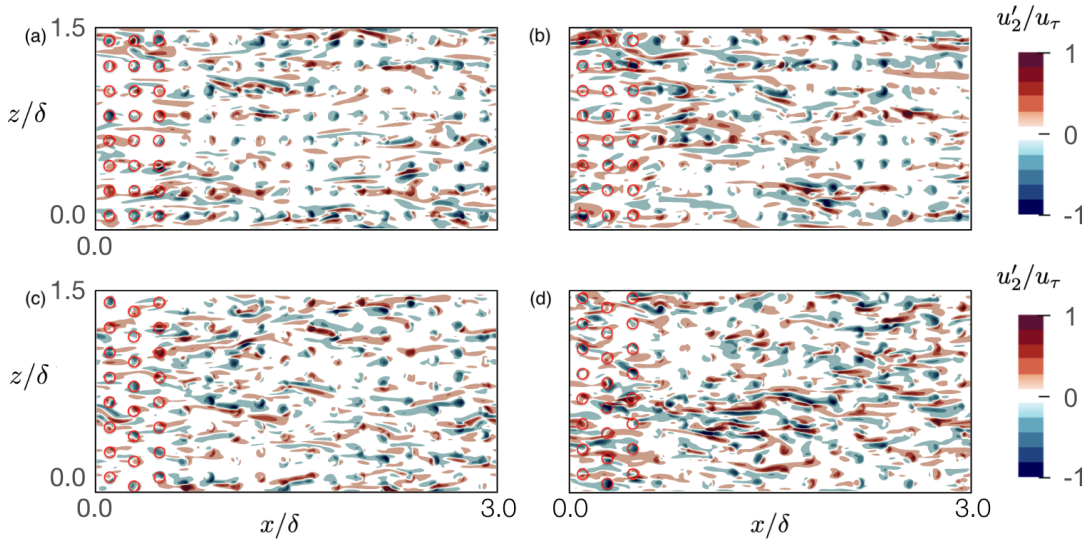

Figure 8.2: Comparision of the instantaneous wall-normal velocity fluctuations u_2' of (a): $L - L14$, (b): $D_{100} - L14$, (c): $L - L14_{stag}$ and (d): $D_{1.6} - L14_{stag}$. All flowfields are x-z planes of the full domain taken at $y^+ = 5$. The location of the orifices is indicated for the first 3 rows at the left side of each case.

stresses.

8.2 Mean Velocity profile

The theory section of this thesis has described that the origin of a smooth-wall boundary layer is found at the wall (i.e. $y = \delta$ or $y = -\delta$ for a channel flow). For rough-wall topographies, however, the origin of the boundary layer does not necessarily correspond to one of these locations. Often an offset is perceived between the physical location of the wall and where the flow perceives its origin. This effect, for instance, is observed in studies regarding passive drag reduction techniques such as riblets (Garcia-Mayoral and Jimenez (2011) Modesti et al. (2021)) or superhydrophobic surfaces (Rothstein (2010)). Wall offset in the positive wall-normal direction is often perceived in such studies, effectively imposing a slip condition on the wall and thus decreasing the drag of a surface.

Virtual origin

Unfortunately, liner-like surfaces do the opposite and shift the boundary layer and turbulence origin downwards. The origin of the boundary has rather been shown to reside below the original wall, as has effectively been illustrated through Figure 8.3 by Shahzad et al. (2023). When the direction of the shift is opposite, the effect it has, generally is opposite as well. As part of the turbulence of a perforated sheet

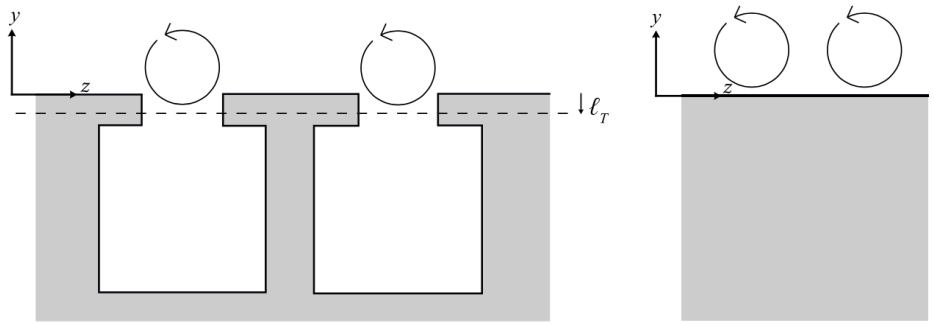

Figure 8.3: Schematic drawing of the near-wall turbulence over a porous and smooth surface, respectively. The virtual origin shift is indicated by l_T.

resides below the facesheet, a drag increase over a smooth wall is seen (Shahzad et al. (2023)).

When comparing mean profiles of rough and smooth surfaces, it is necessary to shift the wall-normal profiles in such a manner that the origin of the boundary layers coincide. This is often referred to as performing a virtual origin shift indicated by l_T^+. This is a relatively small shift (in this thesis it does not exceed $l_T^+ \leq 1.1$) and indicates the position of the wall as perceived by the near wall turbulent structures. Although small, the gradients close to the wall are substantial and thus the shift is necessary to perform.

The magnitude of the shift can be estimated by several methods, like those proposed by G. G. de Segura and García-Mayoral (2020) or Modesti et al. (2021) however in this instance the method proposed by Ibrahim et al. (2021) is used. Here, the Reynolds shear stress profile (τ_{12}) of the liner cases is shifted to coincide with that of the smooth wall. The virtual origin shift l_T ensures the profile collapses close to the wall. Shear stress profiles before (a) and after (b) the shift are illustrated in Figure 8.4. The comparison of these images demonstrates the effective collapse of all profiles near the wall. Due to small differences in geometry and moderate friction Reynolds numbers, the relative differences between the cases are limited.

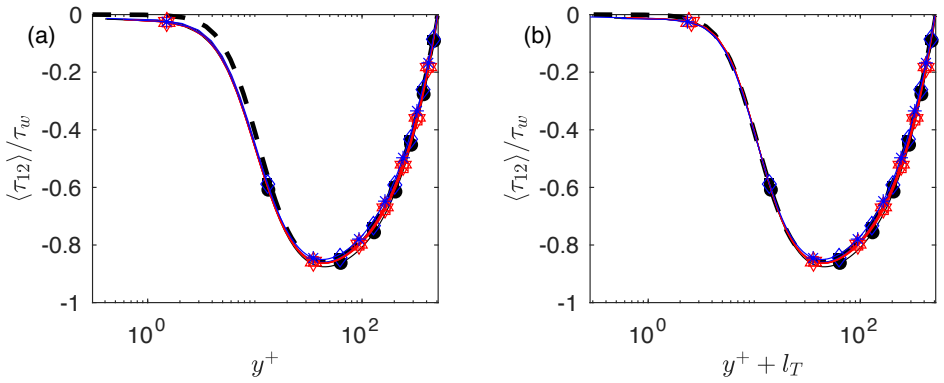

Figure 8.4: Averaged Reynolds shear stress $\langle\tau_{12}\rangle$ profiles vs. the viscous scaled wall distance y^+ without (a) and with (b) the virtual origin correction applied (l_T). The black dashed line indicates the $\langle\tau_{12}\rangle$ profile of the smooth-wall case ($S-L$: performed by Shahzad et al. (2023)). The liner cases are indicated by lines and corresponding coloured symbols as: $L-L14$ (■), L_t-L14 (●), $L-L14_{stag}$ (♢), $D_{50}-L14$ (△), $D_{75}-L14$ (□), $D_{100}-L14$ (×), $D_{50}-L14_{inv}$ (▽), $D_{1.6}-L14_{stag}$ (∗).

Velocity profiles

The virtual origin shifts, as defined above, are individually applied to each liner case to ensure an accurate comparison of the mean flow profiles. One of the primary insights gained from these profiles is the mean velocity profile, which offers valuable indications of the aerodynamic performance of the liners.

In Figure 8.5, a comparison of the mean velocity profiles of the liner cases outlined in Table 7.3 is presented. In Figure 8.5 (a), it is evident that all liner cases exhibit some degree of drag increase compared to the smooth-wall configuration. A closer zoomed version of the mean velocity profiles of (a) can be found in Figure 8.5 (c). This reveals that the mean velocity profiles of all regular, dual, facesheet liner cases collapse onto the $L-L14$ liner case at $y^+ = 100$. Notably, the L_t-L14 liner geometry shows a larger difference in mean velocity with the smooth-wall reference. Despite both $L-L14$ and L_t-L14 sharing the same geometry when viewed from a y-normal plane, they display a difference in drag. The thickness of the L_t-L14 case's facesheet is half that of $L-L14$ and exhibits a larger mean velocity deviation, consistent with other thinner facesheet configurations (Shahzad et al. (2023)). However, the dual facesheet liner cases depicted in Figure 8.5 have even thinner top facesheets than L_t-L14, yet they do not exhibit higher drag than the L_t-L14 case. This suggests that the second facesheet does impact drag, providing a reduction compared to a single thin facesheet. The percentage open variation does not have a notable effect when considering these specific plots.

Figure 8.5 (b) illustrates the comparison of the mean velocity profile with more diverse cases. Upon comparing 8.5 (a) to (b), minimal visible differences are noticeable, directing attention to 8.5 (d). Noticeably, larger differences in geometries are evident. Firstly, the staggered single-facesheet ($L-L14_{stag}$) case exhibits a reduction in drag compared to the $L-L14$ case. This suggests that introducing a spanwise

variation in the facesheet orifice pattern diminishes drag relative to the baseline liner case $L-L14$ at low friction Reynolds numbers. However, this outcome does not extend to the double facesheet and double staggered case ($D_{1.6}-L14_{stag}$), as one might expect based on the Forchheimer coefficient provided in Table 7.4. The $D_{1.6}-L14_{stag}$ case presents slightly lower drag figures than L_t-L14, yet it performs inferiorly to $L-L14$ and all streamwise shifted cases from both 8.5 (a) and (b). The inversely shifted dual facesheet liner configuration yields very similar results to all red cases in 8.5 (a), maintaining the absence of a visible correlation between added drag and percentage open variation from the mean velocity profiles.

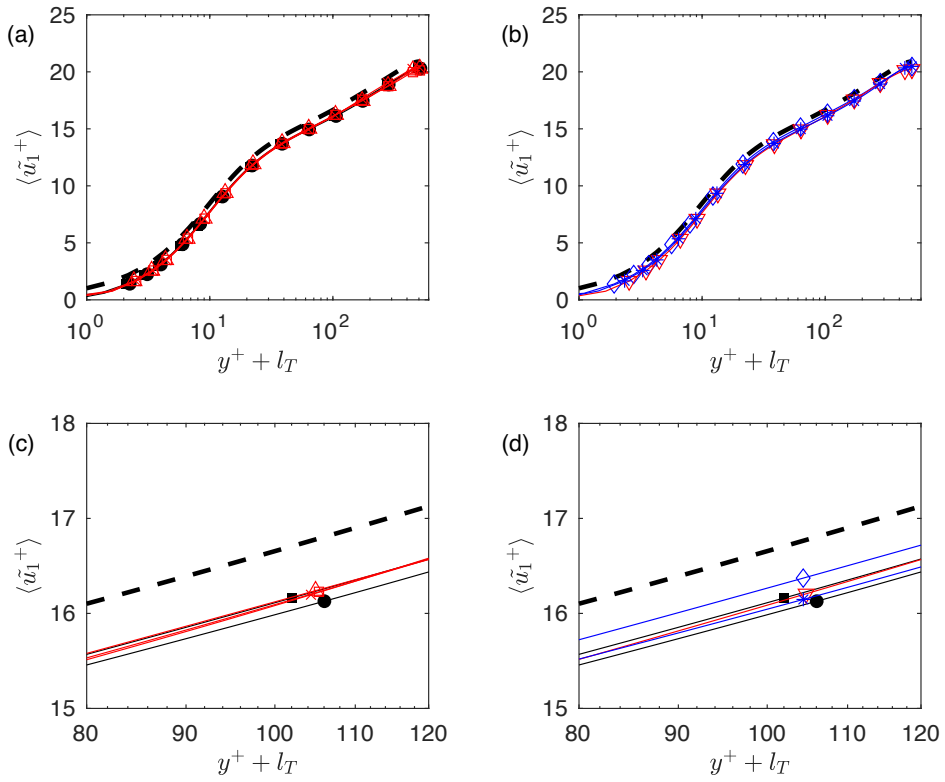

Figure 8.5: Comparison of the mean velocity profile $\langle \tilde{u_1}^+ \rangle$ versus the viscous scaled wall normal distance y^+. All figures show the three reference cases in black: the smooth wall $S-L$ reference case by the black dashed line (- -), $L-L14$ by (■) and L_t-L14 by (•). (a), compares these reference cases to the streamwise shifted dual facesheet liner cases $D_{50}-L14$ (△), $D_{75}-L14$ (□) and $D_{100}-L14$ (×). (b) Shows the runs with a different fs_1 configuration like, $L-L14_{stag}$ (◇) and $D_{1.6}-L14_{stag}$ (∗) as well as the inverse shifted dual facesheet liner case $D_{50}-L14_{inv}$ (▽). (c) and (d) are the zoomed-in images of (a) and (b) respectively.

Added drag

The apparent absence of a visible effect from shifting fs_2 leads to a further investigation into the impact of shifting the dual facesheet on added drag. This investigation employs the Hama roughness function, as defined in Equation 4.4, to provide ΔU^+ values for each run at $y^+ = 100$. Firstly, assessing the relative effect of shifting the second facesheet further out of alignment with the top facesheet. Figure 8.6 is devised for this purpose, illustrating the effect of percentage open settings on ΔU^+ in (a). In (b), ΔU^+ is depicted as a function of d^+_{stag} for all cases considered in this work. In this figure, the influence of the shifting distance becomes more apparent. Here lower, positive, percentage open areas (indicating smaller effective openings) correlate with lower ΔU^+ values. Notably, a discernible difference in velocity deficit is observed, wherein positive staggering percentages in Figure 8.6 (a) and positive staggering distances in (b) lead to a reduction in added drag.

However, staggering in the opposite direction, (shifting fs_2 downstream) does not result in a similar velocity deficit compared to runs shifted upstream. This observation suggests that shifting the bottom face upstream has a more favourable effect on drag. This aligns with the hypothesis that flow is more

restricted by the second facesheet in this configuration. However, the definitive impact of this effect needs to be established through analysis of the instantaneous flow fields, which will be addressed later in this chapter.

Furthermore, the staggered facesheet configuration of $D_{1.6} - L14_{stag}$ ($*$) does not adhere to the initially observed trend. Consequently, it remains inconclusive whether this configuration exhibits less added drag compared to a case with a larger percentage open area and the same facesheet. These results deviate from expectations, particularly when considering the difference between single facesheet and double facesheet configurations, as depicted in Figure 8.5. The non-staggered 'regular' fs_1 (red) cases show minimal disparity in velocity deficit compared to the non-staggered single facesheet liner reference case $L - L14$. However, the staggered facesheet (blue) cases exhibit significant differences between single and double facesheet configurations. It will be intriguing to explore whether there are notable distinctions in qualitative flow behaviour between these cases, as the currently presented results are inconclusive.

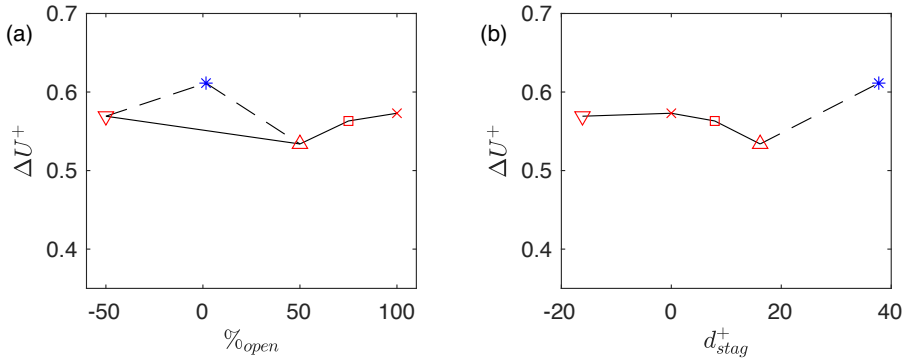

Figure 8.6: Comparison of the viscous scaled velocity deficit (ΔU^+) of the dual facesheet cases versus the percentage open ($\%_{open}$) in (a) and the staggering distance d^+_{stag} in (b). The black lines are merely a visual aid to see a relationship between the velocity deficit of the respective runs. The only double facesheet configuration with a staggered top facesheet ($D_{1.6} - L14_{stag}$) is connected by a dashed line as the stagger magnitude change is not the only difference compared to the regular dual facesheet liner cases. The symbols represent the cases as: $D_{50} - L14$ ($\triangle$), $D_{75} - L14$ ($\square$), $D_{100} - L14$ ($\times$), $D_{50} - L14_{inv}$ ($\triangledown$) and $D_{1.6} - L14_{stag}$ ($*$).

Friction coefficient

When considering the friction coefficient of the respective cases, however, there is some discrepancy found between the indications provided by the velocity deficit and the friction coefficient. The friction coefficients for the runs are provided in Table 7.3. From these coefficients, the drag variation in percentages

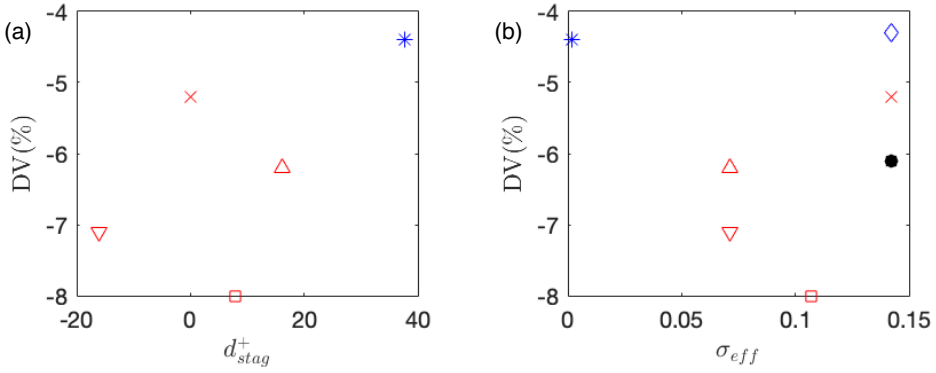

Figure 8.7: Drag variation (in %) for the different double liner cases displayed versus (d^+_{stag}) in (a) and versus the effective porosity (σ_{eff}) in (b). The liner cases are indicated by the following symbols: $L - L14$ ($\blacksquare$), $L_t - L14$ ($\bullet$), $L - L14_{stag}$ ($\diamondsuit$), $D_{50} - L14$ ($\triangle$), $D_{75} - L14$ ($\square$), $D_{100} - L14$ ($\times$), $D_{50} - L14_{inv}$ ($\triangledown$), $D_{1.6} - L14_{stag}$ ($*$).

can be extracted using (7.4), as illustrated in Figure 8.7. In (a), the figure depicts the drag variation in percentages versus the staggering distance of all the dual facesheet liner cases, while (b) shows the relation of the drag variation to the effective porosity of both the dual and single facesheet liner cases. The figure reveals a different relationship between the drag variation and the staggering distance than what is found for the velocity deficit. Specifically, the results for the double staggered configuration ($D_{1.6} - L14_{stag}$) more closely align with expectations and correlate with the single, staggered, facesheet reference case ($L - L14_{stag}$). However, the regular facesheet liner cases show no apparent relation to the staggering distance or the effective porosity, unlike what is observed for the velocity deficit. This discrepancy between the relationship of the parameters to the velocity deficit and the friction coefficient could be attributed to the limited runtime provided for the thesis, which might benefit from additional runtime. Since the velocity deficit is a more universal quantity that compares to other results regardless of the friction Reynolds number (a direct result of the outer layer similarity Townsend (1956)), it will be used throughout the remainder of the results.

This result additionally shows that the relative differences are fairly small. According to Shahzad et al. (2023) the highest drag increase for a liner cases compared to a smooth wall was found to be 70%. This however is an extrapolation of the drag variation to a Reynolds number of a full-scale aircraft possible due to the approach of the fully rough regime in the results found. In this thesis, the highest percentage increase is 8% and the differences among the cases are within a 4% spread. This indicates the relative differences which can be attained with fairly low Reynolds number simulations. In order to enlarge relative differences, higher porosity and friction Reynolds number runs are advised.

8.2.1 Relevant parameters for ΔU^+

One of the main difficulties with the determination of drag for rough surfaces is the lack of an appropriate function which can determine the added drag of a surface. Shahzad et al. (2023) has, however, found that the inverse of the Forchheimer coefficient, for single facesheet liners, shows a monotonically increasing relationship with the velocity deficit. This means that for an increase in $1/\alpha_y^+$ an increase of ΔU^+ was experienced.

The Forchheimer coefficients for all the double facesheet configurations considered in this work are provided in Table 7.4. Figure 8.8 illustrates the corresponding velocity deficit values plotted against these Forchheimer coefficient values in (a). Additionally, as a reference, all of the thick and thin single facesheet liner cases from Shahzad et al. (2023) are included in the figure. These reference cases exhibit larger changes in the Forchheimer coefficient due to varying plate porosities and a larger viscous scaled orifice diameter (due to an increase in Re_τ).

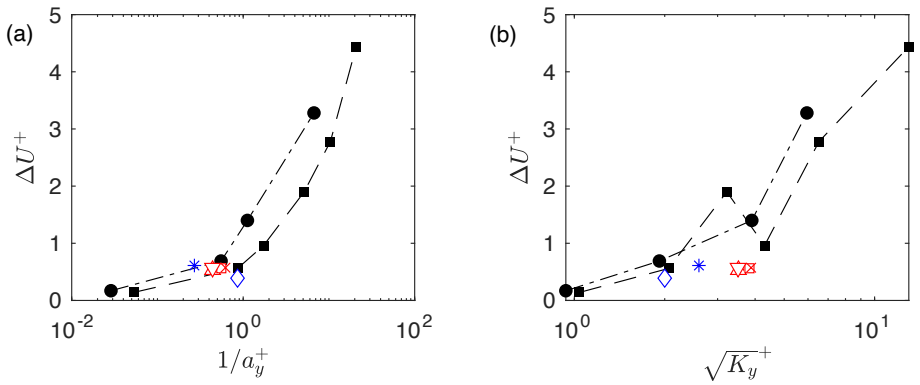

Figure 8.8: ΔU^+ as a function of the Forchheimer coefficient $1/\alpha_y^+$ (a) and the Darcy permeability $\sqrt{K_y}^+$ (b). The reference cases from Shahzad et al. (2023) for the thick (plate thickness $t = d$) and thin (plate thickness $t = d/2$) facesheet are indicated by (– – ■) and (– - •) respectively. The liner cases of this work are indicated by the following symbols: $L - L14_{stag}$ (◇), $D_{50} - L14$ (△), $D_{75} - L14$ (□), $D_{100} - L14$ (×), $D_{50} - L14_{inv}$ (▽), $D_{1.6} - L14_{stag}$ (∗).

As evident from Figure 8.8 (a), the range of Forchheimer coefficients in the current work is considerably smaller than that of the reference cases. Moreover, the observed trend for increasing Forchheimer coefficient, in the double liner cases, corresponds to a decreasing velocity deficit, contrary to the trend

observed in the reference case. This suggests that for a double facesheet, either the Forchheimer coefficient is not a relevant scaling parameter, or the change in the Forchheimer coefficient of a dual facesheet liner, is due to factors not captured in (5.1).

For the regular double facesheet cases, with a small shift in fs_2, the velocity deficit for the respective Forchheimer coefficients does correspond fairly well to the reference cases. Here the larger the staggering distance, the larger the discrepancy between the trend observed in the reference case and the trend in the current work. The largest staggering distance (found for $D_{1.6} - L14_{stag}$) shows the largest deviation from the trend line of the reference cases. This implies the relation between the staggering distance and the deviation of the proposed theory of Shahzad et al. (2023).

The reference cases in the figure readily show that a difference in facesheet thickness results in a separate line for those cases. The same effect could be at hand for the dual facesheet liner cases, where the thickness of each facesheet or a combination of a staggering distance and gap spacing determines its own relation. Consequently, the Forchheimer coefficient for a specific case may only be altered by changes in diameter or plate porosity, rendering it more useful as a combined factor of diameter and porosity rather than a distinct scaling parameter. The plate porosity and orifice diameter have often been cited as factors affecting the added drag of a porous surface (Howerton and Jones (2015)).

Figure 8.8 (b) shows the same velocity deficit as (a) however now as a function of the Darcy permeability. The figure identically contains the reference cases for the thin and thick facesheet from Shahzad et al. (2023). As Table 7.4 shows, the Darcy permeability coefficient is much higher for the dual facesheet liners when compared to the reference cases. As a result, there is a less pronounced relation between the Darcy permeability and the added drag. The results from the present work show little to no change in velocity deficit for increasing $\sqrt{K_y}^+$.

To be able to place the velocity deficit of a double facesheet liner into the results from Shahzad et al. (2023), the geometries need to be tested at different friction Reynolds numbers and porosity. The current data set is not sufficient to draw conclusions on the monotonic relations of velocity deficit to the Forchheimer or Darcy coefficient. The regular double facesheet liners with small staggering distances do find similar velocity deficit values to the single facesheet liner cases for similar Forchheimer coefficients. So although there is no observation of a similar monotonically increasing relation, there is some predictive function of the value of the inversed Forchheimer coefficient and the added drag of the liner.

As the geometries in the current work do have a difference in staggering distance, there can be an investigation if an effective hole size or porosity can be a scaling parameter as these do differ from case to case. To assess whether the size of the effective hole, left after staggering, is a relevant parameter, the effective radius and the effective porosity are employed. Here the effective porosity is defined as has been described in the methodology and the effective radius (r^+_{eff}) is defined as:

$$r^+_{eff} = \sqrt{\epsilon_o} r^+ \tag{8.1}$$

here the effective radius is determined by multiplying the square root of the opening ratio of the configuration (ϵ_o) with the radius of a single orifice, denoted as r (i.e., $r = d/2$). The opening ratio is the ratio of the effective open area of the orifice and the total single orifice area (i.e. $\epsilon_o = A_{eff}/A$). Figure 8.9 visualises how the computation of the effective radius can be performed with basic geometric relations and the fact that $A_{eff} = \epsilon_o A$. In Figure 8.9, A represents the area of a single orifice and ϵ_o is the opening ratio of the specific case. The effective radius r_{eff} corresponds to the radius that a circular orifice would have if it were to possess the same area as A_{eff}.

Figure 8.10 shows the velocity deficit plotted as a function of the effective radius of the orifice (a) and the effective porosity of the plate (b). In 8.10 (a), relatively small differences without a monotonic relation can be observed between the velocity deficit and the respective effective radius. Additionally, the effects of the staggering direction are not captured as there is no distinction between the effective radius for the shifting direction. The figure therefore shows that this metric is not the most appropriate length scale.

In order to assess the velocity deficit with respect to the reference cases, the staggering distance cannot be used as it is not a parameter present in single facesheet liners. However, the effective porosity can be related to all liners, and therefore, the reference cases can be included in Figure 8.10 (b). The figure shows the velocity deficit of all cases discussed in Table 7.3 as a function of the effective porosity. Here it can be observed that at $\sigma_{eff} = 0.142$ there are several cases where a different velocity deficit is found for

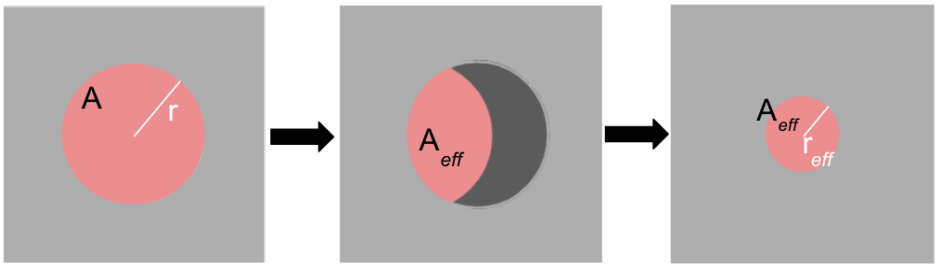

Figure 8.9: Schematic drawing of how r_{eff} is computed. This example shows the case for $D_{50} - L14$.

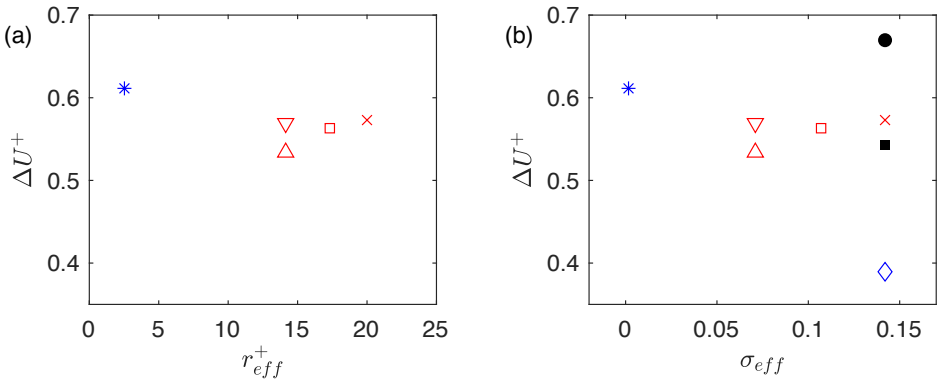

Figure 8.10: Viscous scale velocity deficit (ΔU^+) compared to the effective orifice radius in viscous units (r^+_{eff}) displayed in (a) and the effective porosity of the orifice $\sigma)eff$ in (b). Coloured symbols indicate the different liner cases as: $L - L14$ (■), $L_t - L14$ (●), $L - L14_{stag}$ (◇), $D_{50} - L14$ (△), $D_{75} - L14$ (□), $D_{100} - L14$ (×), $D_{50} - L14_{inv}$ (▽), $D_{1.6} - L14_{stag}$ (∗).

the same effective porosity. This indicates that the effective porosity does not provide all the necessary information and that the effective porosity cannot be treated similarly to the single plate porosity, as the added drag scales with the plate porosity (Howerton and Jones (2017)), and liner cases with the same effective porosity show different velocity deficit values.

From this discussion, it is evident that shifting fs_2 from $D_{100} - L14$ to $D_{50} - L14$ reduces the added drag of the liner from slightly more than the reference case to slightly less. This suggests that, although minimal, some added drag reduction can be achieved by a double facesheet configuration when shifted far enough. However, the staggering of the single facesheet liner results in a much greater reduction of the added drag, consistent with the findings of Zheng et al. (2022b), who suggest that larger spacing between the holes in the streamwise direction leads to less added drag.

Furthermore, when the velocity deficit of the dual facesheet liner is placed in the context of the Forchheimer coefficient, along with the reference cases, it becomes evident that the range of Forchheimer coefficient values in the current work is not sufficient to assess a relationship between the added drag and the inverse of the Forchheimer coefficient. The variation of the added drag between the dual facesheet liner configurations is very small, making it difficult to determine a relevant length scale in the geometry with which the velocity deficit scales.

8.3 Reynolds stresses

The mean velocity profiles and velocity deficit exhibit minimal changes across the flow cases. Given the evident distinctions in geometries, the discussion now shifts towards investigating the Reynolds stresses in the channel. Figure 8.11 presents a comparison of all non-zero Reynolds stresses in the channel. An observable trend emerges from the results of the Reynolds stresses between the smooth wall and the liner cases. Due to the wall roughness of the porous liners, Figure 8.11 (a) indicates a slight decrease in the peak value of $\langle \tau_{11} \rangle$ for the liner cases compared to the smooth wall. Consistently, 8.11 (b,c) depict an increase in peak value, aligning with findings from previous studies on porous liners (Kuwata and Suga

(2016), Shahzad et al. (2023)). Notably, the stresses near the channel centerline in all figures closely resemble those of the smooth-wall case, suggesting outer layer similarity.

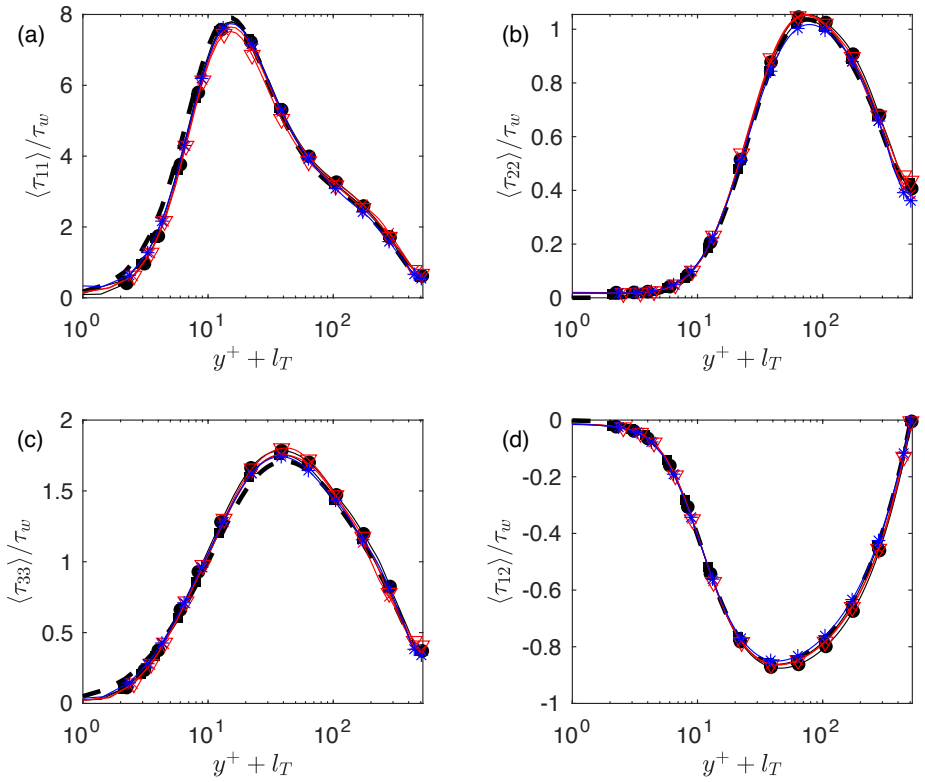

Figure 8.11: Comparison of the intrinsic averaged Reynolds stress profiles. The primary, non-zero directions of the Reynolds stresses are given, i.e. (a): $\langle\tau_{11}\rangle/\tau_w$, (b): $\langle\tau_{22}\rangle/\tau_w$,(c): $\langle\tau_{33}\rangle/\tau_w$ and (d): $\langle\tau_{12}\rangle/\tau_w$ for the cases: S-L (- -), $L - L14$ (■), $L_t - L14$ (•), $D_{100} - L14$ (×), $D_{50} - L14_{inv}$ (▽), $D_{1.6} - L14_{stag}$ (∗). Some of the liner cases' results have been omitted for the clarity of the illustration. The double-liner cases (red) shown are selected as these represent the largest difference between the four cases. $D_{75} - L14$ and $D_{100} - L14$ values lay in between the two shown results.

The results provided in Figure 8.11 are those above the facesheet of the liner. As the geometry of fs_1 has been kept the same as that of the single facesheet liner, the small differences in Reynolds stresses can be attributed to the lack of change. The question arises, where the differences *are* visible, as they are minimal above the wall. Since the largest geometrical changes are present beyond the facesheet, the interest turns to the flow below the wall locations (i.e. $y/\delta \leq -1$ and $y/\delta \geq 1$).

Wall normal velocity fluctuaions

One of the main hypotheses of this thesis has been founded on the work on the Forchheimer coefficient of Shahzad et al. (2023). Where the limiting of the pressure drop over the porous facesheet would reduce the added drag of the liner. This has resulted in the attempt to reduce the pressure drop over the liner by the staggering of the two facesheets as done in La Rosa et al. (2021). The increase in the pressure drop over the plates in that work, however, is seen for normal flow impinging on two plates filled with staggered orifices at different distances. This leads to the question if the same effect is seen for staggered orifice plates with grazing flow instead of normal flow impinging on the surface.

The notion of limiting the pressure drop over the facesheet for drag reduction aligns with the findings of Orlandi and Leonardi (2006) and Gustavsson et al. (2019), where it was discovered that the Root Mean Square (RMS) of the wall-normal fluctuations served as an appropriate scaling parameter for the velocity deficit. These fluctuations are indicative of the momentum transfer between the flow above and below roughness elements. The RMS of the velocity fluctuations is found in the Reynolds stresses along their principal directions (i.e., $\tau_{ii} = \langle u_i' u_i' \rangle$), making the Reynolds stresses a crucial quantity for evaluating the behaviour of the flow under the influence of an additional facesheet.

In order to see if the double facesheet can attain a reduction in the momentum transfer between the channel and the orifices and to see the effect of the staggering distance on the flow, Figure 8.12 is employed. The figure shows the normalised wall-normal velocity fluctuations u_2'/u_τ through the facesheet in a single cavity zoom. All orifices in the top facesheet show vortices inside them, where the flow impinges on the rearward surface and funnels downward creating a vortex in the orifice.

As can be seen from 8.12 (a) compared to all other images of 8.12, the reference case's liner thickness is much thicker than that of the dual facesheet liner cases. This is the only instance where the upstream wall of the orifice interacts with the into-the-cavity fluctuation. In all other instances, due to the thinner facesheet, the downward momentum finds a release in the downstream direction as it is less restricted.

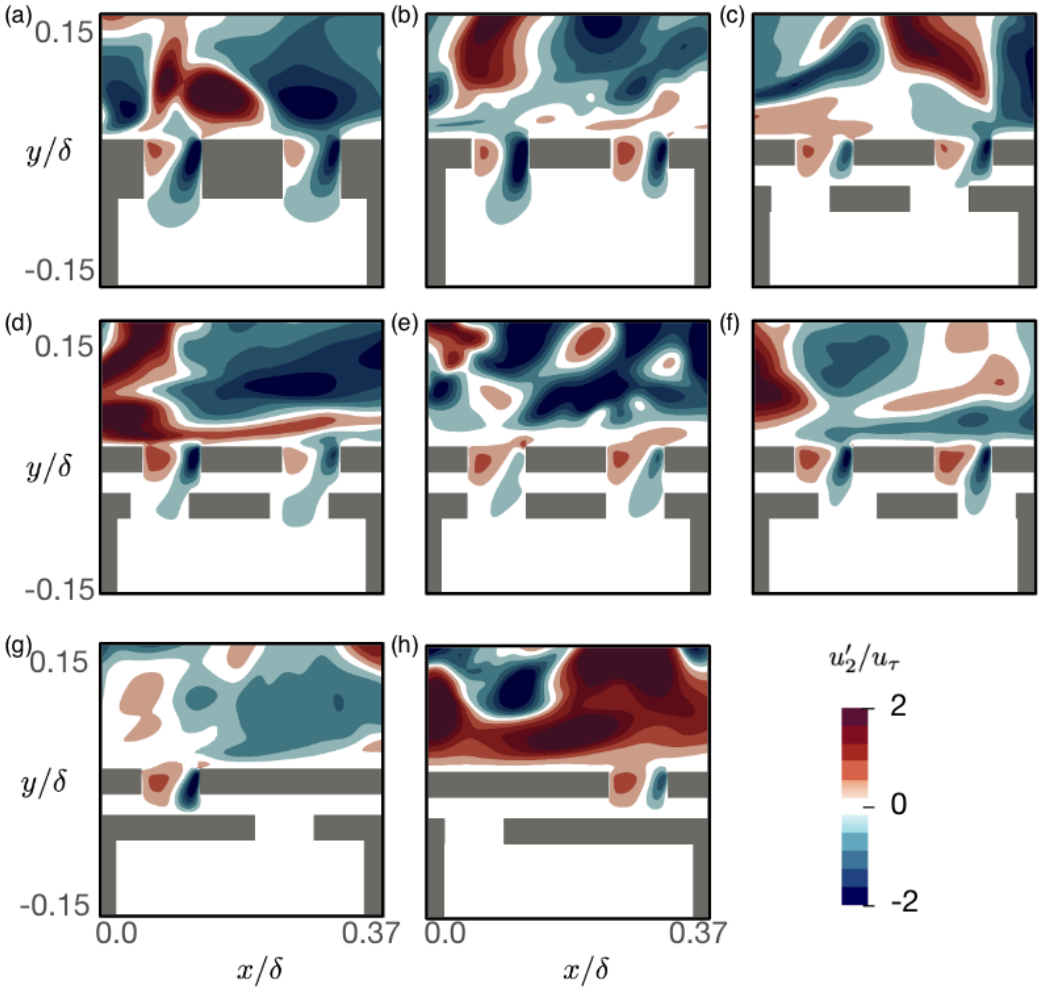

Figure 8.12: Normalised instantaneous wall-normal velocity fluctuations u_2'/u_τ zoomed in at a cavity. The cases displayed are (a): the thick-wall reference case $L - L14$, (b): the thin-wall reference case $L_t - L14$, (c): the 50% open dual face-sheet liner case $D_{50} - L14$, (d): the 75% open dual face-sheet liner case $D_{75} - L14$, (e): the 100% open dual face-sheet liner case $D_{100} - L14$, (f): the 50% open, inversed, dual face-sheet liner case $D_{50} - L14_{inv}$, (g and h): the double staggered liner with 1.6% open configuration $D_{1.6} - L14_{stag}$. Here (g) shows the plane through the orifices which are closest to each other and (h) the orifices with the largest distance between them.

This however is primarily focused on the region just below the top facesheet. Of greater interest is the interaction of the flow through the orifices with the cavity below. Figure 8.12 (c), (d) and (e) show how the wall-normal fluctuations are restricted due to the second facesheet. Here the effect of the staggering distance is evident, as a larger shift limits the wall-normal velocity fluctuations into the cavity. This effect aligns with observations from the velocity deficit, where a greater upstream staggering of the bottom facesheet results in a lower added drag. These figures show how the flow is being restricted by the second facesheet when in place. This reiterates that the reduction of the momentum transfer between above and

below the facesheet can be attained by the correct staggering of the facesheet. This shows the influence of the wall-normal velocity fluctuations on the added drag of the liner.

Interestingly, these results also show the effect of the staggering direction of the second facesheet on the flow. A comparison between Figure 8.12 (c) and (f), illustrating the wall-normal velocity fluctuations of $D_{50} - L14$ and $D_{50} - L14_{inv}$ respectively, reveals the impact of the shifting direction direction of fs_2. In Figure 8.12 (c), there is a noticeable restriction of the negative fluctuation by the second facesheet. Conversely, in Figure 8.12 (f), the second facesheet orifice appears to accommodate the negative fluctuation. Moreover, the positive fluctuation in the cavity appears more contained due to the facesheet in (f). As the channel is the main momentum source, however, restricting the negative fluctuation does seem to have more of an effect on the reduction of the added drag than its opposite.

Figure 8.12 (g) and (h), display u_2'/u_τ of the two aligned hole situations in the x-y plane. These images are obtained by slicing the z-normal plane through the middle of one orifice in the top facesheet and intersecting it with the middle of one orifice in the bottom facesheet. As depicted, this results in a considerable staggering distance in the streamwise direction. However, these images may appear somewhat distorted due to the nearest orifice being further back into the spanwise direction, causing a slight overlap, as illustrated in Figure 7.6 (g).

In Figure 8.12 (g) and (h), we observe how the vortex inside the facesheet orifice is contained by the second facesheet. This observation supports the concept that the second facesheet can restrict the momentum transfer between the channel and the cavities. This effect becomes particularly evident when compared to other cases, where there is a noticeable jet-like fluctuation into the cavities. While this effect is observed, for the staggered cases, the instantaneous figures, of the wall-normal flow, do not tell the full story, especially when considering the large increase of added drag boasted by the $D_{1.6} - L14_{stag}$ case.

Spanwise velocity fluctuations

The previous discussion highlighted the impact of the second facesheet on wall-normal velocity fluctuations, shedding light on the vertical interactions of the flow with the dual facesheet liners. However, wall-normal fluctuations only reveal one aspect of the flow dynamics. Figure 8.13 provides a view similar to Figure 8.12, but now presents the instantaneous normalized spanwise velocity fluctuations u_3'/u_τ. Here, the effect of the second facesheet on wall-parallel flow in the spanwise direction becomes apparent. Upon examining the figure, it becomes evident that the influence of the impinging flow onto the facesheet, as observed in Figure 8.12, extends beyond vertical flow restrictions, with the instantaneous flow indicating the presence of non-zero velocity between the facesheets.

In the orifices of all figures in Figure 8.13, spanwise fluctuations can be observed, indicating the presence of three-dimensional fluctuations. However, judging the strength of each direction from 2D instantaneous velocity fields is challenging. Unlike wall-normal velocity fluctuations, which are caused by the impinging flow on the downstream edge of the orifice, the spanwise fluctuations do not have a clear driver and are more likely a consequence of the turbulent fluctuations in the main channel. Comparing the single liner facesheet in both Figure 8.13 (a) and (b) to all dual liner cases (c-h), the positive and negative regions of the fluctuations are not uniform for each case, unlike the situation in Figure 8.12.

By the comparison of Figure 8.13 (a) and (b), the difference in how the thin facesheet liner contains the velocity fluctuations in the orifice is clear. In Figure 8.13 (a), spanwise fluctuations in the cavity are not evident, whereas Figure 8.13 (b) shows spanwise fluctuations penetrating into the cavity. This indicates that a facesheet with the thickness of $L_t - L14$ is not thick enough to prevent the spanwise fluctuations from appearing below the facesheet. The same phenomenon is observed for the spanwise fluctuations below fs_1 in all double facesheet liner cases, where the flow penetrates into the facesheet gap and is perceived to flow between orifices.

When Figure 8.13 (c) showing $D_{50} - L14$ and (f) showing $D_{50} - L14_{inv}$ are compared, the effect of the staggering distance is seen from the penetration of the spanwise fluctuations into the orifices in fs_2. Although the downstream edge of the orifice is a less clear cause of the spanwise velocity fluctuations, the difference in the staggering directions can be profoundly distinguished. The upstream-shifted case exhibits some spanwise fluctuations in the gap with minimal interaction with the orifice in fs_2. In contrast, the inversely staggered configuration clearly shows spanwise fluctuations penetrating into the cavity. These observations regarding the interaction of flow with the orifices in fs_2 align with the

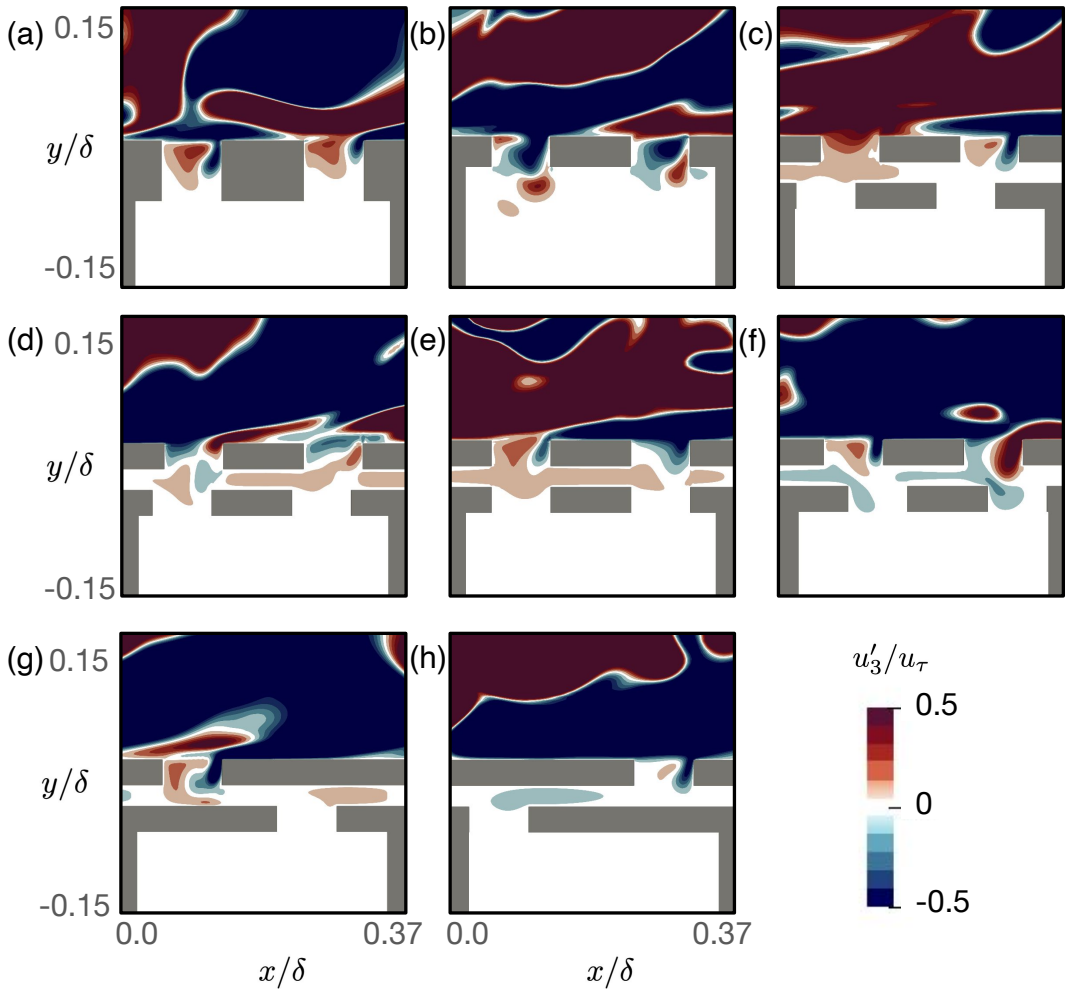

Figure 8.13: Normalised instantaneous spanwise velocity fluctuations u_3'/u_τ zoomed in at a cavity. The cases displayed are (a): the thick-wall reference case $L-L14$, (b): the thin-wall reference case L_t-L14, (c): the 50% open dual face-sheet liner case $D_{50}-L14$, (d): the 75% open dual face-sheet liner case $D_{75}-L14$, (e): the 100% open dual face-sheet liner case $D_{100}-L14$, (f): the 50% open, inversed, dual face-sheet liner case $D_{50}-L14_{inv}$, (g and h): the double staggered liner with 1.6% open configuration $D_{1.6}-L14_{stag}$. Here (g) shows the plane through the orifices which are closest to each other and (h) the orifices with the largest distance between them.

penetration of wall-normal fluctuations depicted in Figure 8.12, suggesting that 3D flow phenomena involve both wall-normal and wall-parallel fluctuation directions (i.e., turbulent fluctuations).

Figure 8.13 (g) and (h) depict the same case, $D_{1.6}-L14_{stag}$, with the x-y plane taken from different perspectives, both through the middle of one of the orifices of the staggered configurations. These figures illustrate spanwise flow between the plates, which is primarily induced by the orifice positioned behind or in front of it along the z-direction. The flow appears to impinge on fs_2 and then flows towards the nearest orifice in the spanwise direction, as it represents the nearest path of relief. Further discussion on the behavior of flow between the facesheets will be continued in the dedicated section later in the results.

Below the regular facesheet

In order to assess the flow between the facesheets, the following section focuses on the Reynolds stresses below the wall. Figure 8.14 (a) and (c) show $\langle\tau_{22}\rangle$ for the straight shifted cases. The wall-normal Reynolds stresses are plotted against the location below the facesheet. Here (a) shows the top of the facesheet at $y^+=0$ until $y^+=-40$ and (c) shows a zoom at the facesheet gap from $y^+=-17$ to $y^+=-31$. As can be observed in (a), all cases exhibit very similar Reynolds stresses from the beginning of the facesheet at $y^+=0$ to the end of fs_1 (at $y^+=-17$). This is because all cases of 8.14 share the

same facesheet geometry. Below fs_1 a clear difference in Reynolds stresses can be observed.

This is highlighted in 8.14 (c), where the effect of the gap between the facesheets and the staggering of the facesheet on the wall-normal velocity fluctuations is evident. The observation of limited wall-normal velocity fluctuations in the x-y planes depicted in Figure 8.12 extends to the Reynolds stresses observed below the wall of the facesheet in 8.14. Particularly, focusing on the wall-normal component of the Reynolds stresses ($\langle\tau_{22}\rangle$), which provides an indication of the mean fluctuations inside the cavities and between the first and second facesheet.

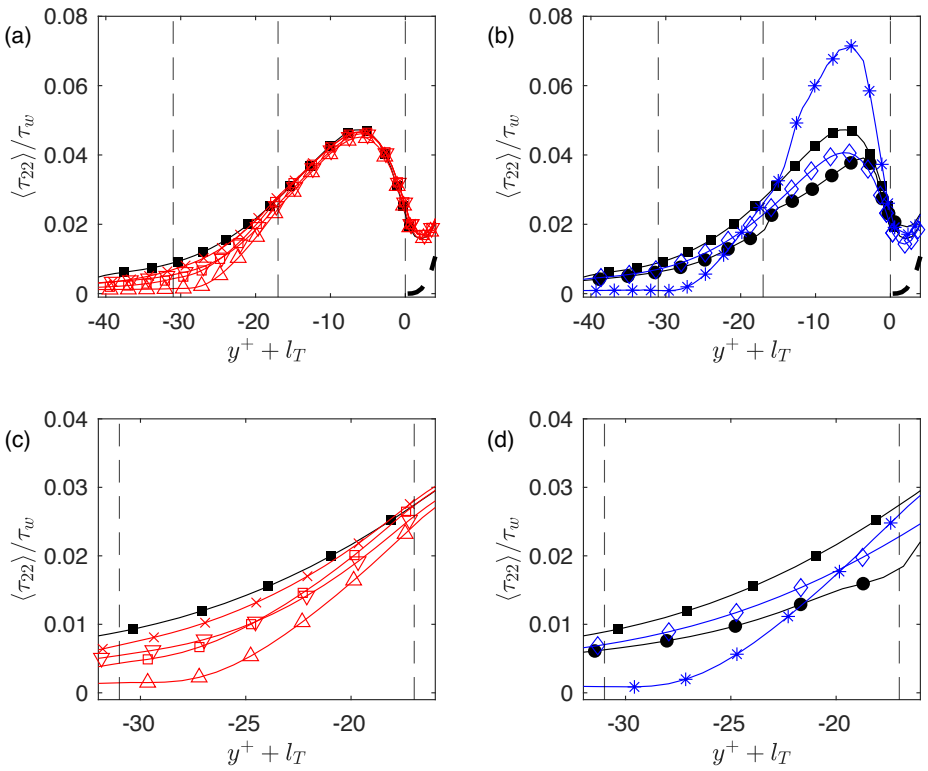

Figure 8.14: Wall normal component of the Reynolds stress, $\langle\tau_{22}\rangle$, Comparison for all runs. (a) and its zoomed-in version,(c), show the thick plate reference case: $L-L14$ (■) and the four straight shifted cases: $D_{50}-L14$ (△), $D_{75}-L14$ (□), $D_{100}-L14$ (×), $D_{50}-L14_{inv}$ (▽). (b) and its zoomed-in version, (d), show both the thick and the thin plate reference cases: $L-L14$ (■) and L_t-L14 (•) as well as both the staggered top facesheet cases: $L-L14_{stag}$ (◇) and $D_{1.6}-L14_{stag}$ (∗). The dashed, horizontal, lines at y+=0, -17 and -31 indicate the beginning of fs_1, the end of fs_1 and the beginning of fs_2 respectively.

Figure 8.15 (a) and (c) show the wall parallel Reynolds stresses ($\langle\tau_{11}\rangle$ and $\langle\tau_{33}\rangle$) in the facesheet gap, for the same cases as in Figure 8.14 (c). In both Figure 8.15 (a) and (c) a peak in wall parallel Reynolds stresses can be observed in the facesheet gap. The figures contain all principal directions of the Reynolds stresses in the facesheet gap and show that the velocity fluctuations are initially confined mainly in the wall-normal direction due to the presence of the orifice, when the facesheet gap is reached, the fluctuations lose this constraint and begin to spread into multiple directions. This shows how all dual facesheet liner cases utilize the gap between the plates to alleviate the restriction on the fluctuating flow direction.

In both Figure 8.15 (a) and (c), it is visible that the decrease in fluctuations in the wall-normal directions results in the increase of fluctuations in the wall-parallel directions. This alleviation is not granted to the thicker facesheet runs and they show clear evidence that the mean fluctuations are in the wall-normal directions throughout the entire facesheet.

Below the first facesheet, there is a noticeable increase in $\langle\tau_{11}\rangle$ and $\langle\tau_{33}\rangle$. Comparing these values for the straight shifted cases in Figure 8.15 (a) and (c) with the wall-normal Reynolds stresses in Figure 8.14 (a) and (c), a relationship between the staggering distance and its effect on the Reynolds stresses becomes apparent. The decrease in $\langle\tau_{22}\rangle$ across the gap is proportional to the shifting distance d^+_{stag} of the plates. Specifically, $\langle\tau_{22}\rangle$ decreases to the lowest value for the 50% open case and the highest for the 100% open case when the second facesheet is reached. Interestingly, the highest maximum value of $\langle\tau_{11}\rangle$ and $\langle\tau_{33}\rangle$

is observed for the 50% open case, while the lowest is seen for the 100% open case. This suggests that greater staggering redirects the flow more into the wall-parallel directions.

The extent to which fluctuations penetrate into the orifices of the second facesheet is also apparent from Figure 8.14 (c). The mean Reynolds stresses beyond the surface of the second facesheet illustrate the extent of this restriction. This observation aligns with the qualitative flow field depicted in Figure 8.12, highlighting the restriction of the flow off the main channel entering the cavity.

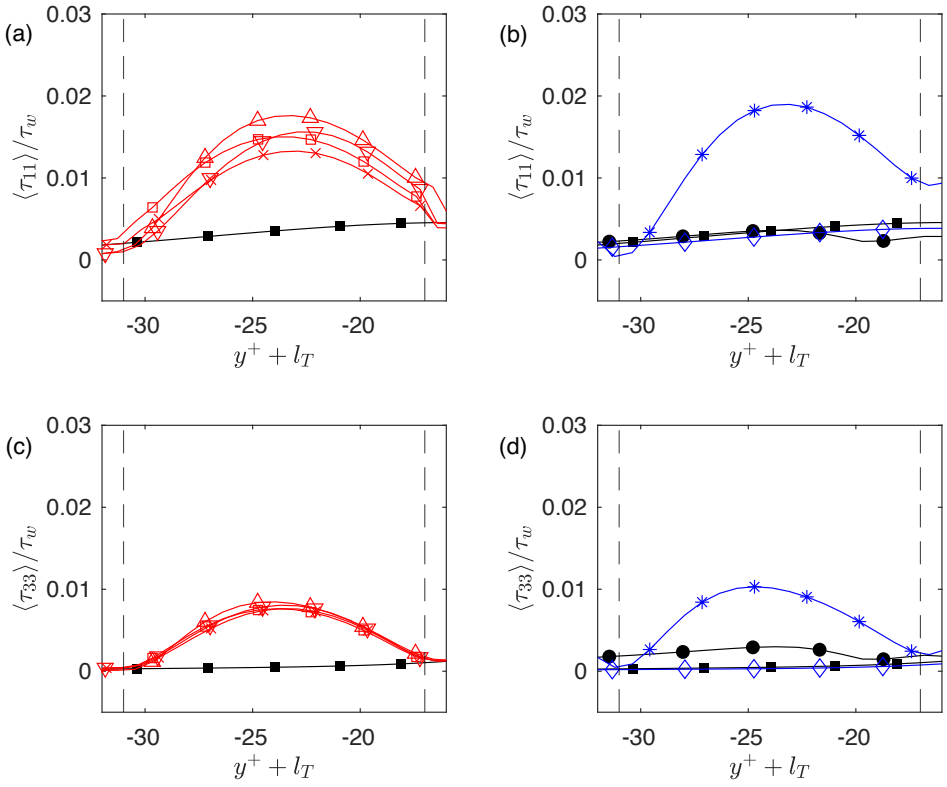

Figure 8.15: Reynolds stress components on the y- normal plane ($\langle\tau_{11}\rangle$ and $\langle\tau_{33}\rangle$) comparison for all runs. (a) and (c) show $\langle\tau_{11}\rangle$ and $\langle\tau_{33}\rangle$ respectively for: $L-L14$ (■) and the four straight shifted cases: $D_{50}-L14$ (△), $D_{75}-L14$ (□), $D_{100}-L14$ (×), $D_{50}-L14_{inv}$ (▽). (b) and its zoomed-in version, (d), show b$\langle\tau_{11}\rangle$ and $\langle\tau_{33}\rangle$ respectively for: $L-L14$ (■) and L_t-L14 (•) as well as both the staggered top facesheet cases: $L-L14_{stag}$ (◇) and $D_{1.6}-L14_{stag}$ (∗). The dashed, horizontal, lines at y+= -17 and -31 indicate the end of fs_1 and the beginning of fs_2 respectively displaying the facesheet gap.

Thin vs thick facesheet

Figure 8.14 (b) shows the wall-normal Reynolds stresses of the L_t-L14 reference case compared to the tick walled reference case and the staggered facesheet cases. The thin facesheet reference case shows lower wall normal Reynolds stresses inside the facesheet when compared to the thick facesheet reference. The orifice orientation of the thin-wall liner, L_t-L14, is identical to that of the thick-wall and all regular facesheet dual facesheet liner cases tested. The only difference lies in the thickness of the plate and the presence of an additional facesheet. Therefore, the thin-wall liner has a configuration very comparable to all the dual facesheet liner cases, as they share the same hole orientation and nearly the same sheet thickness. However, the resulting Reynolds stresses are not very similar. Figure 8.14 (a) and (b) demonstrate that all regular, dual, facesheet liners exhibit $\langle\tau_{22}\rangle$ profiles, inside the first facesheet, much more akin to the thick facesheet reference case than the thin one.

Remarkably, the dual facesheet liner cases display nearly identical behaviour to $L-L14$ for the entirety of fs_1, whereas the thin facesheet has a lower $\langle\tau_{22}\rangle$ peak inside the facesheet. This reveals an intriguing outcome, suggesting that the dual facesheet liner, despite having thinner separate facesheets, demonstrates behaviour more aligned with its total thickness rather than the individual facesheets. Furthermore, the effect of the second liner is observed before it is encountered by the flow. While this could indicate an additional pressure differential over the facesheet, it is challenging to ascertain the exact cause.

Below the staggered facesheet

In the previous section, the focus was on the regular facesheet configuration. From this, some clear conclusions about the effect of the addition of a second facesheet can be drawn. Due to geometric constraints, however, the maximum shifting distance for the regular factsheet results in the 50% open configuration. The staggering of the facesheet allows for a much larger orifice shift in fs_2 such that a 1.6% open configuration can be attained. This, however, does mean that there is a need for an additional reference case, the staggered single facesheet configuration ($L - L14_{stag}$). This section will focus on the Reynolds stresses below the staggered facesheet.

Figure 8.14 (b) shows that the single-facesheet reference case with the staggered facesheet. The geometry exhibits lower wall-normal Reynolds stresses than the thick-wall reference case. In this instance, the lower wall-normal Reynolds stresses also correspond to a lower velocity deficit than the thick-wall reference case (Figure 8.10 (b)). Conversely, the double facesheet configuration ($D_{1.6} - L14_{stag}$) displays a much higher peak $\langle\tau_{22}\rangle$ and a notably higher velocity deficit. However, the thin-wall reference case does not adhere to this trend, as it demonstrates higher velocity deficits than thicker configurations. Despite encountering higher velocity deficits, the peak value of $\langle\tau_{22}\rangle$ below the thin wall is lower than both the staggered cases and the liner reference case. This contradicts what Orlandi and Leonardi (2006) found regarding the relationship of $\langle\tau_{22}\rangle$ with added drag. Apart from the thin-wall reference case, this relationship appears to hold true for all other results.

The influence of the double staggered ($D_{1.6} - L14_{stag}$) configuration on the instantaneous wall-normal velocity is prominently visible in Figure 8.12 (g) and (h). The second facesheet effectively contains the vortex due to the very small effective porosity of this configuration. Figure 8.14 (b) shows the wall-normal Reynolds stresses below the facesheet for both the single and double facesheet configurations, along with the reference cases. The image shows that the $D_{1.6} - L14_{stag}$ configuration leads to significantly higher wall-normal Reynolds stresses within the facesheet itself, indicating that the fluctuations are predominantly contained within the orifice. Consequently, Figure 8.14 (d) shows the zoomed-in version of (b) at the facesheet gap. The figure shows that the mean of the wall-normal Reynolds stresses are reduced to nearly zero at the second facesheet.

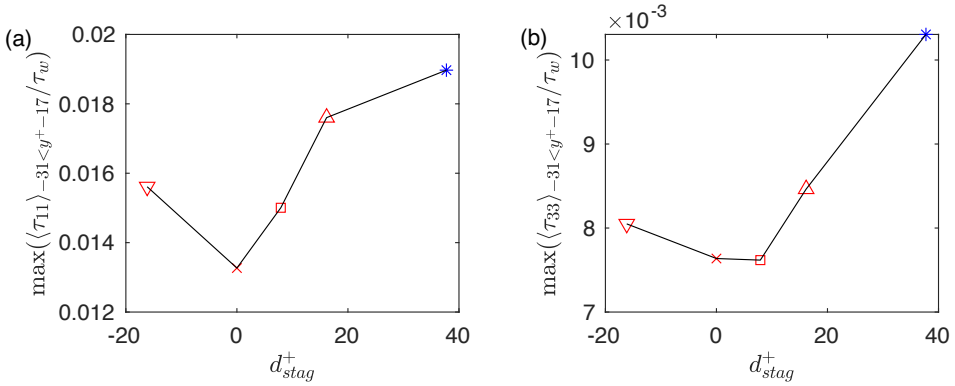

Figure 8.16: Comparison of the maximum value of the wall parallel Reynolds stresses ((a): $\max(\langle\tau_{11}\rangle_{-31<y^+-17})$ and (b): $\max(\langle\tau_{33}\rangle_{-31<y^+-17})$) between the facesheets plotted versus the viscous scaled shifting distance d^+_{stag}. The symbols represent the following cases: $D_{50} - L14$ (△), $D_{75} - L14$ (□), $D_{100} - L14$ (×), $D_{50} - L14_{inv}$ (▽) and $D_{1.6} - L14_{stag}$ (∗).

In Figure 8.15 (b) and (d), $\langle\tau_{11}\rangle$ and $\langle\tau_{33}\rangle$ are shown, respectively, in the facesheet gap for the same cases depicted in Figure 8.14 (d). Both figures (b) and (d) exhibit prominent peaks of wall-parallel Reynolds stresses between the facesheets. Interestingly, the peak of both wall parallel Reynolds stresses is found close to the middle of the gap (at $y^+ = -24$). The staggering of both the top and bottom facesheets has a similar, albeit more pronounced effect on $\langle\tau_{ii}\rangle$ below the facesheet compared to the straight shifted cases. By comparing the peak value in the gap to the single facesheet reference cases the effect of the double facesheet configuration is evident. The results show that the second facesheet is the cause of the wall parallel fluctuations.

Figure 8.16 (a) and (b) illustrate the maximum value of $\langle\tau_{11}\rangle$ and $\langle\tau_{33}\rangle$, respectively, in the facesheet gap. The figures compare the maximum value in the gap for all dual-liner cases. In Figure 8.16 (a), a

monotonic relationship between the staggering distance and the maximum streamwise Reynolds stress in the gap is observed. Although, in Figure 8.16 (b), a less clear relationship with the staggering distance is observed, the peak values of the spanwise Reynolds stresses do show a discernible response. In both directions, generally, the larger the staggering distance, the more the wall-normal fluctuations seem to be converted into wall-parallel fluctuations. From a qualitative perspective, these observations suggest that the mean flow impinges on the second facesheet and is then redirected in the wall-parallel directions, as this is the only relief direction until an orifice in fs_2 is found. Additionally, this suggests that the turbulent kinetic energy in these regions is not necessarily dissipated, but the fluctuations rather adopt a different direction.

Flow in facesheet gap

In order to investigate the findings of the mean velocity fluctuations in the facesheet gap, the following section will address the instantaneous flow in between the facesheets. Figure 8.17 (a) displays the instantaneous streamwise velocity, u_1, while (b) shows the instantaneous spanwise velocity, u_3, in the middle of the facesheet gap at $y^+ = -24$. Both figures visualise the flow magnitude and direction with vectors of the $D_{1.6} - L14_{stag}$ case. The y-position for the plane is chosen as the maximum value for the wall parallel is observed around this height (i.e. the middle of the gap). From (a) and (b) two main occurrences are evident: firstly, flow reversal due to the main channel fluid interaction with the downstream edge of the orifice can be observed. This is similar to what Shahzad et al. (2023) found.

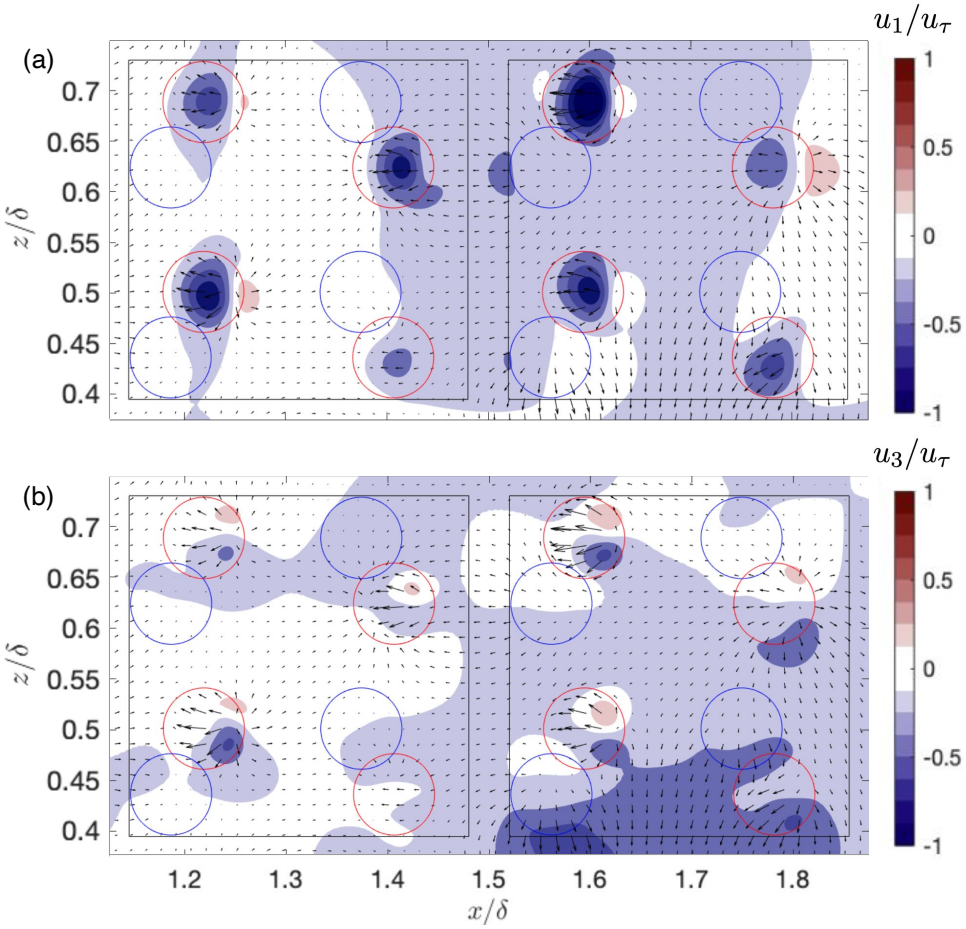

Figure 8.17: (a): Normalized instantaneous streamwise velocity (u_1/u_τ) and (b): Normalized spanwise velocity (u_3/u_τ) shown on an x-z plane in the middle of the facesheet gap, $y^+ = -24$, of $D_{1.6} - L14_{stag}$. Both figures depict the vector field indicating the wall-parallel velocity of magnitude $\|(u_1, u_3)\|_2$ and direction $\langle u_1, u_3 \rangle$. The figure overlays the geometry, where the red geometry represents the orifices in fs_1, the blue geometry represents the orifices in fs_2, and the black geometry indicates the cavity walls. These elements illustrate the location of the respective features, although they are not present at $y^+ = -24$.

Secondly, the redirection of the flow to wall-parallel directions due to the impinging orifice vortex flow on fs_2 similar to van Hout et al. (2018) is observed. Both these observations confirm the quantitative observations made from the Reynolds stresses between the two facesheets.

The reversal of the flow due to the main channel flow impinging on the rear edge of the orifice in fs_1 is most clearly visible in Figure 8.17 (a). With the larger staggering distance of the double-staggered case, the resulting vortex is concentrated in the orifice and gap. The figure illustrates predominantly negative u_1 velocities at the orifice locations, indicating the flow reversal. Consequently, substantial negative velocities between the facesheets are observed, although instances of positive velocities are also observed, resulting in a flow directed towards an orifice in fs_2.

The observations of van Hout et al. (2018) for impinging flow on a flat surface are consistent with both flow directions. As the principal rotation axis of the orifice vortex is in the z-normal direction (due to the mean flow in the x-direction) the resulting velocity of the impinging flow is primarily negative for u_1. However, for u_3, the flow splits more evenly into both positive and negative velocities, as there is no principal velocity in the z-direction to maintain. The fluid direction is a consequence of the interaction with fs_2 and the wall-normal flow, not of spanwise turbulent fluctuations from the main channel. Consequently, the wall-normal flow impinges on fs_2 and splits into both positive and negative velocities of u_3. The vectors at these locations effectively depict the flow emanating from the impinging location.

Both figures show that there is fluid flow in between the facesheet for the $D_{1.6} - L14_{stag}$ case. While each

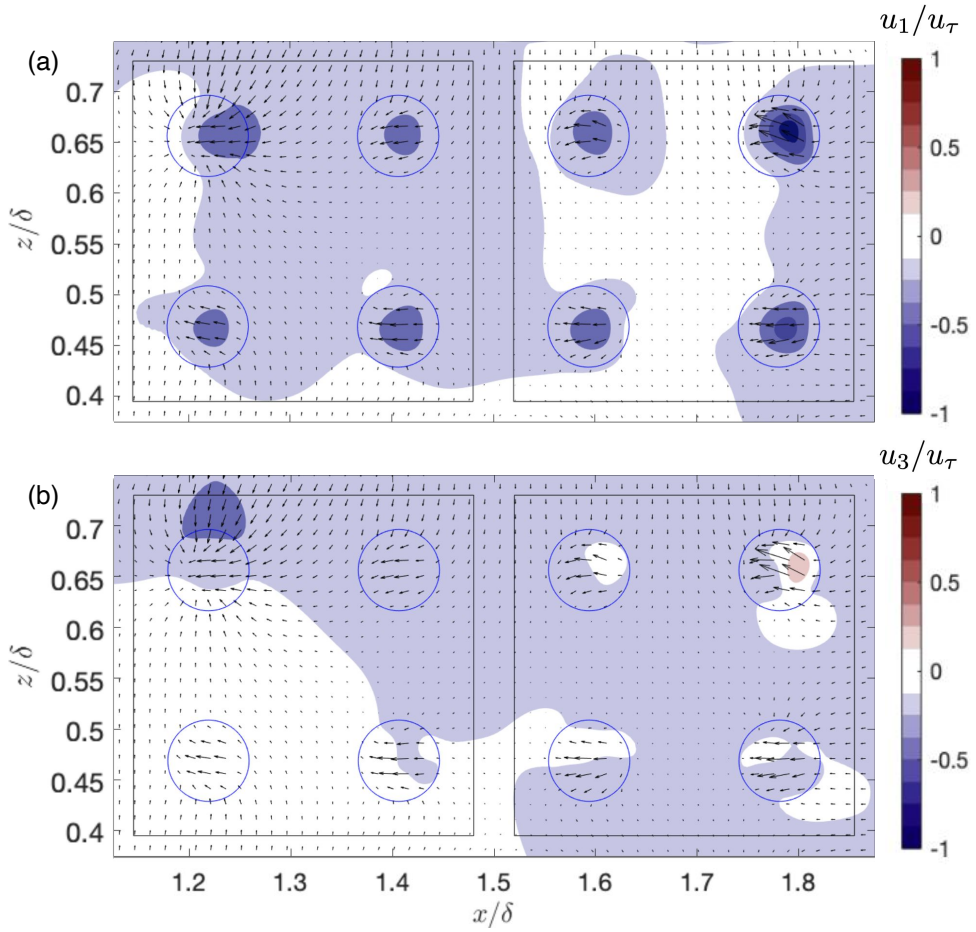

Figure 8.18: (a): Normalized instantaneous streamwise velocity (u_1/u_τ) and (b): Normalized spanwise velocity (u_3/u_τ) shown on an x-z plane in the middle of the facesheet gap, $y^+ = -24$, of $D_{100} - L14$. Both figures depict the vector field indicating the wall-parallel velocity of magnitude $\|(u_1, u_3)\|_2$ and direction $\langle u_1, u_3 \rangle$. The figure overlays the geometry on the flow fields. The orifices in fs_1 and fs_2 are shown by the blue orifices (as they overlap) and the black geometry indicates the cavity walls. These elements illustrate the location of the respective features, although they are not present at $y^+ = -24$.

orifice in fs_1 has a corresponding orifice in fs_2 fluid flow does not seem to maintain the adjacent orifice as a destination. The flow rather heads to orifices in different cavities in both streamwise and spanwise directions. As Figure 8.16 indicates, the staggering distance has an enlarging effect on the fluctuations between the facesheets.

In Figure 8.18, the streamwise velocity (a) and the spanwise velocity (b) of the $D_{100} - L14$ case in the middle of the facesheet gap are depicted. Similar to Figure 8.17, the vectors indicate the wall parallel direction of the flow. A comparison between Figure 8.17 and Figure 8.18 reveals several regions with differences in velocity magnitude. Particularly near the orifice, the streamwise velocity is generally lower for $D_{100} - L14$ compared to $D_{1.6} - L14_{stag}$. Similarly, Figure 8.18 (b) illustrates that there is less flow interaction with the second facesheet, as the orifice in fs_2 is directly below that in fs_1. Consequently, there is minimal flow impinging on the bottom facesheet, leading to reduced wall parallel velocity fluctuations between the plates.

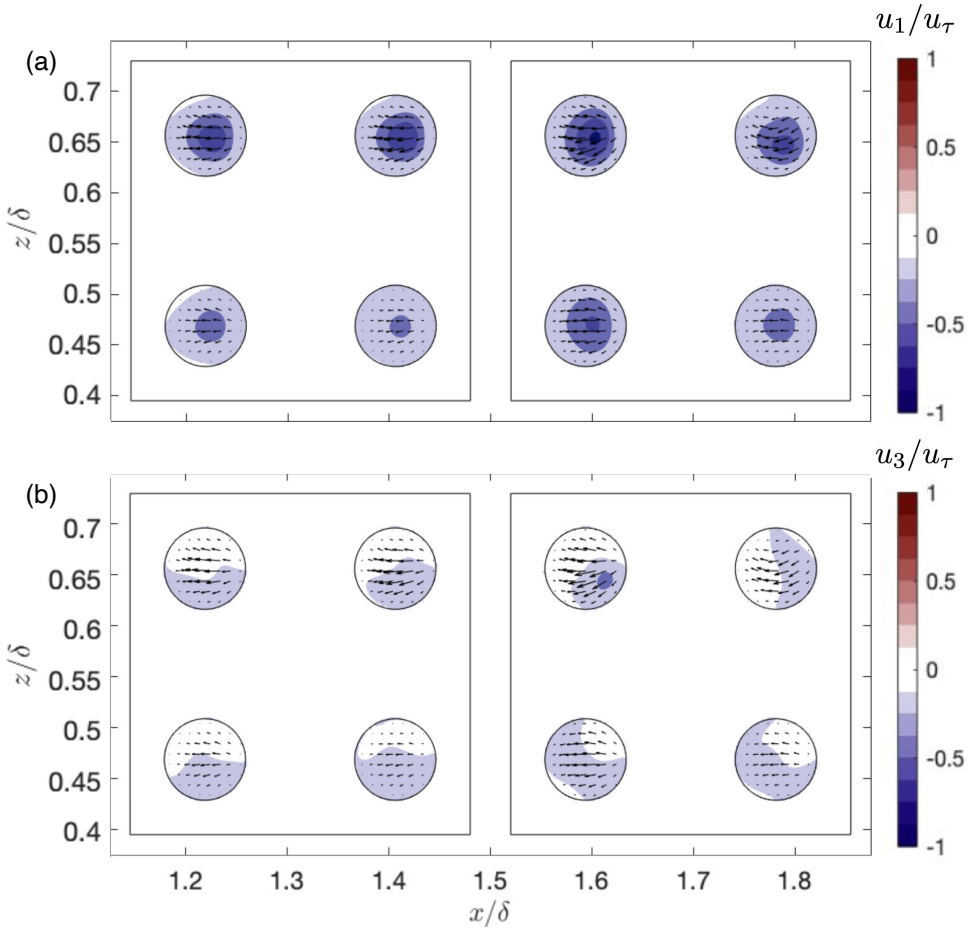

Figure 8.19: Normalized instantaneous streamwise velocity (u_1/u_τ) and (b): spanwise velocity (u_3/u_τ) shown on an x-z plane at $y^+ = -24$ for the single facesheet $L - L14$ case. Both figures depict the vector field indicating the wall-parallel velocity of magnitude $\|(u_1, u_3)\|_2$ and direction $\langle u_1, u_3 \rangle$. The black circles indicate the orifices in the thick facesheet and the black squares show the location of the cavity walls below the facesheet (i.e. $y^+ < -40$).

While the difference in staggering distances between the cases noticeably affects the vortex in the orifice and the flow impingement on fs_2, both dual facesheet liner geometries exhibit flow between the facesheets. As a reference, Figure 8.19 displays the instantaneous streamwise velocity (a) and spanwise velocity (b) for $L - L14$, on the same height x-z plane as Figure 8.17 and Figure 8.18. This figure displays the flow velocity within the facesheet of $L - L14$, which has a single, thick facesheet. In $L - L14$, the only fluid volume present from $0 \geq y^+ \geq -40$ is found in the orifices, emphasizing that the wall parallel velocity within the facesheet is concentrated in fluctuating flow within the orifices.

Figure 8.20 illustrates the instantaneous normalised streamwise velocity on an x-y plane within the

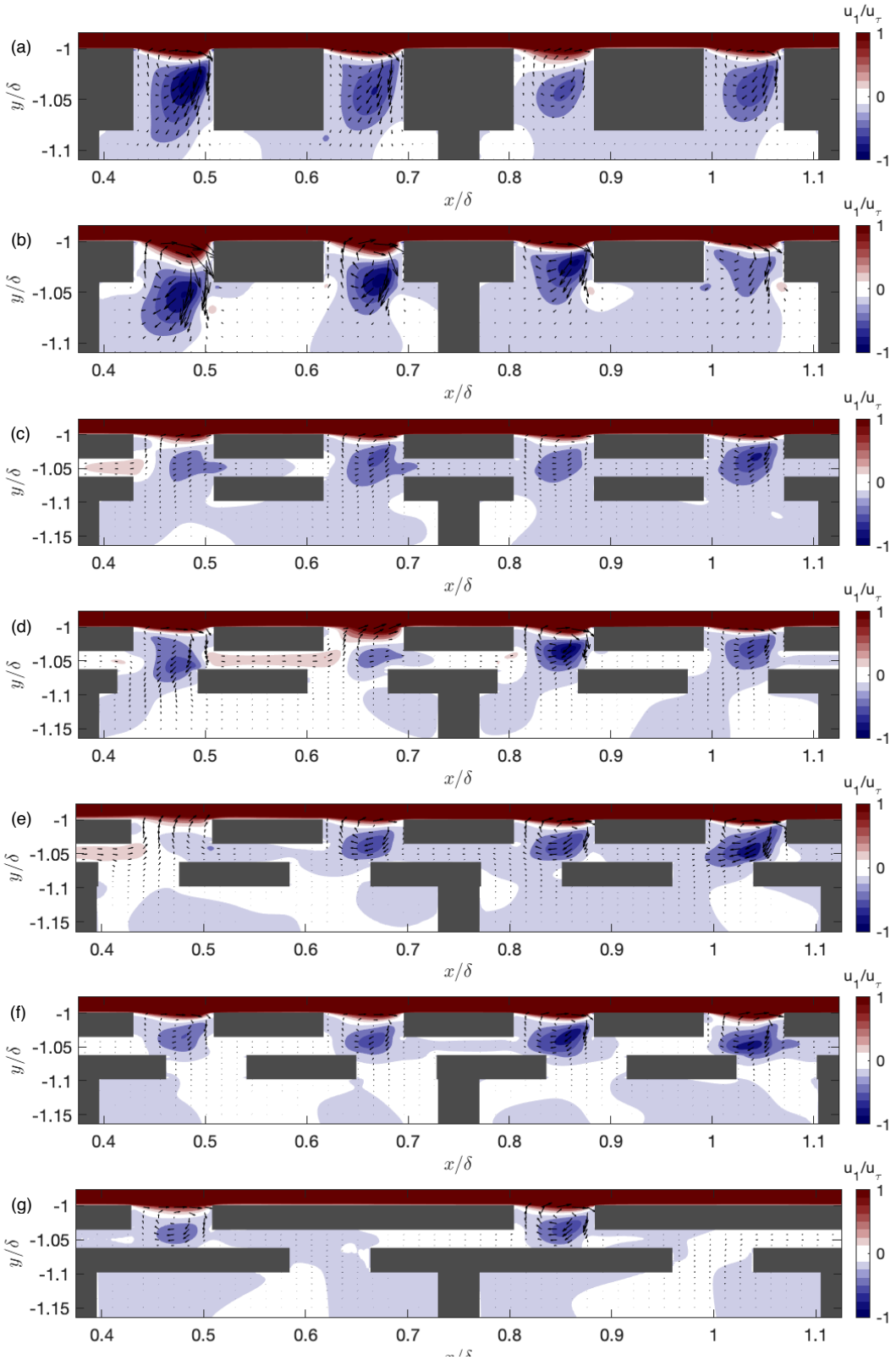

Figure 8.20: Normalised streamwise velocity in an x-y plane through the orifice and cavity. The figures show vectors of magnitude $\|(u_1, u_2)\|_2$ and direction $\langle u_1, u_2 \rangle$. The display is of the bottom wall of the domain, where the wall is at $y/\delta = -1$. The cases presented are (a): $L - L14$, (b): $L_t - L14$, (c): $D_{100} - L14$, (d): $D_{75} - L14$, (e): $D_{50} - L14$, (f): $D_{50} - L14_{inv}$ and (g): $D_{1.6} - L14_{stag}$. The liner walls are indicated in grey.

orifices and facesheet gap. The figure includes vectors of $\langle u_1, u_2 \rangle$ to indicate the flow direction on the x-y plane. It encompasses all cases considered in the present work alongside the thick and thin facesheet reference cases. The vectors within the orifices depict how the flow within them forms a vortex-like structure on the x-y plane.

A comparison between 8.20 (a) and (b) reveals the behaviour of the orifice vortex in the thick facesheet configuration. It impinges on the upstream wall of the orifice, causing part of the flow to split towards the cavity, while the remainder continues upwards within the orifice. In contrast, due to the thinner facesheet in (b), this effect is less pronounced, resulting in more fluid flowing directly into the cavity below the facesheet.

Figure 8.20 (c) presents the streamwise velocity in the double facesheet liner of $D_{100} - L14$. Notably, the double facesheet liners share a similar single facesheet thickness as $L_t - L14$. Consequently, similar effects can be observed for the double facesheet geometries. However, in the case of the double facesheet liners, the flow below fs_1 does not directly penetrate into the cavity. Instead, the flow travels between the facesheets, influencing the fluid flow in the adjacent orifice and eventually either flowing into the cavity or towards the channel.

Figure 8.20 (d) and (e) depict the x-y plane of the streamwise velocity and the interaction of the flow with the facesheet for $D_{75} - L14$ and $D_{50} - L14$ respectively. These figures illustrate the wall-parallel velocity between the plates, primarily negative due to the direction of the vortex in the orifice. However, some positive velocity is observed between the plates. When encountering positive velocity, it strongly interacts with the flow in the fs_1 orifice, leading to the breakup of the vortex and a net mass outflow through the orifice facilitated by fluid originating from the cavity. Nonetheless, this does not result in a net mass outflow out of the entire cavity, as such a phenomenon is known to substantially reduce drag (O'Connor et al. (2023)), which is not observed in this work.

Figure 8.20 (f) depicts the $D_{50} - L14_{inv}$ case, showcasing the streamwise shifted fs_2. This figure illustrates how the shift of the fs_2 orifice towards the downstream edge of the fs_1 orifice accommodates the wall-normal fluctuations by the orifice in fs_2. The fluid originating from the downstream edge of fs_1 flows towards the cavities unimpeded by the facesheet. Moreover, the upstream edge of the orifice in fs_2, to a lesser extent, exhibits the same flow-splitting effect of the impinging vortex on the upstream wall, as seen for $L - L14$. This appears to funnel fluid into the cavity, somewhat preventing it from flowing in between the facesheet. This effect is especially noticeable when compared to Figure 8.20 (e).

The streamwise velocity for the double staggered configuration ($D_{1.6} - L14_{stag}$) is presented in Figure 8.20 (g). This figure differs from the previous geometries as the x-y plane only shows one orifice, owing to the staggering of the orifices in both facesheets. Due to the different geometry, the vortex in the orifice finds a facesheet below nearly the entire orifice, a characteristic not experienced by any other geometry in this manner. Consequently, the vortex appears nearly fully contained in the orifice, and the streamwise flow towards the downstream orifice in fs_2 is limited. However, Figure 8.17 demonstrates that the spanwise flow due to the impinging flow on fs_2 plays a larger role in determining the fluid release direction. In this case, the spanwise fluctuations are more prevalent due to the geometry's increased spanwise variations compared to all other cases considered.

After comparing wall parallel flow below $y^+ = 0$ between single and dual facesheet liner geometries, along with observations from the Reynolds stresses in the facesheet gap, it becomes evident that wall-normal permeability alone may not fully characterize the permeability of dual facesheet liners. While for a single facesheet, the wall-normal permeability has been shown to be an effective scaling parameter by Shahzad et al. (2023), the present work has shown that this does not extend to double facesheet liners. Although lower values for the Forchheimer coefficients have been attained by increasing the normal pressure drop over the facesheet, they did not reveal the added drag reduction expected based on the values of the Forchheimer coefficients. Moreover, the deviation of the velocity deficit from the reference case increases with increasing staggering distance. Especially for $D_{1.6} - L14_{stag}$, the $1/\alpha_y^+$ is very low, and ΔU^+ is the highest of all dual facesheet cases.

Due to the shifting of the facesheet, the wall-normal velocity in the facesheet behaves differently from that of the reference cases used in this work. Although the wall-normal fluctuations in fs_1 are very similar to those found in the thick facesheet reference case. The shifting of the facesheet causes a very large reduction of the wall-normal fluctuations through the second facesheet orifices. This reduces the inertial effects in the orifices to nearly zero as these scale with the pore Reynolds number. Although for a high enough pore Reynolds number, the Darcy permeability is not significant (Figure 5.1), for lower

values, only the Darcy permeability is of interest. The Darcy permeability scaling however does not show a monotonic relation with added drag in the work of Shahzad et al. (2023), therefore additional research is needed to investigate the effect of the wall parallel permeabilities and the reduction of inertial effects inside the facesheet on liner drag.

Moreover, the shifting of the second facesheet reveals an opposite response to what was expected for ΔU^+ vs $1/\alpha_y^+$. The further the shift of the facesheet, the lower the values for the wall-normal element of the inversed Forchheimer coefficient, indicating a lower permeability. The space between the liners, however, effectively increases the permeability of the facesheet where a further shift means more wall parallel flow between fs_1 and fs_2. Additionally, an indication of this has been given by the higher values of the Darcy permeability for the dual facesheet cases in this work.

The computation of the Darcy and Forchheimer coefficients might be a cause of this effect. The method used by Shahzad et al. (2023) is tailored to wall normal permeability only, not taking wall parallel permeability into account. In this work however, the effective geometry change from a normal flow to a grazing flow is more profound as there is permeability in the stream and spanwise direction rather than only in the wall-normal direction, as is the case for a single facesheet liner configuration. Therefore, the wall parallel permeability needs to be accounted for in future works, rather than only the wall-normal direction.

8.3.1 Relevant parameters for Reynolds stresses

The previous discussion has indicated that there is a monotonic relation between d^+_{stag} and both the velocity deficit and the Reynolds stresses. This however is limited to regular facesheet liner geometries. Both the velocity deficit and the wall-normal velocity fluctuations responded similarly to the increase of d^+_{stag}, where the larger d^+_{stag}, the smaller the velocity deficit and the larger the decrease of wall-normal velocity fluctuations in the facesheet.

In order to have a better impression of the reduction of the wall-normal fluctuations, Figure 8.21 is employed. In 8.21 (a), the percentage reduction of $\langle\tau_{22}\rangle$ over the facesheet gap is shown. Here it is visible that the misalignment of the facesheet orifices reduces the wall-normal fluctuations entering the facesheet gap. The farthest staggering ($D_{1.6} - L14_{stag}$) reduces 96% of all wall-normal velocity fluctuations. The percentage decrease of $\langle\tau_{22}\rangle$ over the gap is nearly identical in distribution as Figure 8.16 reiterating the redirection of fluctuations in the wall parallel directions when the second facesheet is reached.

Figure 8.21 (b) shows the value of $\langle\tau_{22}\rangle$ at $y^+ = -40$, i.e the end of the facesheet of $L - L14$. All cases are considered in the figure and therefore an effective comparison can be made. All double facesheet liner

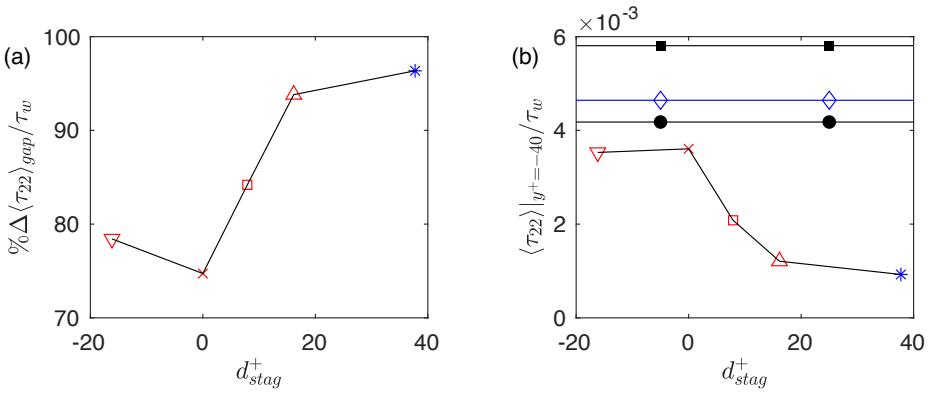

Figure 8.21: Percenntual decrease of the Wall normal Reynolds stresses over the facesheet gap ($\%\Delta\langle\tau_{22}\rangle_{gap}/\tau_w$) compared to the staggering distance (d^+_{stag}) displayed in (a) and the value of $\langle\tau_{22}\rangle$ found at y+=-40, i.e. the bottom of the L-L14 facesheet, in (b). The different liner cases are indicated by coloured symbols as: $L - L14$ (■), $L_t - L14$ (•), $L - L14_{stag}$ (◇), $D_{50} - L14$ (△), $D_{75} - L14$ (□), $D_{100} - L14$ (×), $D_{50} - L14_{inv}$ (▽), $D_{1.6} - L14_{stag}$ (∗). Note that for (b) the single facesheet liner cases are included as lines to provide a comparison, they do not have a staggering distance as they only have a single facesheet in the geometry.

cases are seen to reduce $\langle\tau_{22}\rangle$ compared to all the single facesheet liners. Indicating that the application of a second facesheet is an effective manner to reduce the momentum transfer between the channel and the cavities as the wall-normal fluctuations are inhibited in the facesheet.

As the previously described figures have shown, the staggering distance is a relevant length scale, for double facesheet liners, which can be increased to reduce wall normal fluctuations in the facesheet. The question remains, however, what effect this proves to have on the liner drag. In order to investigate this, Figure 8.22 (a) is employed. Here the percentage decrease of $\langle\tau_{22}\rangle$ over the facesheet gap is compared to the corresponding velocity deficit. The regular facesheet cases show that the larger the reduction of the wall-normal velocity fluctuations through the facesheet, the smaller the velocity deficit. This result remains in line with Orlandi and Leonardi (2006) where the observation of reduced wall-normal velocity fluctuations do result in a lower velocity deficit. Again, the velocity deficit for the double staggered case does not follow this pattern. It would be interesting to see where different other percentage open configurations with the staggered facesheet would be positioned in this figure. This way a conclusion could be drawn on whether there is an optimal value for the staggering, (i.e. around 50 %) or that the double staggered configuration does not present as favourable results as was anticipated, based on the minimal percentage open area and its facesheet.

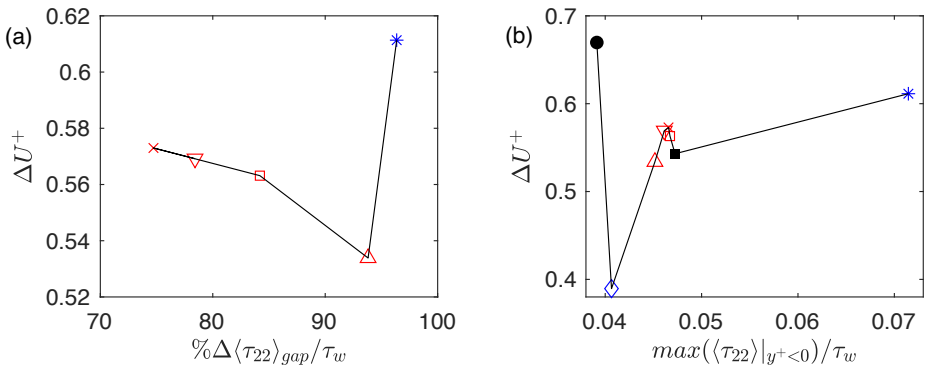

Figure 8.22: (a): ΔU^+ vs Percenntual decrease of the Wall normal Reynolds stresses over the facesheet gap ($\%\Delta\langle\tau_{22}\rangle_{gap}/\tau_w$) (b): ΔU^+ vs max($\langle\tau_{22}\rangle$) for $y^+ < 0$. The different liner cases are indicated by coloured symbols as: $L - L14$ (■), $L_t - L14$ (●), $L - L14_{stag}$ (◇), $D_{50} - L14$ (△), $D_{75} - L14$ (□), $D_{100} - L14$ (×), $D_{50} - L14_{inv}$ (▽), $D_{1.6} - L14_{stag}$ (∗).

Figure 8.22 (b) shows the relation of the maximum value of the wall-normal RMS of the velocity with the velocity deficit. Figure 8.22 (b) shows, no apparent correlation between the quantities and therefore the relation of the maximum wall normal fluctuations below the wall and the velocity deficit is not existent. Therefore the maximum value of $\langle\tau_{22}\rangle$ is not the ideal performance metric of the liner to pursue reduction in.

9

Conclusion and Recommendations

Throughout this thesis, the impact of adding an extra facesheet on the aerodynamics of an acoustic liner has been thoroughly examined. This investigation was carried out by conducting pore-resolved DNS simulations over perforated plates. The simulations have added to the only limited knowledge base of turbulent flows over porous surfaces especially when resembling acoustic liner applications in jet engines. Additionally, some concepts in literature have been leveraged and tested in an attempt to attain favourable aerodynamic characteristics in the liner.

When the results are coupled back to the rationale behind the design, an evaluation of how well the expectations have been fulfilled and to what extent uncertainties still exist can be performed. This will initially be done by the evaluation of the posed research questions:

Research Question: What is the effect of an additional facesheet on acoustic liner aerodynamics?

Sub-questions:

1. What is the effect of an additional facesheet on the added liner drag?
2. How does a double facesheet affect the wall-normal velocity fluctuations and interaction between the flow below and above the facesheet?
3. What are the relevant scaling parameters for the performance indication of the dual facesheet liners?

The examination of the additional facesheet's impact on liner drag reveals several key findings. As anticipated, all tested liner configurations exhibit an increase in drag compared to the smooth wall configuration. However, a correlation emerges between the velocity deficit and the shifting distance of the second facesheet. Specifically, an increase in shifting distance leads to a reduction in added drag for the regular, dual, facesheet liner configurations. Notably, all cases in this study demonstrate a smaller velocity deficit than the thin plate reference case. This suggests that the second facesheet does impact drag, providing a reduction compared to a single thin facesheet. The thick-wall reference case exhibits less added drag than a dual-facesheet liner with minimal staggering, applying a sufficient staggering distance to the second facesheet results in an observed reduction in added drag.

The relative differences observed between the runs are minor. Above the facesheet, little to no discernible variation can be identified between the single and dual facesheet liner cases. The differences in drag variation between the most and least favourable cases are less than 4%, suggesting that for an effective investigation of the effects of a dual facesheet liner configuration on the flow above the facesheet, higher friction Reynolds number DNS runs are required.

However, the effect of a second facesheet on the Reynolds stresses is more pronounced. Instantaneous velocity fluctuations provide a clear illustration of the staggering distance's impact on inhibiting wall-normal fluctuations attempting to penetrate into the cavities below the facesheet. The effect of the direction of staggering has become evident, with downstream staggering accommodating wall-normal fluctuations into the second facesheet orifice, while upstream staggering inhibits this phenomenon. This effectively restricts the flow into the cavities while maintaining the desired sound attenuation properties.

A similar effect is observed in the wall-normal Reynolds stresses below the wall. Negative streamwise shifting of the plates impedes the entry of wall-normal fluctuations into the cavity. The second facesheet

constrains this phenomenon, diverting turbulent fluctuations predominantly into wall-parallel directions. Moreover, greater misalignment between the orifices of the top and bottom facesheets leads to a more significant reduction of wall-normal Reynolds stresses, approaching their minimum value, across the facesheet gap.

After conducting a comprehensive comparison of wall parallel flow below $y^+ = 0$ in both single and dual facesheet liner configurations, combined with the wall parallel Reynolds stresses in the facesheet gap, it is apparent that wall-normal permeability alone may not provide a complete characterization of a dual facesheet liners' permeability. While previous studies have demonstrated the effectiveness of wall-normal permeability as a scaling parameter for single facesheet configurations, the findings in this work suggest that this may not extend to dual facesheet liners.

Although for similar $1/\alpha_y^+$ values to the reference case, similar values of ΔU^+ were found in the present work. The opposite of a monotonically *increasing* trend vs $1/\alpha_y^+$ was found. Despite achieving lower values for the Forchheimer coefficients through increased normal pressure drop over the facesheet, the anticipated reduction in added drag was not observed in line with the expected response to $1/\alpha_y^+$. For increasing staggering distance, a lower value for $1/\alpha_y^+$ was found while this showed higher values for the cases' velocity deficit. These discrepancies indicate the presence of additional factors influencing added drag beyond what can be solely accounted for by variations in wall-normal permeability. The larger discrepancy for larger staggering distances suggests the influence of wall parallel permeabilities should be accounted for.

When considering relevant scaling parameters for the double facesheet liner, two main factors emerge as significant. Firstly, the staggering distance of the plates exhibits a clear correlation with the added drag of the plates. While this parameter may not fully capture the behaviour of single facesheet geometries, it proves informative for dual facesheet designs. Similar to the orifice radius or the single plate porosity, the staggering distance of the second facesheet emerges as a relevant parameter for scaling with the added drag of the liner. Secondly, the percentage reduction of the wall-normal Reynolds stresses across the facesheet gap also stands out. Although this reduction is a consequence of the staggering distance of the plates, this variable, akin to the jet-like flow into the cavities, serves as an indicator of added drag on the plates. Greater reductions in wall-normal Reynolds stresses over the facesheet gap correspond to smaller velocity deficits in the configuration.

The relation of the velocity deficit for $D_{1.6}-L14_{stag}$ with both the staggering distance and the wall-normal Reynolds stress reduction over the facesheet gap does not align with the regular facesheet configurations. This raises questions regarding the correspondence between wall-normal fluctuations, pressure over the facesheet and drag, suggesting that additional factors may influence the overall drag behaviour of the acoustic liner configurations studied. Furthermore, it is noteworthy to consider whether grazing flow results in similar pressure drop behaviour over two plates as normal impinging flow does. This is as differences between configurations such as $D_{50} - L14$ and $D_{50} - L14_{inv}$ indicate that the pressure drop for normal flow impinging on a surface cannot be directly extrapolated to grazing flow situations.

Recommendations

This thesis represents a preliminary exploration into the aerodynamics of double facesheet liner configurations. While hypotheses have been formulated based on prior works on similar geometries or topics, the selection of hypotheses was not specifically tailored to this unique geometry. Nonetheless, this initial investigation provides an understanding, albeit limited, of the aerodynamic effects of adding an extra liner. Despite the limited impact observed, further investigation into this area is warranted, as the concept holds promise for potential added drag reduction under certain conditions. Moreover, this study has raised some new questions regarding the behaviour of the double staggered configuration, as well as the behaviour of pressure drop over staggered plates under grazing flow conditions compared to normal flow and the influence of streamwise permeability on drag. For future research, the following recommendations are proposed:

The first recommendation is to include additional double staggered liner cases with more moderate staggering distances. This would help clarify the effect of double staggering and address any doubts arising from the current results. By fulfilling this recommendation, the added drag increase of the double staggered configuration could be contextualized better, potentially revealing whether different behaviour exists among double facesheet staggered configurations or if there exists an optimal staggering distance for the second facesheet.

Secondly, it is recommended to conduct additional tests under higher friction Reynolds numbers or for higher facesheet porosities. While the latter may present geometric challenges regarding plate staggering, it could lead to more pronounced relative differences. This would offer clearer insights into the effects of the plates and establish a more evident relationship between staggering distance, inhibition of wall-normal velocity fluctuations, and added drag.

Moreover, to verify the relevance of pressure drop over the plates as a scaling parameter for the velocity deficit, the direction of flow should be considered when defining the pressure drop over the facesheet. This ensures the pressure drop's relevance and could serve as an appropriate measure for defining a low added drag configuration, particularly for grazing flow conditions. Such a study would allow for the evaluation and comparison of the effect of the additional facesheet on skin friction.

Additionally, due to the observation of wall parallel flow between the plates, the limitation of the permeability coefficients to the wall-normal direction is not suitable. Further research into the effect of wall parallel permeabilities in liners can provide additional insights into these phenomena. Having a permeability coefficient which captures the permeability of the entire facesheet in multiple directions might provide better scaling parameters for the relation of added drag to a liner length scale.

Lastly, expanding the parameter space is recommended. This could involve reducing the gap width while ensuring it remains sufficient for the desired sound attenuation levels. Additionally, introducing geometric variations such as a third facesheet or shifting the holes in the spanwise directions could offer further insights into the aerodynamic behaviour of double facesheet liner configurations.

References

Amir, M., & Castro, I. (2011, 08). Turbulence in rough-wall boundary layers: Universality issues. *Experiments in Fluids*, *51*, 313-326. doi: 10.1007/s00348-011-1049-7

ANSI. (2014). *Acoustical terminology.* Archived from the original (PDF) on 2023-10-11. (Retrieved 2023-10-11)

Bae, Y., & Kim, Y.-I. (2016). Numerical modeling of anisotropic drag for a perforated plate with cylindrical holes. *Chemical Engineering Science*, *149*, 78–87. Retrieved from https://doi.org/10.1016/j.ces.2016.04.036 doi: 10.1016/j.ces.2016.04.036

Bake, F., & Knobloch, K. (2019, March). Novel liner concepts. *CEAS Aeronautical Journal*, 123–136. doi: 10.1007/s13272-019-00380-7

Bechert, D. W., Bruse, M., Hage, W., Van der Hoeven, J. G. T., & Hoppe, G. (1997). Experiments on drag-reducing surfaces and their optimization with an adjustable geometry. *Journal of Fluid Mechanics*, *338*, 59–87. doi: 10.1017/S0022112096004673

Beck, B., Schiller, N., & Jones, M. (2015, June). Impedance assessment of a dual-resonance acoustic liner. *Applied Acoustics Journal*, *93*, 15–22. doi: 10.1016/j.apacoust.2015.01.011

Bernardini, M., Modesti, D., Salvadore, F., & Pirozzoli, S. (2021). Streams: A high-fidelity accelerated solver for direct numerical simulation of compressible turbulent flows. *Computer Physics Communications*, *263*, 107906. Retrieved from https://www.sciencedirect.com/science/article/pii/S0010465521000473 doi: https://doi.org/10.1016/j.cpc.2021.107906

Bielak, G. W., Premo, J. W., & Hersh, A. S. (1999). *Advanced turbofan duct liner concepts* (Tech. Rep.). NASA CR 209002.

Bozak, R. F., Jones, M. G., Howerton, B. M., et al. (2019). Effect of grazing flow on grooved over-the-rotor acoustic casing treatments. In *Proceedings of the 25th aiaa/ceas aeroacoustics conference.* Delft.

Breugem, W. P., Boersma, B. J., & Uittenbogaard, R. E. (2006). The influence of wall permeability on turbulent channel flow. *Journal of Fluid Mechanics*, *562*, 35–72. doi: 10.1017/S0022112006000887

Casalino, D., Hazir, A., & Mann, A. (2018). Turbofan broadband noise prediction using the lattice boltzmann method. *AIAA Journal*, *56*(2), 609–628.

Castro, I. (2007, 08). Rough-wall boundary layers: Mean flow universality. *Journal of Fluid Mechanics*, *585*, 469 - 485. doi: 10.1017/S0022112007006921

Chan, L., MacDonald, M., Chung, D., Hutchins, N., & Ooi, A. (2015, 05). A systematic investigation of roughness height and wavelength in turbulent pipe flow in the transitionally rough regime. *Journal of Fluid Mechanics*, *771*, 743-777. doi: 10.1017/jfm.2015.172

Chan, L., MacDonald, M., Chung, D., Hutchins, N., & Ooi, A. (2018). Secondary motion in turbulent pipe flow with three-dimensional roughness. *Journal of Fluid Mechanics*, *854*, 5–33. doi: 10.1017/jfm.2018.570

Chan-Braun, C., García-Villalba, M., & Uhlmann, M. (2011). Force and torque acting on particles in a transitionally rough open-channel flow. *Journal of Fluid Mechanics*, *684*, 441–474. doi: 10.1017/jfm.2011.311

Chen, K., Chen, Y., Lin, K., & Weng, C. (1998). The improvement on the transmission loss of a duct by adding helmholtz resonators. *Applied Acoustics*, *54*(1), 71-82. Retrieved from https://www.sciencedirect.com/science/article/pii/S0003682X97000364 doi: https://doi.org/10.1016/S0003-682X(97)00036-4

Cheng, H., & Castro, I. (2002, 01). Near wall flow over urban-like roughness. *Boundary-Layer Meteorology*, *104*, 229-259. doi: 10.1023/A:1016060103448

Cherrier, O., Pommier-Budinger, V., & Simon, F. (2012). Panel of resonators with variable resonance frequency for noise control. *Appl Acoustics*, *73*, 781-790.

Chung, D., Chan, L., MacDonald, M., Hutchins, N., & Ooi, A. (2015). A fast direct numerical simulation method for characterising hydraulic roughness. *Journal of Fluid Mechanics*, *773*, 418–431. doi: 10.1017/jfm.2015.230

Chung, D., Hutchins, N., Schultz, M., & Flack, K. (2021, 01). Predicting the drag of rough surfaces. *Annual Review of Fluid Mechanics*, *53*, 439-471. doi: 10.1146/annurev-fluid-062520-115127

Clauser, F. H. (1954). Turbulent boundary layers in adverse pressure gradients. *Journal of the Aeronautical Sciences*, *21*(2), 91-108. Retrieved from https://doi.org/10.2514/8.2938 doi: 10.2514/8.2938

Coceal, O., Dobre, A., Thomas, T. G., & Belcher, S. E. (2007). Structure of turbulent flow over regular arrays of cubical roughness. *Journal of Fluid Mechanics*, *589*, 375–409. doi: 10.1017/S002211200700794X

Colebrook, C. F. (1939). Turbulent flow in pipes, with particular reference to the transitional region between smooth and rough wall laws. *J. Inst Civ.Eng.*, 133-156.

Dai, X., & Aurégan, Y. (2018). A cavity-by-cavity description of the aeroacoustic instability over a liner with a grazing flow. *Journal of Fluid Mechanics*. doi: 10.1017/jfm.2018.542

de Bedout, J. M., Franchek, M. A., Bernhard, R. J., et al. (1997). Adaptive-passive noise control with self-tuning helmholtz resonators. *J Sound Vib*, *202*, 109-123.

de Segura, G., & García-Mayoral. (2019). Numerical studies of turbulent drag reduction over anisotropic porous media with high streamwise permeability. *Journal of Fluid Mechanics*. doi: 10.1017/jfm.2019.100

de Segura, G. G., & García-Mayoral, R. (2020). Imposing virtual origins on the velocity components in direct numerical simulations. *International Journal of Heat and Fluid Flow*, *86*, 108675. Retrieved from https://www.sciencedirect.com/science/article/pii/S0142727X20303027 doi: https://doi.org/10.1016/j.ijheatfluidflow.2020.108675

Dodge, C., Howerton, B. M., & Jones, M. G. (2023). Effects of layer spacing for a multilayered facesheet acoustic liner. In *Aiaa aviation 2023 forum*. Retrieved from https://arc.aiaa.org/doi/abs/10.2514/6.2023-3640 doi: 10.2514/6.2023-3640

Esteban, L. B., Rodríguez-López, E., Ferreira, M. A., & Ganapathisubramani, B. (2022, Sep). Mean flow of turbulent boundary layers over porous substrates. *Phys. Rev. Fluids*, *7*, 094603. Retrieved from https://link.aps.org/doi/10.1103/PhysRevFluids.7.094603 doi: 10.1103/PhysRevFluids.7.094603

Fahy, F. (2001). 4 - impedance. In F. Fahy (Ed.), *Foundations of engineering acoustics* (p. 48-73). London: Academic Press. Retrieved from https://www.sciencedirect.com/science/article/pii/B9780122476655500059 doi: https://doi.org/10.1016/B978-012247665-5/50005-9

Favre, A. J. (1969). Statistical equations of turbulent gases. In *Problems of hydrodynamics and continuum mechanics* (p. 231-266). Philadelphia, PA: Society for Industrial and Applied Mathematics.

Flack, & Schultz, M. (2010, 04). Review of hydraulic roughness scales in the fully rough regime. *Journal of Fluids Engineering-transactions of The Asme - J FLUID ENG*, *132*. doi: 10.1115/1.4001492

Flack, & Schultz, M. P. (2014, 09). Roughness effects on wall-bounded turbulent flowsa). *Physics of Fluids*, *26*(10), 101305. Retrieved from https://doi.org/10.1063/1.4896280 doi: 10.1063/1.4896280

Flack, Schultz, M. P., & Connelly, J. S. (2007, 09). Examination of a critical roughness height for outer layer similarity. *Physics of Fluids*, *19*(9). Retrieved from https://doi.org/10.1063/1.2757708 (095104) doi: 10.1063/1.2757708

Flack, Schultz, M. P., & Shapiro, A. T. (2005). Experimental support for townsend's reynolds number similarity hypothesis on rough walls. *Physics of Fluids*, *17*.

Gan, G., & Riffat, S. B. (1997). Pressure loss characteristics of orifice and perforated plates. *Experimental Thermal and Fluid Science*, *14*(2), 160-165. Retrieved from https://www.sciencedirect.com/science/article/pii/S0894177796000416 doi: https://doi.org/10.1016/S0894-1777(96)00041-6

Garcia-Mayoral, R., & Jimenez, J. (2011). Hydrodynamic stability and breakdown of the viscous regime over riblets. *Journal of Fluid Mechanics*, *678*, 317–347. doi: 10.1017/jfm.2011.114

García Mayoral, R., Gomez de Segura, G., & Fairhall, C. (2018). The control of near-wall turbulence through surface texturing. *Fluid Dynamics Research*, *51*, -.

Gowree, E. R., Jagadeesh, C., & Atkin, C. (2019). Skin friction drag reduction over staggered three dimensional cavities. *Aerospace Science and Technology*. doi: 10.1016/j.ast.2018.11.001

Gustavsson et al., J. (2019). and zhang, yang and cattafesta, louis n. and kreitzman, jordan r. acoustic liner drag measurements. *25th AIAA/CEAS Aeroacoustics Conference*. doi: 10.2514/6.2019-2683

Hama, F. (1954). *Boundary-layer characteristics for smooth and rough surfaces, by francis r. hama.* Society of Naval Architects and Marine Engineers. Retrieved from https://books.google.nl/books?id=q-8zcgAACAAJ

Herbert, G. W., & Copiello, D. (2015). *Honeycomb structure.* Wikimedia Commons. Retrieved from https://commons.wikimedia.org/w/index.php?curid=38545220 (CC BY-SA 2.5 License)

Hetsroni, G., Mosyak, A., Pogrebnyak, E., & Yarin, L. (2011, 12). Micro-channels: Reality and myth. *Journal of Fluids Engineering*, *133*, 121202. doi: 10.1115/1.4005317

Hillereau, N., Syed, A. A., & Gutmark, E. J. (2005). Measurements of the acoustic attenuation by single layer acoustic liners constructed with simulated porous honeycomb cores. *J Sound Vib*, *286*, 21-36.

Howerton, B. M., & Jones, M. G. (2015). Acoustic liner drag: A parametric study of conventional configurations. In *21st aiaa/ceas aeroacoustics conference.* Retrieved from https://arc.aiaa.org/doi/abs/10.2514/6.2015-2230 doi: 10.2514/6.2015-2230

Howerton, B. M., & Jones, M. G. (2016). Acoustic liner drag: Measurements on novel facesheet perforate geometries. In *22nd aiaa/ceas aeroacoustics conference.* Retrieved from https://arc.aiaa.org/doi/abs/10.2514/6.2016-2979 doi: 10.2514/6.2016-2979

Howerton, B. M., & Jones, M. G. (2017). A conventional liner acoustic/drag interaction benchmark database. *23rd AIAA/CEAS Aeroacoustics Conference*. Retrieved from https://arc.aiaa.org/doi/abs/10.2514/6.2017-4190 doi: 10.2514/6.2017-4190

Howerton, B. M., Jones, M. G., & Buckley, J. L. (2012). Development and validation of an interactive liner design and impedance modeling tool. In *Proceedings of the 18th aiaa/ceas aeroacoustics conference (33rd aiaa aeroacoustics conference).* Colorado Springs.

Ibrahim, J., de Segura, G. G., Chung, D., & García-Mayoral, R. (2021). The smooth-wall-like behaviour of turbulence over drag-altering surfaces: a unifying virtual-origin framework. *Journal of Fluid Mechanics*, *915*, A56. doi: 10.1017/jfm.2021.13

Ichihashi, F. (2013, Dec.). *Structure with active acoustic openings* (U.S. Patent No. 2013/0341119 A1).

Ingard, U. (1953, 06). On the Theory and Design of Acoustic Resonators. *The Journal of the Acoustical Society of America*, *25*(6), 1037-1061. doi: 10.1121/1.1907235

Jackson, P. S. (1981). On the displacement height in the logarithmic velocity profile. *Journal of Fluid Mechanics*, *111*, 15–25. doi: 10.1017/S0022112081002279

Jasinski, C., & Corke, T. (2020, 05). Mechanism for increased viscous drag over porous sheet acoustic liners. *AIAA Journal*, *58*, 1-12. doi: 10.2514/1.J059039

Jiménez, J. (2004, 01). Turbulent flows over rough wall. *Annu. Rev. Fluid Mech*, *36*, 173-96.

Jones, M., Simon, F., & Roncen, R. (2022). Broadband and low-frequency acoustic liner investigations at nasa and onera. *AIAA Journal*, *60*(4), 2481-2500. doi: 10.2514/1.J060862

Jones, M., Watson, W. R., Nark, B. M., Douglas M. Howerton, & Brown, M. C. (2020). A review of acoustic liner experimental characterization at nasa langley. *Langley Research Center, Hampton, Virginia*.

Kempton, A. (2011). *Acoustic liners for modern aero-engines.* Rolls-Royce.

Kornilov, V., & Boiko, A. V. (2012). Efficiency of air microblowing through microperforated wall for flat plate drag reduction. *Aiaa Journal*. doi: 10.2514/1.j051426

Kostek, T. M., & Franchek, M. A. (2000). Hybrid noise control in ducts. *J Sound Vib*, *237*, 81-100.

Krogstad, P., & Efros, V. (2012). About turbulence statistics in the outer part of a boundary layer developing over two-dimensional surface roughness. *Physics of Fluids*, *24*.

Kuwata, Y., & Suga, K. (2016). Lattice boltzmann direct numerical simulation of interface turbulence over porous and rough walls. *Int. J. Heat Fluid Flow*, *61*, 145–157.

Kuwata, Y., & Suga, K. (2019). Extensive investigation of the influence of wall permeability on turbulence. *International Journal of Heat and Fluid Flow*, *80*, 108465. Retrieved from https://www.sciencedirect.com/science/article/pii/S0142727X1930373X doi: https://doi.org/10.1016/j.ijheatfluidflow.2019.108465

La Rosa, D. M., Rossi, M. M. A., Ferrarese, G., & Malavasi, S. (2021, 02). On the Pressure Losses Through Multistage Perforated Plates. *Journal of Fluids Engineering*, *143*(6), 061205. Retrieved from https://doi.org/10.1115/1.4049937 doi: 10.1115/1.4049937

Lee, & Ih, J.-G. (2003). Empirical model of the acoustic impedance of a circular orifice in grazing mean flow. *The Journal of the Acoustical Society of America*, *114*(1), 98–113. Retrieved from https://doi.org/10.1121/1.1581280 doi: 10.1121/1.1581280

Lee, & Moser, R. (2015). Direct numerical simulation of turbulent channel flow up to $Re_\tau \approx 5200$. *Journal of Fluid Mechanics*, *774*, 395–415. doi: 10.1017/jfm.2015.268

Lee, & Yeo, J. H. (1997). Modeling of darcy-forchheimer drag for fluid flow across a bank of circular cylinders. *International Journal of Heat and Mass Transfer*, *40*(13), 3149–3155.

Liu, Horowitz, S., Nishida, T., Cattafesta, L., & Sheplak, M. (2003). A tunable electromechanical helmholtz resonator. In *Aiaa paper 2003-3145*.

Liu, & Hu, C. (2019). An actuator line - immersed boundary method for simulation of multiple tidal turbines. *Renewable Energy*, *136*, 473-490. Retrieved from https://www.sciencedirect.com/science/article/pii/S0960148119300199 doi: https://doi.org/10.1016/j.renene.2019.01.019

Luchini, P., Manzo, F., & Pozzi, A. (1991). Resistance of a grooved surface to parallel flow and cross-flow. *Journal of Fluid Mechanics*, *228*, 87–109. doi: 10.1017/S0022112091002641

MacDonald, M., Chan, L., Chung, D., Hutchins, N., & Ooi, A. (2016, sep). Turbulent flow over transitionally rough surfaces with varying roughness densities. *Journal of Fluid Mechanics*, *804*, 130–161. Retrieved from https://doi.org/10.10172Fjfm.2016.459 doi: 10.1017/jfm.2016.459

MacDonald, M., Ooi, A., García-Mayoral, R., Hutchins, N., & Chung, D. (2018). Direct numerical simulation of high aspect ratio spanwise-aligned bars. *J. Fluid Mech.*, *843*, 126–55.

Manes, C., Pokrajac, D., McEwan, I., & Nikora, V. (2009, 12). Turbulence structure of open channel flows over permeable and impermeable beds: A comparative study. *Physics of Fluids*, *21*(12), 125109. Retrieved from https://doi.org/10.1063/1.3276292 doi: 10.1063/1.3276292

Matsuhisa, H., Ren, B., & Sato, S. (1992). Semiactive control of duct noise by a volume-variable resonator. *JSME Int J III-Vib C*, *35*, 223-228.

McAuliffe, C. E. (1950). *The influence of high-speed flow on the behavior of acoustical elements* (Unpublished master's thesis). Massachusetts Institute of Technology.

McDonald, A. M., Hutchins, S. M., Stothers, I., et al. (1997). *Method and apparatus for attenuating acoustic vibrations in a medium* (European Patent No. EP0572492B1).

Mechel, F. P. (2008). Formulas of acoustics. In (pp. 830–831). Springer Berlin Heidelberg. Retrieved from https://doi.org/10.1007/978-3-540-76833-3_240 doi: 10.1007/978-3-540-76833-3_240

Mittal, R., & Iaccarino, G. (2005). Immersed boundary methods. *Annual Review of Fluid Mechanics*, *37*(1), 239-261. Retrieved from https://doi.org/10.1146/annurev.fluid.37.061903.175743 doi: 10.1146/annurev.fluid.37.061903.175743

Modesti, D., Endrikat, S., Hutchins, N., & Chung, D. (2021). Dispersive stresses in turbulent flow over riblets. *Journal of Fluid Mechanics*, *917*, A55. doi: 10.1017/jfm.2021.310

Nagaya, K., Hano, Y., & Suda, A. (2001). Silencer consisting of two-stage helmholtz resonator with auto-tuning control. *J Acoust Soc Am*, *110*, 289-295.

Nikuradse, J. (1933). Strömungsgesetze in rauhen rohren. *VDI-Forschungsh. 361. Berlin: Ver. Dtsch. Ing.*.

Orlandi, P., & Leonardi, S. (2006). Dns of turbulent channel flows with two- and three-dimensional roughness. *Journal of Turbulence*, *7*, N73. Retrieved from https://doi.org/10.1080/14685240600827526 doi: 10.1080/14685240600827526

Orlandi, P., Leonardi, S., & Antonia, R. A. (2006). Turbulent channel flow with either transverse or longitudinal roughness elements on one wall. *Journal of Fluid Mechanics*, *561*, 279–305. Retrieved from https://doi.org/10.1017/S0022112006000723 doi: 10.1017/S0022112006000723

O'Connor, J., Diessner, M., Wilson, K., Whalley, R. D., Wynn, A., & Laizet, S. (2023). Optimisation and analysis of streamwise-varying wall-normal blowing in a turbulent boundary layer. *Flow Turbulence and Combustion*. doi: 10.1007/s10494-023-00408-3

Palani, S., Murray, P., McAlpine, A., Sasaki, D., & Richter, C. (2021). Slanted septum and multiple folded cavity liners for broadband sound absorption. *International Journal of Aeroacoustics*. doi: 10.1177/1475472x211023835

Parrott, T. L., & Jones, M. G. (1995). Parallel-element liner impedances for improved absorption of broadband sound in ducts. *Noise Control Eng J*, *43*, 183-195.

Pirozzoli, S. (2010). Generalized conservative approximations of split convective derivative operators. *Journal of Computational Physics*, *229*(19), 7180-7190. Retrieved from https://www.sciencedirect.com/science/article/pii/S0021999110003219 doi: https://doi.org/10.1016/j.jcp.2010.06.006

Pirozzoli, S., Romero, J., Fatica, M., & Orlandi, P. (2022, 06). Dns of passive scalars in turbulent pipe flow. *Journal of Fluid Mechanics*, *940*. doi: 10.1017/jfm.2022.265

Pope, S. B. (2000). *Turbulent flows*. Cambridge University Press. doi: 10.1017/CBO9780511840531

Prandtl, L. (1925). Uber die ausgebildete turbulenz. *ZAMM - Journal of Applied Mathematics and Mechanics*.

Raupach, M. R., Antonia, R. A., & Rajagopalan, S. (1991, Jan 01). Rough-wall turbulent boundary layers. *Applied Mechanics Reviews*, *44*(1), 1-25. Retrieved from https://doi.org/10.1115/1.3119492 doi: 10.1115/1.3119492

Raupach, M. R., Thom, A. S., & Edwards, I. (1980, Jun 01). A wind-tunnel study of turbulent flow close to regularly arrayed rough surfaces. *Boundary-Layer Meteorology*, *18*(4), 373-397. Retrieved from https://doi.org/10.1007/BF00119495 doi: 10.1007/BF00119495

Reggente, M. (2014). *Statistical gas distribution modelling for mobile robot applications* (Doctoral dissertation). doi: 10.13140/2.1.1260.5760

Rosti, M. E., Brandt, L., & Pinelli, A. (2018). Turbulent channel flow over an anisotropic porous wall - drag increase and reduction. *Journal of Fluid Mechanics*, *842*, 381–394. Retrieved from https://doi.org/10.1017/jfm.2018.152 doi: 10.1017/jfm.2018.152

Rothstein, J. P. (2010). Slip on superhydrophobic surfaces. *Annual Review of Fluid Mechanics*, *42*(1), 89-109. Retrieved from https://doi.org/10.1146/annurev-fluid-121108-145558 doi: 10.1146/annurev-fluid-121108-145558

Scarano, F., Jacob, M. C., Gojon, R., Carbonneau, X., & Gowree, E. R. (2022). Modification of a turbulent boundary layer by circular cavities. *Physics of Fluids*. doi: 10.1063/5.0091110

Scarano, F., Jacob, M. C., & Gowree, E. R. (2023). Drag reduction by means of an array of staggered circular cavities at moderate reynolds numbers. *International Journal of Heat and Fluid Flow*, *102*, 109142. Retrieved from https://www.sciencedirect.com/science/article/pii/S0142727X23000413 doi: https://doi.org/10.1016/j.ijheatfluidflow.2023.109142

Schiller, N., Jones, M., Howerton, B., & Nark, D. (2019). *Initial developments of a low-drag, variable-depth acoustic liner*. doi: 10.2514/6.2019-2749

Schlichting. (1937). Experimental investigation of the problem of surface roughness.

Schlichting. (1968). *Boundary-layer theory* (6th ed.). New York: McGraw-Hill.

Shahzad, H., Hickel, S., & Modesti, D. (2022, Nov 01). Permeability and turbulence over perforated plates. *Flow, Turbulence and Combustion*, *109*(4), 1241-1254. Retrieved from https://doi.org/10.1007/s10494-022-00337-7 doi: 10.1007/s10494-022-00337-7

Shahzad, H., Hickel, S., & Modesti, D. (2023). Turbulence and added drag over acoustic liners. *Journal of Fluid Mechanics*, *965*, A10. doi: 10.1017/jfm.2023.397

Sharma, A., & García-Mayoral, R. (2020, 04). Turbulent flows over dense filament canopies. *Journal of Fluid Mechanics*, *888*. doi: 10.1017/jfm.2020.27

Shur, M., Strelets, M., Travin, A., Suzuki, T., & Spalart, P. R. (2020). Unsteady simulation of sound propagation in turbulent flow inside a lined duct using a broadband time-domain impedance model. In *Aiaa paper 2020-2535*.

Spalart, P. R., Moser, R. D., & Rogers, M. M. (1991). Spectral methods for the navier-stokes equations with one infinite and two periodic directions. *Journal of Computational Physics*, *96*(2), 297-324. Retrieved from https://www.sciencedirect.com/science/article/pii/002199919190238G doi: https://doi.org/10.1016/0021-9991(91)90238-G

Sutliff, D. L., & Jones, M. G. (2009). Low-speed fan noise attenuation from a foam-metal liner. *J Aircraft*, *46*, 1381-1394.

Sutliff, D. L., Jones, M. G., & Hartley, T. C. (2013). High-speed turbofan noise reduction using foam-metal liner over-the-rotor. *J Aircraft*, *50*, 1491-1503.

Svetgoff, A., & Manimala, J. (2018). Absorption characteristics of membrane-embedded acoustic liners. In *Proceedings of the inter-noise and noise-con congress and conference*. Chicago.

Tanner, P., Gorman, J., & Sparrow, R. (2019). Flow-pressure drop characteristics of perforated plates. *International Journal of Numerical Methods for Heat Fluid Flow*, *29*(11), 4310–4333. Retrieved from https://doi.org/10.1108/HFF-01-2019-0065 doi: 10.1108/HFF-01-2019-0065

Thakkar, M., Busse, A., & Sandham, N. D. (2018). Direct numerical simulation of turbulent channel flow over a surrogate for nikuradse-type roughness. *Journal of Fluid Mechanics*, *837*, R1. doi: 10.1017/jfm.2017.873

Thomas, R. H., Burley, C. L., Lopes, L. V., Bahr, C. J., Gern, F. H., & Zante, D. E. V. (2014). System noise assessment and the potential for low noise hybrid wing body aircraft with open rotor propulsion. In *52nd aerospace sciences meeting*. Retrieved from https://arc.aiaa.org/doi/abs/10.2514/6.2014-0258 doi: 10.2514/6.2014-0258

Townsend, A. A. (1956). The structure of turbulent shear flow. *Cambridge University Press*, *1*(5), 554-560. doi: 10.1017/S0022112056210366

van Hout, R., Rinsky, V., & Grobman, Y. (2018). Experimental study of a round jet impinging on a flat surface: Flow field and vortex characteristics in the wall jet. *International Journal of Heat*

and Fluid Flow, *70*, 41-58. Retrieved from https://www.sciencedirect.com/science/article/pii/S0142727X17305453 doi: https://doi.org/10.1016/j.ijheatfluidflow.2018.01.010

von Karman, T. (1930). Mechenical similtude and turbulence. *Nachrichten von der Gesellschaft der Wissenschaften*.

Watson, W., Robinson, J., Jones, M., & Parrott, T. (2004, May). Computational study of optimum and off-design performance of checkerboard liners. In *Aiaa paper 2004-3030.* doi: 10.2514/6.2004-3030

Weller, H., Tabor, G., Jasak, H., & Fureby, C. (1998). A tensorial approach to computational continuum mechanics using object-oriented techniques. *Comput. Phys.*, *12*(6), 620–631. doi: 10.1063/1.168744

Whitaker, S. (1969). Advances in theory of fluid motion in porous media. *Industrial & Engineering Chemistry*. doi: 10.1021/ie50720a004

Wilkinson, S. (1983). Influence of wall permeability on turbulent boundary-layer properties. In *21st aerospace sciences meeting.* doi: 10.2514/6.1983-294

Williams, K., Chiu, G., & Bernhard, R. (2002). Adaptive-passive absorbers using shape-memory alloys. *Journal of Sound and Vibration*, *249*(5), 835–848. doi: 10.1006/jsvi.2000.3496

XuQiang, M., & ZhengTao, S. (2020). Development of acoustic liner in aero engine: A review. *Sci. China Technol. Sci.*, *63*, 2491-2504. Retrieved from https://doi.org/10.1007/s11431-019-1501-3 doi: 10.1007/s11431-019-1501-3

Yang, Z., Dai, H., Chan, N., Ma, G., & Sheng, P. (2010). Acoustic metamaterial panels for sound attenuation in the 50–1000 hz regime. *Applied Physics Letters*, *96*(4). Retrieved from https://doi.org/10.1063/1.3299007 doi: 10.1063/1.3299007

Zhang, Q., & Bodony, D. J. (2016). Numerical investigation of a honeycomb liner grazed by laminar and turbulent boundary layers. *Journal of Fluid Mechanics*. doi: 10.1017/jfm.2016.79

Zhao, C., Wood, G. S., Xie, J., Chang, H., Pu, S. H., & Kraft, M. (2016). A three degree-of-freedom weakly coupled resonator sensor with enhanced stiffness sensitivity. *Journal of Microelectromechanical Systems*, *25*(1), 38-51. Retrieved from https://doi.org/10.1109/jmems.2015.2490204 doi: 10.1109/jmems.2015.2490204

Zheng, M., Chen, C., & Li, X. (2022a). Direct measurements of aerodynamic drag of acoustic liners. In *28th aiaa/ceas aeroacoustics 2022 conference.* doi: 10.2514/6.2022-2927

Zheng, M., Chen, C., & Li, X. (2022b). Experimental investigation of factors influencing acoustic liner drag using direct measurement. *Aerospace Science and Technology*, *130*, 107903. doi: https://doi.org/10.1016/j.ast.2022.107903